NUMERICAL MODELLING OF POTENTIAL AND CURRENT DISTRIBUTIONS IN A BIPOLAR ELECTROLYTIC CELL

THÈSE N° 1772 (1998)

PRÉSENTÉE AU DÉPARTEMENT DE MATHÉMATIQUES

ÉCOLE POLYTECHNIQUE FÉDÉRALE DE LAUSANNE

POUR L'OBTENTION DU GRADE DE DOCTEUR ÈS SCIENCES TECHNIQUES

PAR

Eric MITHA

Ingénieur électricien diplômé EPF
de nationalité française

acceptée sur proposition du jury:

Prof. H. Froidevaux, directeur de thèse
Prof. Ch. Comninellis, corapporteur
Dr J.-Y. Salamin, corapporteur
Prof. A. Savall, corapporteur
Dr Ch. Trophime, corapporteur

Lausanne, EPFL
1998

" A little point revealed the infinitudes "
Sri Aurobindo's Savitri.

Acknowledgments

First, I would like to thank sincerely Professor H. Froidevaux, my thesis director, for providing me very good conditions for research, for his permanent interest in different aspects of my work, and for his judicious and experienced advice during these four years.

Secondly, I would like to thank Professor C. Comninellis, of the Institute of Chemical Engineering, for teaching me the basics of electrochemistry theory, for giving precious advice and with whom we had a fruitful collaboration.

Third, I would like to thank Dr.J.-Y. Salamin for introducing me into the project, for his very helpful hints and for accepting to be a member of the jury.

Fourth, I would like to thank Professor A. Savall to have accepted to take part in the evaluation of this work.

Fifth, I would like to thank Dr.C. Trophime for his experienced recommendations especially about three-dimensional problems of mesh generation and to have accepted to take part in the evaluation of this work.

Last, but not least, I would like to thank my wife and my family for their unfailing support during the whole period of this work.

Version abrégée

Ce travail concerne la modélisation de réacteurs électrochimiques à électrodes bipolaires. Nous proposons un modèle numérique permettant de calculer les distributions de potentiel et de courant électrique dans une cellule électrochimique de géométrie quelconque de deux ou trois dimensions contenant des électrodes à potentiel flottant a priori inconnu. Nous présentons tout d'abord les principes généraux de fonctionnement d'un réacteur électrochimique et plus particulièrement les phénomènes cinétiques et thermodynamiques responsables des discontinuités de potentiel aux interfaces métal-solution.

Nous présentons ensuite un modèle mathématique complet. Il contient les équations de conservation du courant électrique et les conditions non-linéaires aux interfaces. Ce problème est approché et résolu par une méthode d'éléments finis pour des systèmes bi et tridimensionnels. Un exposé détaillé des approximations qui ont été faites ainsi que les algorithmes de résolution numérique sont décrits.

Un logiciel de calcul a été implémenté et des résultats de simulation numérique ont été comparés à des mesures expérimentales. Finalement, un certain nombre de résultats de simulation sont présentés. Plusieurs réacteurs de géométrie différente ont été modélisés pour des applications notamment à l'électrolyse de l'eau et à la décontamination de sols pollués.

Abstract

This work deals with the modelling of electrochemical reactors with bipolar electrodes. We give a numerical model which enables us to compute electrical current and potential distributions in an electrochemical cell of any type of geometry in two and three dimensions, including electrodes at an unknown floating potential.

We first present electrochemical reactors and particularly insist on kinetics and thermodynamics phenomena responsible on potential discontinuities at electrodes-electrolyte interfaces.

Secondly, we derive a complete mathematical model which contains the equations of conservation of the electrical current and the nonlinear conditions at interfaces. This problem is approached and solved using a finite element method for two and three-dimensional systems. A detailed description of approximations we have made and algorithms of numerical solving are then given.

Afterwards, the architecture of the software that we have built is detailed and numerical simulations are compared to experimental measurements. Finally, some computation results are presented. Several geometries of different reactors have been simulated with applications in water electrolysis and soils decontamination.

Contents

List of Figures

List of Symbols

The given unit is the one the most employed in this paper and the last column gives the section in which the symbol appears for the first time.

α	transfer coefficient		1.2
δ_u	electrical potential	[V]	4.3
ϵ_{kellog}	relative error		4.3
ϵ_{min}	relative error		4.3
ϵ_z	volumetric gas fraction		5.2
η	overpotential	[V]	1.2
λ	*Kellog* parameter (> 0)		3.3
$\mu(q)$	length or area exchange relative to the node q		3.2
$\underline{\nu}$	unit normal vector to the boundary		2.1
ρ_n	norm of the descent vector at iteration n		3.4
σ^m	conductivity of the metal	$[\Omega^{-1}\mathrm{mm}^{-1}]$	2.1
σ^e	conductivity of the electrolyte	$[\Omega^{-1}\mathrm{mm}^{-1}]$	2.1
φ	extended *Butler-Volmer* function		1.2
ψ	primitive of φ		2.1
$\underline{\omega}_n$	vector of descent at iteration n		3.4

$\Gamma^1(V)$	boundary of anode at potential V		2.1
$\Gamma^2(0)$	boundary of cathode at potential 0		2.1
$\Gamma^i(V_i)$	boundary of electrode i at potential V_i		2.2
Γ^m	boundary of Ω^m in contact with the electrolyte		2.1
Γ^m_j	boundary of Ω^m_j in contact with the electrolyte		2.2
Γ_N	boundary electrolyte-insulator		2.1
Φ^e	potential of the electrolyte	[V]	1.2
$\underline{\Phi}^e$	vector of nodes values of the approximation of Φ^e		3.2
$\underline{\Phi}^e(q)$	component q of $\underline{\Phi}^e$		3.2
$\underline{\Phi}^e_n$	$\underline{\Phi}^e$ at iteration n		3.3
Φ^m	potential of the electrode	[V]	1.2
Φ^m_j	potential of the electrode j	[V]	2.1
$\Phi^m_{j_n}$	potential of the electrode j at iteration n	[V]	3.2
$\underline{\Phi}^m_n$	vector of potentials $\Phi^m_{j_n}$ at iteration n		3.3
Ψ	current bypass		1.3
Ω^e	bounded domain of the electrolyte		2.1
Ω^e_h	discretization of Ω^e		3.1
Ω^m	domain of the bipolar electrode		2.1
Ω^m_j	domain of the the bipolar electrode		2.1
$\mathbf{a}_{el}$	elementary stiffness matrix		3.2
$\mathbf{a}_{el_{i,j}}$	(i,j) term of $\mathbf{a}_{el}$		3.2
$\mathbf{A}$	over-all stiffness matrix		3.2
$\mathbf{A}_{i,j}$	(i,j) term of $\mathbf{A}$		3.2
$\mathbf{A}_2$	modified over-all stiffness matrix		4.3
$\mathbf{bv}$	secondary potential vector		4.3
$\underline{\mathbf{B}}_\Gamma(\underline{\Phi}^e)$	"*Butler-Volmer*" vector for the interface Γ		3.2
$\underline{\mathbf{B}}(\underline{\Phi}^e)$	over-all "*Butler-Volmer*" vector		3.2
Bn	dimensionless bipolar number		1.3

c_0	concentration of the species O		1.2
c_R	concentration of the species R		1.2
C_k	constant		3.4
DIM	space dimension		4.3
$\underline{E}$	electrical field	$[\mathrm{Vm}^{-1}]$	2.1
E_e	equilibrium potential	[V]	1.2
E_e^o	tabulated standard potential	[V]	1.2
E_{el}	tetrahedral element		3.2
$\mathbf{f}$	intermediate vector		4.3
F	Faraday number = 96500 [A.s]		1.2
$\mathcal{F}$	3×3 matrix		3.2
$\underline{g}$	intermediate vector		3.3
Gb	dimensionless geometric bypass		1.2
h	diameter of the circumcircle of a triangle		3.1
H	set of functions		2.1
$\underline{i}$	current flow density vector		1.2
i	normal component of $\underline{i}$	$[\mathrm{Amm}^{-2}]$	1.2
i_a	anodic current density	$[\mathrm{Amm}^{-2}]$	1.2
i_c	cathodic current density	$[\mathrm{Amm}^{-2}]$	1.2
i_l	limiting value of the current density	$[\mathrm{Amm}^{-2}]$	1.2
I	total current crossing the cell	[A]	5.2
I_0	exchange current density	$[\mathrm{Amm}^{-2}]$	1.2
I_b	current entering the bipolar electrode	[A]	5.1
I_{lim}	limiting current of I	[A]	5.3
I_m	measured value of I	[A]	5.1
I_s	simulated value of I	[A]	5.1
I_{tot}	total current flow crossing Γ^m	[A]	4.3
J	functional		2.1
$\mathcal{J}$	numerical approximation of J		3.4
$\mathcal{M}$	3×3 matrix		3.2
n	number of nodes per line		3.5
n_e	number of tetrahedral elements		3.1
n_{it}	number of iterations		4.5
n_t	number of triangles		3.1

N	number of nodes per layer		3.5
N_b	number of bipolar electrodes		2.2
N_f	number of electrodes at a fixed potential		2.2
N_n	number of nodes of the discretization		3.1
N_s	number of sides		4.3
N_t	number of elements		4.3
$Nelem$	number of elements of the 2D mesh		3.5
NTE	number of elements		
	(number of slices $\times Nelem$)		3.5
NTN	number of nodes (number of layers$\times N$)		3.5
T	temperature	[°C]	5.1
$\mathcal{T}^e$	set of all elements mapping Ω^e		3.2
$\mathcal{T}^i(V_i)$	set of all faces mapping $\Gamma^i(V_i)$		3.2
T_{el_k}	triangle k		3.1
$\tilde{u}$	function of (x, y, z)		3.5
u	function of (x, y)		3.5
u'	function of (x, y)		3.5
u^e	electrical potential of the electrolyte	[V]	2.1
$\underline{u}^e$	vector of nodes values		
	of the approximation of u^e		3.2
$\underline{u}^e(q)$	component q of $\underline{u}^e$		3.2
U_{cell}	cell potential	[V]	5.1
U_{bip}	bipolar electrode potential	[V]	4.3
$\underline{v}_k$	unit vector of $\underline{\omega}_k$		3.4
V	applied difference of potential	[V]	1.1
V_b	potential of the bipolar electrode	[V]	2.1
V_{b_j}	potential of the bipolar electrode j	[V]	2.2
V_i	potential of the electrode i	[V]	2.1
$\mathbf{V}$	vector of fixed potentials V_i		4.3
$\dot{V}_{gz}$	volume flow rate of the gas	[mm^{3}s^{-1}]	5.2
$\dot{V}_l$	volume flow rate of the electrolyte	[mm^{3}s^{-1}]	5.2
$\mathbf{x}$	primary potential vector		4.3
$\mathbf{y}$	intermediary vector		4.3
$\mathbf{z}$	secondary solution vector		4.3

Introduction

Bipolar electrochemical reactors have received a lot of attention recently. Two major attractions of the bipolar reactor are compactness and low investment cost but its main disadvantage is the presence of parasitic electrical current or by-pass current. This results in a Faradaic efficiency loss, an inhomogeneous potential and current distribution, which means an increase in corrosion rate of the electrodes.

The knowledge of these distributions is of a great interest because of their incidence on the lifetime of electrodes and on the energy consumption. This is an excellent example of a problem which has important industrial applications : water electrolyzer for hydrogen production [ALY], electrolytic regeneration [CC95a], batteries [CC95b], soil decontamination [LPS89], and which cannot be solved (completely) either analytically or experimentally.

Description of the problem

We consider here general electrochemical systems composed of electrodes, electrolyte and insulators. Each environment has its own electrical conductivity. The conductivity of the electrolyte can either be constant or variable, and the conductivity of the electrodes are much higher than the conductivity of the electrolyte and therefore the potential in the electrodes are supposed to be constant.

At interfaces electrodes-electrolytes, there is a nonlinear relationship between the potential drop (metal-solution) and the crossing current. Electrodes can be of any type of material and any type of

geometry. Electrochemical systems can be of any type of geometry in two and three dimensions. Some electrodes are current feeders at a fixed known potential, others are not fed and have a floating unknown potential. Some parts of a such electrode act as an anode, other parts as a cathode. They are the bipolar electrodes.

These electrochemical processes are described by partial differential equations. The complete model, needed for the mathematical description of phenomena which interest us, is composed of partial differential equations accompanied by complicated boundary conditions due to the nonlinear phenomena at interfaces.

As an analytical or an experimental approach did not solve completely such problems, numerical simulation remains the only way of attack.

Rapid progress in computer technology has made workstations more and more powerful, especially in the last decade. This means that increasingly fast calculations and large memory storage are now possible. This has made feasible numerical simulations of exceedingly complex phenomena, like the one we shall study in this work.

The goal of this work is to provide a two and three-dimensional general model for designing electrochemical cells with bipolar electrodes. This has been achieved by developing advanced numerical techniques, which can predict those floating potentials of bipolar electrodes and those inhomogeneous potential and current distributions in the whole reactor, especially the ones at metal-solution interfaces where the reaction takes place.

This thesis is at the junction of electrochemistry, numerical analysis, and computer science.

History of the project

Due to the importance of the problem it is not surprising to know that several different studies, from theoretical, numerical and experimental points of view, have been undertaken. We will mention the important bibliographical references in the following description.

Several authors have treated the subject of bipolar electrochemical reactors using an electrical analogy [IR86], [JB79], [EK83]. Some others solve analytically the Laplace equation [SS90], [JH84], [J.N73], [Mar91], [SY91].
But as it is impossible to find an analytical general solution, numerical approach becomes the only one possible. Some authors have developed numerical methods [AS84], [RW90], [YSC96], [Bol88], giving good results for primary current and potential distributions.
Others have calculated secondary current and potential distributions [Rou74], [JD97], [PM97] in monopolar configurations, but those methods are not applicable in bipolar situations. Some others chose an experimental approach by measuring either the thickness of a metallic deposition [Dec94], [Lan94] or by fragmenting electrodes and measuring separately the current in each fragment [LJ91], [Bon92].

For the moment, it suffices to say that our work, at the Swiss Federal Institute of Technology (EPFL), is the extension of the work of J.-Y. Salamin [Sal95].
His thesis, like the present one, was done in collaboration with the Institute of Chemical Engineering of EPFL, the Paul Scherrer Institut and partly financially supported by the Swiss Federal Office of Energy [FS94], [FM95a].
P. Bolomey [Bol88] and G. Bonvin [Bon92] had undertaken the initial works on modelling bipolar electrochemical reactors.

J.-Y. Salamin has treated the numerical modelling of two-dimensional electrochemical reactors made of parallel bipolar plates. In his work, symmetrical electrolyzers have been modelled.

Our work is a natural extension of his work. We deal with any type of geometry of electrodes and any type of geometry of reactors in two or three dimensions. Furthermore, we have also incorporated effects of conductivity variation (§ 5.2.5) due to the formation of bubbles in the reactor.

Description of the chapters

In chapter 1 we consider electrochemical reactors in general and describe its theoretical principles.

We particularly insist on the interface conditions and give major results and equations to build progressively the extended *Butler-Volmer* function taking into account the kinetics and the thermodynamics. Then bipolar reactors are introduced and compared with their monopolar analog.

In chapter 2 we derive a complete mathematical model which contains the physical phenomena of interest.

Current conservation, and the current-potential function defined in chapter 1 at interfaces comprise our modelling. It starts with a simple two-dimensional model with one bipolar electrode and continue with three mathematical formulations of the problem for general cases.

In chapter 3, we describe in detail all the different types of numerical approximations which were used to obtain the final discrete equations. To solve those systems of nonlinear partial differential equations we shall employ a finite element method (FEM). We use a finite element discretization in space. We believe that this approach is very flexible. The finite element method makes it possible to handle complicated two and three-dimensional geometries with ease. Algorithms of numerical solving and an original method of determination of the potentials of the bipolar electrodes, which we believe to be new and efficient, are detailed in this chapter.

Chapter 4 of this thesis deals with the code we have written. All programming aspects are described from the finite element mesh generator used to the graphical output of the computation results. To validate the software we have built, some tests are made and because we employ iterative methods, a study of the parameters inherent in such methods is undertaken. This study helps us for the choice of those parameters in order to accelerate the convergence to the solution.

The final chapter of this thesis deals with computation results

which we obtained by our code. In § 5.1 we compare our numerical results, concerning systems including one and two bipolar electrodes in any orientation between two parallel plates, with experimental measurements of V. Merminod [Mer96].

In § 5.2, the reactor which has been modelled in [Sal95] is investigated but the main differences are that, first the cell is modelled in three dimensions and secondly, that we introduce in this case a model concerning the conductivity of the electrolyte. We incorporate effects due to the formation of bubbles during the water electrolysis.

In § 5.3, we make an analysis of the behavior of a single sphere inserted in a three-dimensional electrolytic cell.

The fourth experiment is an application of the three-dimensional model to decontamination of sites and soils polluted with heavy metals, anions, or organic chemicals.

The last result deals with the modelling of a three-dimensional industrial electrolyzer for hydrogen production.

Chapter 1

Characterization of Electrochemical Cells

1.1 Generalities

Most electrochemical processes are effected in devices similar to that shown in Figure 1.1. Such a device is called an electrochemical cell. The anode transports the electrons out of the cell into an external circuit while the cathode acts as a sink for electrons from the internal circuit. The principal function of the anolyte and catholyte is to provide electrolytic charge transport within the cell. The separator, if present, serves as a barrier to mixing anodic and cathodic species.

The separator must be capable of transporting charge by ion migration between the anolyte and catholyte.

A difference of electrical potential V, the cell voltage is applied between the two electrodes which are called current feeders. We consider here water electrolysis in an alkaline environment but all our work is applicable to any kind of electrolysis.

The reaction takes place at the interfaces electrodes-electrolyte to produce new chemical species via an electronic exchange at the interfaces.

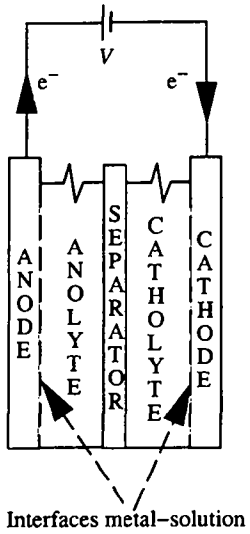

Figure 1.1: Schematic representation of an electrochemical cell

1.2 Interface conditions

We first summarize the key features of the thermodynamics and kinetics of electrode reactions [BF83], [BR85], for an interface of a working electrode in solution containing the species O, concentration c_O, and R, concentration c_R. Having a selected system so that the only electrode reaction occurring in the potential range of interest is:

$$O + ne^- \rightleftarrows R$$

Then, we will extend it to our case of water electrolysis in bipolar configurations.

1.2.1 Electrode reactions

The electric current is strictly controlled by the dynamic of the interfacial phenomena. Electron transfer can occur only over molecular dimensions, and, hence, the oxidation/reduction of the reactant will

be possible when it is immediately adjacent to the electrode. As a result, a significant chemical range at the electrode require at least a three step sequence:

$$A_{bulk} \xrightarrow{mass\ transport} A_{electrode}$$
$$A_{electrode} \xrightarrow{electron\ transfer} B_{electrode}$$
$$B_{electrode} \xrightarrow{mass\ transport} B_{bulk}$$

and the characteristics of an electrode reaction will be determined by both electron transfer and mass transport.
The rate of conversion reactant to product at an electrode will be determined by the slowest step in the previous sequence. Hence, it is possible to envisage four situations arising in different potential regions: it exists domains of potential for which no current can cross the cell and other domains where the current has a variable intensity. The general form of that current-potential characteristics is given in Figure 1.2.

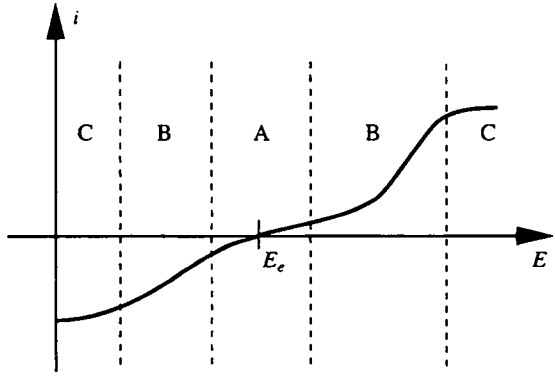

A : Tafel region (charge transfer control)
B : Mixed control
C : Mass transfer control

Figure 1.2: Typical i-E characteristics for an electrode reaction

For convenience, we introduce η the overpotential. It is defined by: $\eta = E - E_e$ and reflects the deviation of the system from equilibrium.

We describe then the four situations of different potential regions shown in Figure 1.2.

Equilibrium potential

At equilibrium, clearly no net chemical change can occur; the current through the cell must be zero: any current would convert O to R or R to O at the electrode surface. The working electrode will take up its equilibrium potential E_e. This value may be measured or calculated from the *Nernst Equation*

$$E_e = E_e^O + \frac{2.3RT}{nF}\log\frac{c_O}{c_R} \tag{1.1}$$

E_e^O is the standard potential for the couple, values are tabulated for many couples.

Tafel region

At low overpotentials, electron transfer is the sole rate determining step. Then, the current density vs. overpotential characteristic is defined by the *Butler-Volmer* equation:

$$i = I_0\left\{\exp\frac{\alpha nF\eta}{RT} - \exp\frac{-(1-\alpha)nF\eta}{RT}\right\} \tag{1.2}$$

The observed current density is the sum of the anodic and cathodic current densities and the magnitudes of each depends on:

(i) The exchange current density I_0.

(ii) The transfer coefficient α.

(iii) The applied overpotential η.

From the difference in signs of the arguments of the exponential terms of equation 1.2, only one of the exponential terms is significant. For example, at positive overpotentials and when $\eta > RT/\alpha nF$

$$i = I_0\exp\frac{\alpha nF\eta}{RT} \tag{1.3}$$

and hence

$$\log i = \log I_0 + \frac{\alpha n F \eta}{2.3RT} \tag{1.4}$$

At potential negative to the equilibrium value, the cathodic current density is related to overpotential by the Tafel equation:

$$\log(-i) = \log I_0 - \frac{(1-\alpha) n F \eta}{2.3RT} \tag{1.5}$$

and with 1.4 and 1.5, it becomes possible to determine the kinetic parameters I_0 and α, (see Figure 1.3). So, at low overpotentials, the

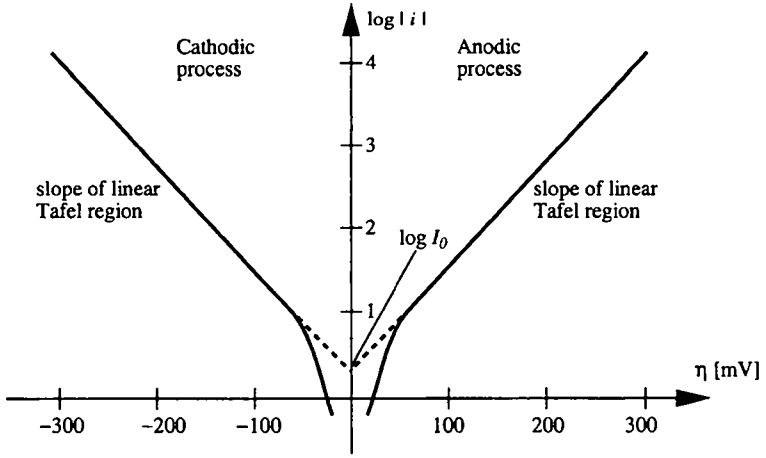

Figure 1.3: Tafel equations for anodic and cathodic branches of the i-E characteristic

i-E characteristic follows the equation (1.2) and the current density is the same under all mass transport conditions. In this potential range, the surface concentration of the reactant does not deviate significantly from the bulk value. ($\ll 1\%$).

Mixed control

As the rate of electron transfer increases exponentially with potential, (see Eq 1.4), the rate of electron transfer will become comparable to

the rate of mass transport.
In this region of mixed control, the surface concentration of reactant decreases from the bulk value and the current density varies to some extent with the mass transport conditions.

Mass transfer control

At high overpotentials, the rate of electron transfer becomes very fast and therefore mass transport becomes the rate determining step. Conversion of reactant to product at an electrode surface will always cause the concentration of reactant at the electrode to be lower than in the bulk will diffuse towards the electrode. Similarly, there will always be a driving force for diffusion of the product away from the surface. The current density becomes strongly dependent on the mass transport conditions but is independent of potential. The surface concentration of reactant drops to zero.

1.2.2 Water electrolysis

For the water electrolysis, we have to take into account the two couples: H_2O/H_2, hydrogen formation at the cathode and H_2O/O_2, oxygen formation at the anode.
We have the following reactions:

$4\ H_2O + 4\ e^-$	$\rightarrow$	$2\ H_2 + 4\ OH^-$	at the cathode
$4\ OH^-$	$\rightarrow$	$O_2 + 2\ H_2O + 4\ e^-$	at the anode
$2\ H_2O$	$\rightarrow$	$O_2 + 2\ H_2$	is the global reaction

Thermodynamics give the equilibrium potential of these couples.
Then for each half-reaction, the equations of Tafel (Eq. 1.3) are used for anodic and cathodic branches.
Finally, the mass transfer gives us the limiting current. Figure 1.4 shows a such function where the thermodynamics and kinetics contributions are present. It is a solution of KOH 4M.

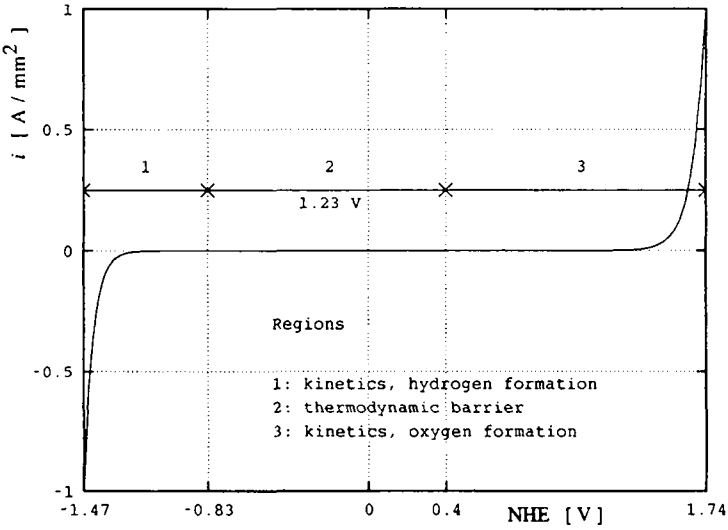

Figure 1.4: Current potential function built for water electrolysis in KOH 4M

Thermodynamic term

Equilibrium potentials of the two couples H_2O/H_2 and H_2O/O_2 are plotted on Figure 1.5 in function of the pH of the solution [Pou63]. Independently of the pH, the gap which gives the domain of stability of water is constant and equal to 1.23 V. That gap is the standard equilibrium potential for the system H_2O/H_2 and H_2O/O_2.
We have:

E=-0.06pH for H_2 and

E=-0.06pH + 1.23 for O_2.

This is the thermodynamic barrier to reach to have a current crossing the cell. The current density at the equilibrium potential is zero. That gap depends on the pressure, the temperature and on the concentration. Therefore the gap depends on the pH but not on the current crossing the interface and not on the metal constituting the electrodes.

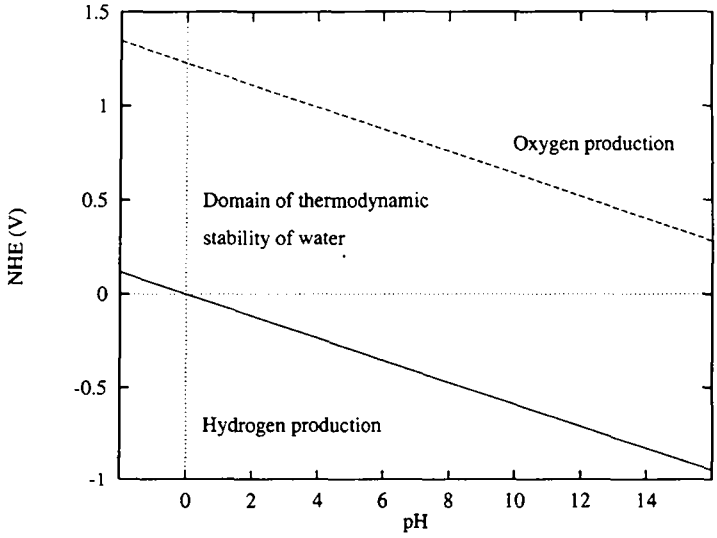

Figure 1.5: Domain of thermodynamic stability of water under pressure of 1 atm

If only the material of the electrodes changes, then the gap E_0 keeps the same value but the other terms of the current-potential function are modified.

Kinetics terms

The total current is the sum of the anodic and cathodic current i_c and i_a. When the overpotential is very negative, the anodic component of the current can be neglected, only the current equal to the absolute values of the cathodic side i_c counts. Similarly when the overpotential is very high, the cathodic component can be neglected and only the the current i_a counts. Near from the equilibrium potential, on each hand, the current increases (in absolute value) rapidly due to the exponential term. For water electrolysis in a solution of KOH 4M,

kinetics terms are obtained using Tafel's law :

$$\eta = a + b \log i \tag{1.6}$$

Then, for each half reaction, each exponential branch is build in finding the coefficients a and b for the cathode and the anode:

$$\begin{aligned} \eta = \quad & a_a + b_a \log i \quad \text{anodic branch} \\ \eta = \quad & a_c + b_c \log i \quad \text{cathodic branch} \end{aligned}$$

Tafel parameters are given in tables for nickel electrodes in KOH 4M, we have:
$a_a = 0.44\text{V} \;\; b_a = -0.163\text{V}$
$a_c = 0.02\text{V} \;\; b_c = -0.119\text{V}$

Mass transfer effects

When the electrolysis current reached high value i_l, the process takes place with the maximal speed corresponding to the mass transfer, because the species are reduced as fast as they arrive at the surface of the electrodes. Then, in this situation, the current is limited by the diffusion.
This value defined as i_l for both, anode and cathode is unknown.
We arbitrarily fix a limit of $i_l = 1\text{A/mm}^2$. This high value is realistic but generally not reached during the modeling of electrolysis conditions. This is more a numerical limitation that we introduce for the simulations.

1.2.3 The extended *Butler-Volmer* function

We have now described each part of the interfacial metal-solution function.
For all the following work, we call extended *Butler-Volmer* function a such function φ.

$\varphi : \mathbb{R} \rightarrow \mathbb{R}$ is a non-decreasing, continuous and a bounded function with $\varphi(0) = 0$.

Figure 1.6 shows a typical form of an extended *Butler-Volmer* function taking into account thermodynamics, kinetics and mass transfer effects. The sampled function shown in Figure 1.6 displays also the values that we store for future numerical simulations. (It will be stored in a file of couples (x, y)). Thermodynamics and kinetics are the values given in Figure 1.4. We have also incorporated the limiting current flow density of $i_l = 1[\mathrm{A/mm^2}]$.

We have here $i = \varphi(\Phi^m - \Phi^e)$ where
i is the current flow density in $[\mathrm{A/mm^2}]$ and
$\Phi^m - \Phi^e$ is the potential drop at metal-solution interface in [V].

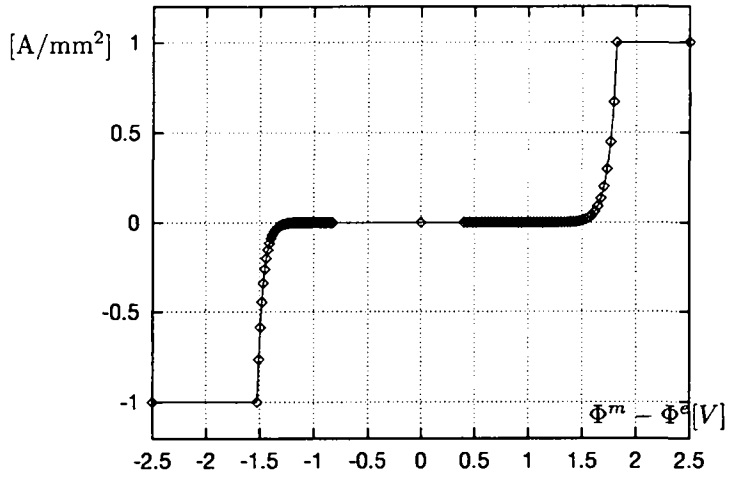

Figure 1.6: Extended *Butler-Volmer* with its sampled version

1.3 Bipolar cells and electrodes

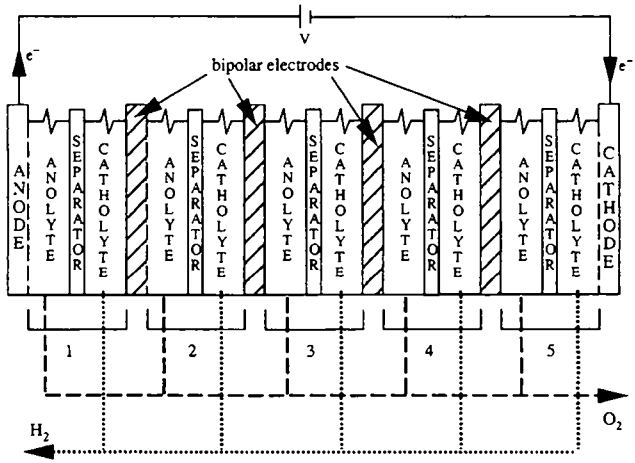

Figure 1.7: Bipolar electrolyzer

A bipolar configuration is a system where electrolytic cells may be connected in series in a common housing with the anode of one cell being electrically in series with the cathode of the prior cell and mounted on the opposite sides of a common structural member. The anodes of the cells are in series with the cathodes of the prior cell in the electrolyzer. A bipolar electrolyzer is shown in Figure 1.7, it has a plurality of individual electrolytic cells (1 to 5) electrically and mechanically in series, with an anodic end cell 1 at one end of the electrolyzer and cathodic end cell 5 at the opposite end of the cell. The internal electrodes take a different polarization on each side, giving the name 'bipolar'.

In the operation of the electrolyzer, an electrical current passes from the anodes of the first electrolytic cell through electrolyte to cathodes of the first electrolytic cell, evolving oxygen on the anodes, hydrogen on the cathodes. The electrical current then passes from the cathode to one cell to the anodes of the next adjacent cell in the

electrolyzer. No busbars are required inside the electrode stack and the reactor operates at a much higher voltage and much lower current than its monopolar analog.

Bipolar electrolyzers provide economy of materials of construction and plant space. Due to its high productivity and low cost, the bipolar electrochemical reactor is very interesting for industrial applications. However, the main disadvantage is the presence of parasitic electrical currents, or current bypass in the electrolyte inlet and outlet of the electrode stack. This results in a non-homogeneous potential and current distributions and consequently, poor selectivity and increase corrosion of the electrodes.

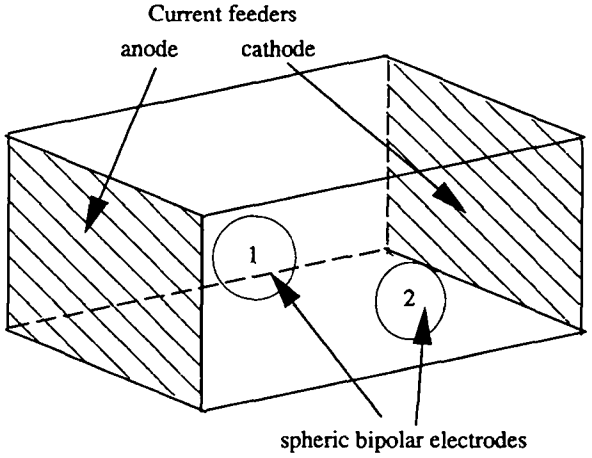

Figure 1.8: Schematic representation of a three-dimensional electrolyzer with two bipolar electrodes

The current bypass depends on the geometric configuration of the reactor, the current density, the conductivity of the electrolyte, the type of electrochemical reaction, the flow rate of the electrolyte and the number of elements in the reactor. [BC94] showed that for the scale-up of an electrochemical process, a relation between the current

bypass Ψ and two dimensionless numbers (Gb and Bn) exists:

$$\Psi = Gb(Bn + 1) \tag{1.7}$$

where the bipolar number Bn depends on the electrochemical system and on the process parameters in contrast of Gb, depending only on the geometry.

Modelling of such cells has been treated in the work of J.-Y. Salamin [Sal95] where bipolar electrolyzers were constituted of parallel plates. (Figure 1.7).

In this work, we present a generalized model of the work undertaken by J.-Y. Salamin [Sal95], G. Bonvin [Bon92] and P. Bolomey [Bol88]. We will deal with three-dimensional electrolyzers made of bipolar electrodes of any geometry (Figure 1.8), and will investigate the local behavior of such cells in terms of current and potential distributions. In Figure 1.8, there are two bipolar electrodes, but in many configurations, there is a stack of bipolar electrodes. In Figure 1.8, each bipolar electrode has a potential that is unknown and at the interface of each electrode including the bipolar electrodes (surface in contact with the electrolyte), the current-potential function is given by Figure 1.4.

Chapter 2

Mathematical Modelling

The goal of this chapter is to formulate clearly a mathematical model which will describe a bipolar electrolyzer.

For clarity reasons, we start by giving a simple model and the governing equations for a two-dimensional reactor : system made of an anode, a cathode and one bipolar electrode. It is a section of a three-dimensional electrolyzer.

We define first geometrically the domains and boundaries of this bipolar electrolyzer, then physical considerations are made to obtain a preliminary mathematical formulation. From that formulation, we give two others formulations corresponding to the exact problem to solve.

This is the first step of the modelling that will give us the equations for the electrical current and potential distributions in an electrolytic bipolar reactor.

Afterwards we describe laws for a general electrolytic cell (2D or 3D) of any geometry with several feeding electrodes and several bipolar electrodes.

The modelling presented here and the Apppendix A provided from the works [FS94], [FM95a], [FMS95], [Fro], [FM95b], [FMCM96], [FMC97] and [FC97].

2.1 Basic electrolyzer

2.1.1 Geometry

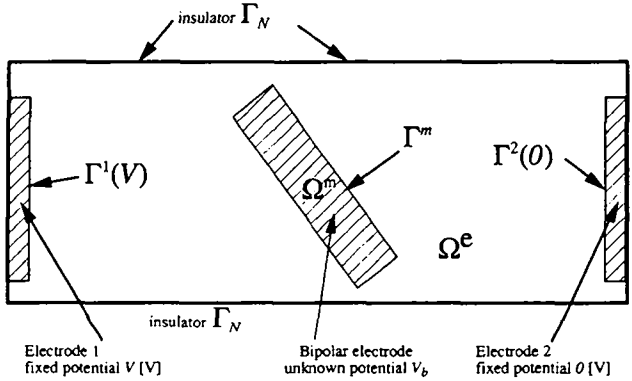

Figure 2.1: Geometry of a reactor with 2 current feeders and 1 bipolar electrode

Figure 2.1 gives a schematic representation of an electrolyzer with an anode, a cathode and one bipolar electrode in its center. It is a section of a three-dimensional reactor. The different domains and frontiers are designed as following:

1. Ω^e is the bounded domain of $\mathbb{R}^2$ occupied by the electrolyte.
2. Ω^m is the domain occupied by the bipolar electrode.
3. $\Gamma^1(V)$ is the part of the anode in contact with the electrolyte at the fixed potential V.
4. $\Gamma^2(0)$ is the part of the cathode in contact with the electrolyte at the fixed potential 0.
5. Γ^m is the boundary of Ω^m in contact with the electrolyte.
6. Γ_N is the part of the electrolyte in contact with an insulator.

2.1.2 Preliminary hypothesis

Having a geometrical characterization of the electrolyzer, we are interested now in finding the governing laws in relation with the electrical potential inside the reactor.
Before developing the governing equations of the system, the following important considerations have to be made.

1. **Stationarity**

   Under an applied cell potential difference V, the bipolar electrodes are polarized under an electrical field. At interfaces metal-electrolyte, the electron transfer takes place to produce the couple of reaction. In the electrolyte, the ionic transfer takes place under the effect of the electrical field.
   Supposing that the ionic diffusion at the electrodes is faster than the electrochemical reaction, then all phenomena are stationary. All time-derivatives variables are null ($\partial_t() = 0$).

2. **Isothermal conditions**

   Bulk temperature influences kinetics and thermodynamics parameters of the system. As the electrolyte has a minimal speed ($1\ \mathrm{ms}^{-1}$) and has a thermoregulation system, isothermal conditions are satisfied.

3. **Bipolar electrodes are equipotential**

   The numerical values of the electrical conductivities of our different environments have the following order of magnitude:

   $\sigma^e \approx 10^{-2}\,\Omega^{-1}\mathrm{mm}^{-1}$

   $\sigma^m \approx 10^{5}\,\Omega^{-1}\mathrm{mm}^{-1}$

   That means, if we compare the variation of electrical potential in both environments, for the same distance, using Ohm's law, we have:

   $\sigma^m(U - U^m) = \sigma^e(U - U^e)$

   with the electrical potentials U, U^m and U^e defined in Figure 2.2. So the variation of the potential in the electrolyte

$(U - U^e)$ is 10^7 higher than in the electrodes and each electrode can be considered as equipotential.

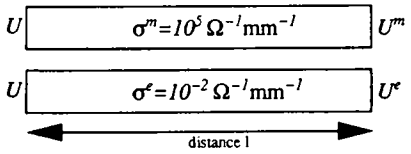

Figure 2.2: Potential variations depending on the environment

2.1.3 Parameters of the model

Finally, the parameters of the physic-chemical process are:

1. the interface conditions parameters:
   the extended *Butler-Volmer* function (§ 1.2.3) which depends on the electrodes material and on the electrolyte: with the hypothesis that all electrodes are made of the same material, the Extended *Butler-Volmer* characteristics is the same for all electrodes (see Figure 1.6),
2. the applied cell voltage V,
3. the geometry of the electrolyzer,
4. the electrical conductivity of the electrolyte σ^e, not necessarily constant.

And the unknown values are:

1. **the electrical potential field in the electrolyte Φ^e.**
2. **the value of the potential of the bipolar electrode V_b.**

2.1.4 Governing equations

Ohm's law gives the relationship between the electrical current density $\underline{i}$ and the electrical field $\underline{E}$: $\underline{i} = \sigma^e \underline{E}$
where σ^e is the electrical conductivity of the electrolyte.
Knowing that the electrical field derives from the potential Φ^e,
$\underline{E} = -\underline{grad}\,\Phi^e$, we obtain : $\underline{i} = -\sigma^e \underline{grad}\,\Phi^e$.
Then the conservation law of the electrical current, here, $div(\underline{i}) = 0$ gives for the electrolyte :

$$div(-\sigma^e \underline{grad}\,\Phi^e) = 0 \tag{2.1}$$

To describe the boundary conditions or interfaces electrodes-electrolyte conditions, we adopt the following conventions:

a) Electrolyte-insulator boundary.

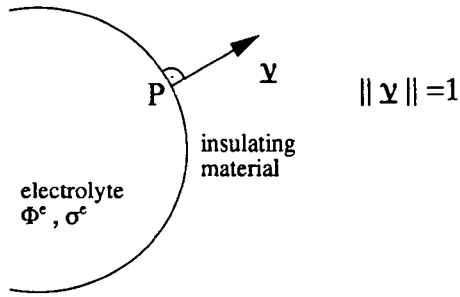

Figure 2.3: Electrolyte-insulator interface

$\underline{\nu}$: normal to the boundary pointed to the insulator; $\|\underline{\nu}\| = 1$.
The condition that there is no current crossing the boundary is expressed by:

$$\frac{d\Phi}{d\nu} = <\underline{i}\,|\,\underline{\nu}> = <-\sigma \underline{grad}\,\Phi(P)\,|\,\underline{\nu}> = 0 \tag{2.2}$$

b) Electrolyte-electrode boundary.

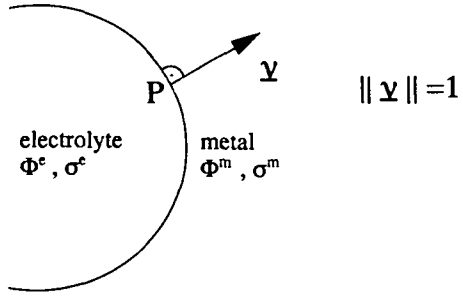

Figure 2.4: Electrolyte-metal interface

$\underline{\nu}$: normal to the boundary pointed to the metal; $\|\underline{\nu}\| = 1$.

$i = < \underline{i} \,|\, \underline{\nu} > :=$ current flow density crossing the interface at P.

The extended *Butler-Volmer* function defined in § 1.2.3 indicates the relationship between the current flow density and the potential jump at the interface. If Φ^m represents the potential of the metal, we have:

$$i = \varphi(\Phi^m - \Phi^e) \tag{2.3}$$

where $\varphi : \mathbb{R} \to \mathbb{R}$ is a non-decreasing, continuous and bounded function with $\varphi(0) = 0$.

So, with (2.3) and (2.2), at the interface, we have:

$$\boxed{-\sigma^e < \underline{grad}\,\Phi^e \,|\, \underline{\nu} >= \varphi(\Phi^m - \Phi^e)} \tag{2.4}$$

A bipolar electrode inside an electrolyzer under a difference of potential V, at the equilibrium state, with the preliminary hypothesis we have made, has its own constant potential V_b.
Then, the total current crossing the boundary Γ^m is null, there is current conservation crossing the interface.
The inlet current is equal to the outlet current and we have for **the bipolar electrode**:

$$\boxed{\int_{\Gamma^m} \varphi\,(V_b - \Phi^e)ds = 0} \tag{2.5}$$

Regrouping the equations (2.1), (2.2), (2.4) and (2.5), we obtain the differential (or classical) formulation of the problem that we call PROBLEM 1A and PROBLEM 1B:

The potential field Φ^e in the electrolyte and the value of the potential V_b of the bipolar electrode are solution of the following problem:

PROBLEM 1A : search Φ^e and V_b such that:

$$\left\{\begin{array}{lcll} div(\sigma^e \underline{grad}\,\Phi^e) & = & 0 & \text{in } \Omega^e \\ < \sigma^e \underline{grad}\,\Phi^e \,|\, \underline{\nu} > & = & 0 & \text{on } \Gamma_N \\ < \sigma^e \underline{grad}\,\Phi^e \,|\, \underline{\nu} > + \varphi\,(V - \Phi^e) & = & 0 & \text{on } \Gamma^1(V) \\ < \sigma^e \underline{grad}\,\Phi^e \,|\, \underline{\nu} > + \varphi\,(-\Phi^e) & = & 0 & \text{on } \Gamma^2(0) \\ < \sigma^e \underline{grad}\,\Phi^e \,|\, \underline{\nu} > + \varphi\,(V_b - \Phi^e) & = & 0 & \text{on } \Gamma^m \\ \displaystyle\int_{\Gamma^m} \varphi\,(V_b - \Phi^e) ds & = & 0 & \end{array}\right. \tag{2.6}$$

If Φ^m is the **imposed** known potential of the bipolar electrode, then the PROBLEM 1A is reduced to the PROBLEM 1B:

PROBLEM 1B : search Φ^e such that:

$$\left\{\begin{array}{lcll} div(\sigma^e \underline{grad}\,\Phi^e) & = & 0 & \text{in } \Omega^e \\ < \sigma^e \underline{grad}\,\Phi^e \,|\, \underline{\nu} > & = & 0 & \text{on } \Gamma_N \\ < \sigma^e \underline{grad}\,\Phi^e \,|\, \underline{\nu} > + \varphi\,(V - \Phi^e) & = & 0 & \text{on } \Gamma^1(V) \\ < \sigma^e \underline{grad}\,\Phi^e \,|\, \underline{\nu} > + \varphi\,(-\Phi^e) & = & 0 & \text{on } \Gamma^2(0) \\ < \sigma^e \underline{grad}\,\Phi^e \,|\, \underline{\nu} > + \varphi\,(\Phi^m - \Phi^e) & = & 0 & \text{on } \Gamma^m \end{array}\right. \tag{2.7}$$

In the formulations of the PROBLEM 1A and the PROBLEM 1B, Φ^e, its gradient and its second derivative must be continuous:

$$\Phi^e \in C^2(\Omega^e)$$

This strong condition is not natural for physical problems. To weaken this condition, we introduce a set H of **continuous** functions having a gradient and an energy:

$$\int_{\Omega^e} [|u^e|^2 + \| \underline{grad}\, u^e \|^2] \mathrm{d}\tau \text{ exists for all } u^e \in H.$$

H is in a certain sense, the set of all the possible potential functions on Ω^e.

2.1.5 Weak formulation of the problem

Then, (see Appendix A) the PROBLEM 2A, which is the weak formulation of the PROBLEM 1A, is :

PROBLEM 2A : find $\Phi^e \in H$ and $V_b \in \mathbb{R}$ such that:

$$\left\{\begin{array}{l} \displaystyle\int_{\Omega^e} \sigma^e \, < \, \underline{grad}\, \Phi^e \mid \underline{grad}\, u^e \, > d\tau \\ \\ \displaystyle + \int_{\Gamma^1(V)} \varphi\,(V \, - \, \Phi^e)\, u^e ds + \int_{\Gamma^2(0)} \varphi\,(-\,\Phi^e)\, u^e ds \\ \\ \displaystyle - \int_{\Gamma^m} \varphi\,(V_b \, - \, \Phi^e)\,(c^m - u^e) ds = 0 \\ \\ \text{for all } u^e \in H \text{ and } c^m \in \mathbb{R} \end{array}\right. \tag{2.8}$$

ds is the length element of the curve $\Gamma^1(V)$, $\Gamma^2(0)$ or Γ^m.

The weak formulation of the PROBLEM 1B is :

PROBLEM 2B : find $\Phi^e \in H$ such that:

$$\left\{\begin{array}{l} \displaystyle\int_{\Omega^e} \sigma^e \, < \, \underline{grad}\, \Phi^e \mid \underline{grad}\, u^e \, > d\tau \\ \\ \displaystyle + \int_{\Gamma^1(V)} \varphi\,(V \, - \, \Phi^e)\, u^e ds + \int_{\Gamma^2(0)} \varphi\,(-\,\Phi^e)\, u^e ds \\ \\ \displaystyle + \int_{\Gamma^m} \varphi\,(\Phi^m \, - \, \Phi^e)\, u^e ds = 0 \\ \\ \text{for all } u^e \in H \end{array}\right. \tag{2.9}$$

It is proved (see Appendix A) that the solution of the PROBLEM 2A, Φ^e and V_b verify, if $\Phi^e \in C^2$, all relations of the PROBLEM 1A, particularly the relation (2.5):

$$\int_{\Gamma^m} \varphi\,(V_b - \Phi^e) ds = 0$$

2.1.6 Variational form of the problem

Introducing a primitive of φ:

$$\psi\,(x) = \int_0^x \varphi\,(y)\,dy \tag{2.10}$$

Let J the following functional defined as:

$$\boxed{\begin{aligned} J(\Phi^m, u^e) = \frac{1}{2}\int_{\Omega^e} \sigma^e \|\underline{grad}\, u^e\|^2 d\tau \\ + \int_{\Gamma^1(V)} \psi(V - \Phi^e) ds + \int_{\Gamma^2(0)} \psi(-\Phi^e) ds \\ + \int_{\Gamma^m} \psi(\Phi^m - u^e) ds \end{aligned}} \tag{2.11}$$

$J(\Phi^m, u^e)$ is defined for all $\Phi^m \in \mathbb{R}$ and all $u^e \in H$.

$J(\Phi^m, u^e)$ measures the total virtual power of the cell if the potential is u^e and if Φ^m is the potential of the bipolar.

Then, under variational form, the PROBLEM 3A is:

PROBLEM 3A : find $\Phi^e \in H$ and $V_b \in \mathbb{R}$ which realized the minimum of $J(\Phi^m, u^e)$.

More precisely:

$$\boxed{J(V_b, \Phi^e) \leq J(\Phi^m, u^e)} \tag{2.12}$$

For all $\Phi^m \in \mathbb{R}$ and all $u^e \in H$.

It is proved (see Appendix A), that the PROBLEM 3A is an equivalent formulation of the PROBLEM 2A (2.8).

2.2 General model

We present here the general formulations (differential, weak and variational) of the PROBLEMS 1A, 1B, 2A, 2B and 3A for cells in two or three dimensions with several electrodes at a fixed known potential and several bipolar electrodes at an unknown floating potential.

2.2.1 Geometry

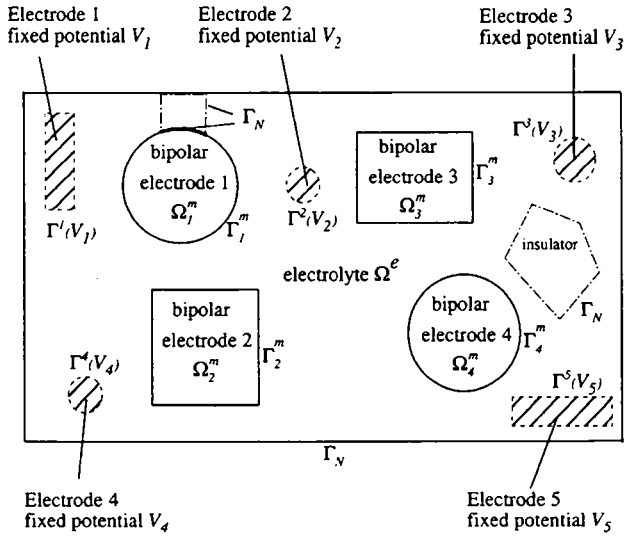

Figure 2.5: Section of a reactor with 5 current feeders and 4 bipolar electrodes

Figure 2.5 gives a representation of a section of a three-dimensional electrolyzer with electrodes at a fixed potential and bipolar electrodes. The following notations are adopted to design frontiers and regions:

1. Ω^e is the bounded domain of $\mathbb{R}^2$ or $\mathbb{R}^3$ occupied by the electrolyte.
2. N_f is the number of electrodes at a fixed known potential, in Figure 2.5, there are 5 electrodes: $N_f = 5$.
3. N_b is the number of the bipolar electrodes, in Figure 2.5, there are 4 bipolar electrodes: $N_b = 4$.
4. $\Gamma^i(V_i)$ is the part of the electrode i, $i = 1...N_f$ in contact with the electrolyte at the fixed potential V_i.
5. Ω_j^m is the domain occupied by the bipolar electrode j $j = 1...N_b$.
6. Γ_j^m is the frontier of Ω_j^m in contact with the electrolyte.
7. Γ_N is the part of the electrolyte in contact with an insulator, and the part of any electrode in contact with an insulator.

2.2.2 Parameters of the model

Accordingly to what has been developed in § 2.1.3, the parameters of the physic-chemical process are now:

1. the interface conditions parameters with the hypothesis that all electrodes are made of the same material, the extended *Butler-Volmer* characteristics is the same for all electrodes,
2. the fixed known potential V_i, $i = 1.., N_f$,
3. the geometry of the electrolyzer,
4. the electrical conductivity of the electrolyte σ^e (which is not necessarily constant).

And the unknown values are:

1. **the electrical potential field in the electrolyte Φ^e,**
2. **the value of the potentials of the bipolar electrodes** V_{b_j}, $j = 1, ..., N_b$.

2.2.3 Mathematical formulations

In this case, the generalized formulation of the PROBLEM 1A becomes:

PROBLEM 1A : search Φ^e and V_{b_j}, $(j = 1, ..., N_b)$ such that:

$$\left\{\begin{array}{lcll} div(\sigma^e \underline{grad}\,\Phi^e) & = & 0 & \text{in } \Omega^e \\ < \sigma^e \underline{grad}\,\Phi^e \,|\, \underline{\nu} > & = & 0 & \text{on } \Gamma_N \\ < \sigma^e \underline{grad}\,\Phi^e \,|\, \underline{\nu} > + \varphi\,(V_i - \Phi^e) & = & 0 & \text{on } \Gamma^i(V_i) \\ & & & i = 1, .., N_f \\ < \sigma^e \underline{grad}\,\Phi^e \,|\, \underline{\nu} > + \varphi\,(V_{b_j} - \Phi^e) & = & 0 & \text{on } \Gamma_j^m \\ & & & j = 1, .., N_b \\ \displaystyle\int_{\Gamma_j^m} \varphi\,(V_{b_j} - \Phi^e) ds & = & 0 & j = 1, .., N_b \end{array}\right. \tag{2.13}$$

Where V_{b_j}, $(j = 1, .., N_b)$ are the **floating** potential of each bipolar electrode j.

If Φ_j^m, $(j = 1, .., N_b)$ are the **imposed** known potentials of each bipolar electrode, then the general formulation of the PROBLEM 1B is:

PROBLEM 1B : search Φ^e such that:

$$\left\{\begin{array}{lcll} div(\sigma^e \underline{grad}\,\Phi^e) & = & 0 & \text{in } \Omega^e \\ < \sigma^e \underline{grad}\,\Phi^e \,|\, \underline{\nu} > & = & 0 & \text{on } \Gamma_N \\ < \sigma^e \underline{grad}\,\Phi^e \,|\, \underline{\nu} > + \varphi\,(V_i - \Phi^e) & = & 0 & \text{on } \Gamma^i(V_i) \\ & & & i = 1, .., N_f \\ < \sigma^e \underline{grad}\,\Phi^e \,|\, \underline{\nu} > + \varphi\,(\Phi_j^m - \Phi^e) & = & 0 & \text{on } \Gamma_j^m \\ & & & j = 1, .., N_b \end{array}\right. \tag{2.14}$$

The weak formulation of the PROBLEM 1A, becomes:

PROBLEM 2A : find $\Phi^e \in H$ and $V_{b_j} \in \mathbb{R}$, $(j = 1, ..., N_b)$ such that:

$$\left\{ \begin{array}{l} \displaystyle\int_{\Omega^e} \sigma^e < \underline{grad}\,\Phi^e \mid \underline{grad}\,u^e > d\tau + \sum_{i=1}^{N_f} \left[\int_{\Gamma^i(V_i)} \varphi\,(V_i - \Phi^e)\,u^e dS \right] \\ \\ \displaystyle -\sum_{j=1}^{N_b} \left[\int_{\Gamma_j^m} \varphi\,(V_{b_j} - \Phi^e)\,(c_j^m - u^e) dS \right] = 0 \\ \\ \text{for all } u^e \in H \text{ and } c_j^m \in \mathbb{R},\ j = 1, ..., N_b \end{array} \right. \tag{2.15}$$

The weak formulation of the PROBLEM 1B, becomes:

PROBLEM 2B : find $\Phi^e \in H$ such that:

$$\left\{ \begin{array}{l} \displaystyle\int_{\Omega^e} \sigma^e < \underline{grad}\,\Phi^e \mid \underline{grad}\,u^e > d\tau + \sum_{i=1}^{N_f} \left[\int_{\Gamma^i(V_i)} \varphi\,(V_i - \Phi^e)\,u^e dS \right] \\ \\ \displaystyle +\sum_{j=1}^{N_b} \left[\int_{\Gamma_j^m} \varphi\,(\Phi_j^m - \Phi^e)\,u^e dS \right] = 0 \\ \\ \text{for all } u^e \in H \end{array} \right. \tag{2.16}$$

Then the functional $J(\Phi^m, u^e)$ given in (2.11) becomes:

$$\boxed{\begin{aligned} J(\Phi_1^m, .., \Phi_j^m, .., \Phi_{N_b}^m, u^e) &= \frac{1}{2}\int_{\Omega^e} \sigma^e \|\underline{grad}\, u^e\|^2 d\tau \\ &+ \sum_{i=1}^{N_f}\left[\int_{\Gamma^i(V_i)} \psi(V_i - u^e) ds\right] + \sum_{j=1}^{N_b}\left[\int_{\Gamma_j^m} \psi(\Phi_j^m - u^e) ds\right] \end{aligned}} \tag{2.17}$$

and the PROBLEM 3A is :

PROBLEM 3A : find $\Phi^e \in H$ and V_{b_j}, $(j = 1, ..., N_b) \in \mathbb{R}$ which realized the minimum of $J(\Phi_1^m, .., \Phi_j^m, .., \Phi_{N_b}^m, u^e)$.

More precisely:

$$\boxed{\begin{aligned} J(V_{b_1}, .., V_{b_j}, .., V_{b_{N_b}}, u^e) \leq J(\Phi_1^m, .., \Phi_j^m, .., \Phi_{N_b}^m, u^e) \\ \text{for all } \Phi_j^m \in \mathbb{R} \text{ and all } u^e \in H \\ j = 1, ..., N_b \end{aligned}} \tag{2.18}$$

Chapter 3

Finite Element Approximation and Numerical Solving

The problem as formulated in the preceding chapter cannot be solved analytically. To solve this problem, numerical methods are employed. This problem has to be transformed into a numerical form. This has been achieved using a finite element method.

This chapter presents the approached problem of the exact problem and its numerical solving.

In the first part of the chapter, we describe how the approximation of domains is made and what type of finite element has been employed to discretize two and three-dimensional geometries of electrochemical reactors.

Afterwards, the transformation of the weak formulation (PROBLEM 2B (2.16)) presented in the chapter 2 to a non-linear system of equations is detailed for two and three-dimensional discretized domains. The case which is treated here is when the potentials of the bipolar electrodes are known.

Then, the numerical solving procedure is given in this case, and the method of numerical solving of the non-linear system of equations is fully detailed.

In § 3.4, the method of determination of the bipolar electrodes potentials is detailed: we used an iterative method (method of descent)

to minimize an approached functional of the functional J (Eq. (2.17)) as defined in § 2.2.3.

Note that the method that has developed here is general: it handles geometries in two and three dimensions. There is a complete analogy between 2D and 3D problems. Except the computation of elementary stiffness matrices (§ 3.2.1), the assembly procedure is the same, the storage is the same and the methods of solving the systems of equations are identical.

However, in the last section, we describe another finite element approximation which has been developed for particular geometries (electrolyzer hydrogen producer from [ALY]) made of stacking of layers. For this application, taking into account the cylindrical symmetry of the cell and the superposition of the different layers, the description of the modelling such electrolyzers has been undertaken. This finite element approximation is different from the previous one: not only the elementary stiffness matrices are naturally different but also the storage of the over-all matrices is optimized and we have employed iterative methods for the numerical solving of linear systems of equations.

3.1 Domain approximation

3.1.1 Two-dimensional geometries

We subdivide the domain Ω^e into a finite number of subregions, the finite elements. We chose triangular elements: it permits to mesh any kind of geometric forms and the interface between two environments is a polygonal line made of edges of some triangles (Figure 3.3).

A triangulation on Ω^e is a family of triangles T_{el_k}, $k = 1, \ldots, n_t$ satisfying some of the following constraints:

1. the intersection of two distinct triangles must either be empty, either be reduced to a edge or a point.
2. $\Omega_h^e = \bigcup_{k=1}^{k=n_t} T_{el_k}$;
3. triangles are of non null surface.

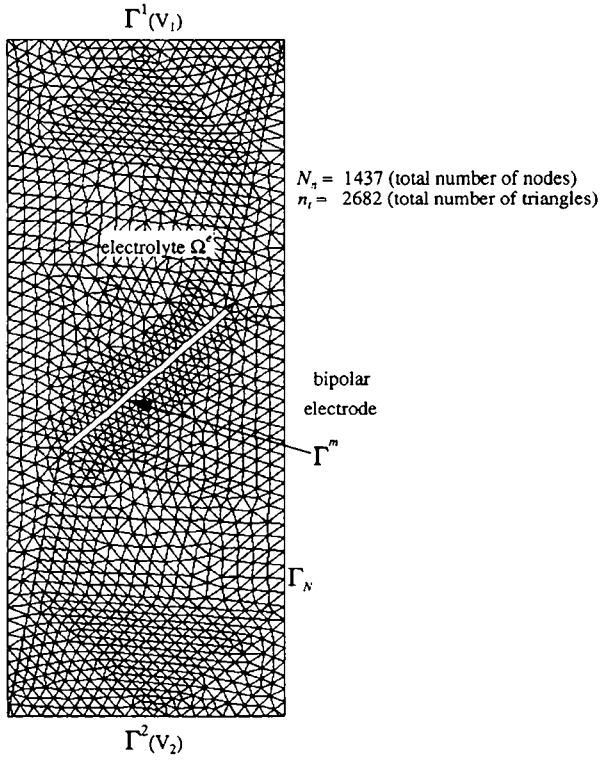

Figure 3.1: A triangulation of Ω^e

That triangulation on Ω^e noted Ω^e_h is indexed by h. h is the biggest diameter of the circumcircle of all the triangles forming the triangulation.

We use linear, affine functions on triangles. An approximation of the solution on a triangle is defined by the values of this approximation on the three vertices of the triangle (Figure 3.2).
On the full discretized domain (Figure 3.1), an approached solution is defined by the set of values on each node (or vertice) of the triangulation. N_n is the number of nodes of the triangulation.

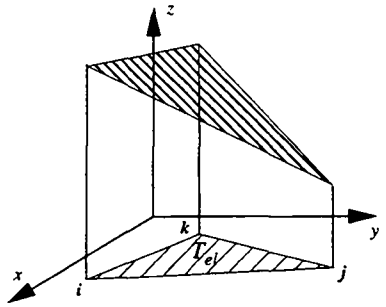

Figure 3.2: Graph of the affine function defined on T_{el}

These values are contained in a vector where each component represents the nodal value. Nodes are numbered and the k^{th} vector's component is the value of the potential at the node k.

Note that in Figure 3.1, because the electrodes are considered as equipotential, they are not meshed, but there are nodes on each interface electrode-electrolyte where the current-potential function makes the link between the two environments.

3.1.2 Three-dimensional geometries

The domain Ω^e is three-dimensional and we have chosen the three-dimensional equivalent of the plane triangle which is the tetrahedral element as shown in Figure 3.4 to divide the domain into a finite number of subregions. This element permits to mesh any kind of geometric forms and the interface between two environments are always a surface made of triangles which are the sides of the tetrahedra. (see Figure 3.5)

Similarly to the 2D geometries, we use linear, affine functions on the tetrahedra, and an approximation of the solution on a tetrahedral element is defined by the values of this approximation on the four vertices of the tetrahedra.

On the full discretized domain, an approached solution is defined by the set of values on each node (or vertice) of the discretization.

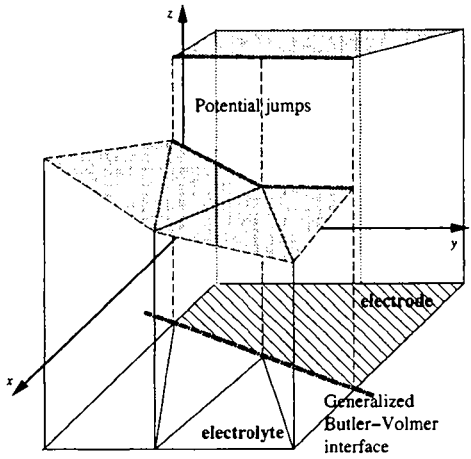

Figure 3.3: Approached solution : typical polyhedral representation

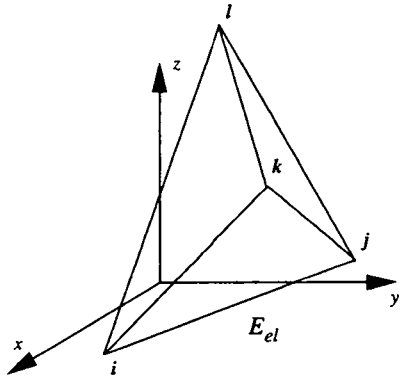

Figure 3.4: Tetrahedral element

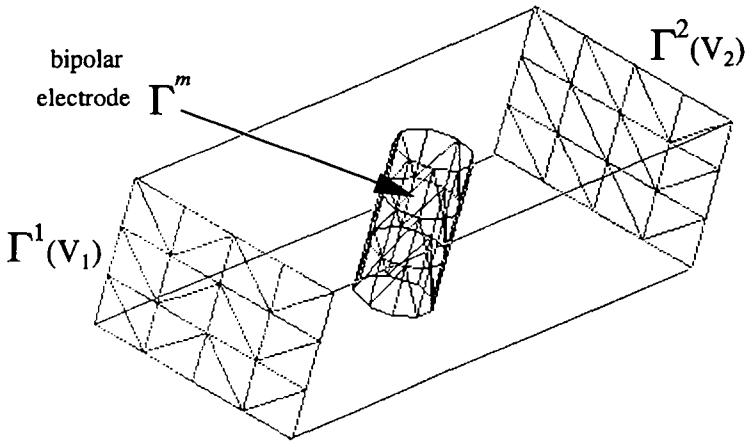

Figure 3.5: 3D geometry with boundaries electrodes - electrolyte

3.2 Transformation into matrix form

In this part, the transformation of the formulation of the PROBLEM 2B (2.16) to a numerical form that we will able to program is described.

We explain firstly how, doing the hypothesis that the potential of each bipolar is known, the PROBLEM 2B (2.16) is transformed into a non-linear system of equations.

In the following, we consider any two or three-dimensional electrolyzer with :

1. N_f electrodes at a fixed known potential V_i for $i = 1, .., N_f$
2. N_b bipolar electrodes where each potential Φ_j^m for $j = 1, .., N_b$ has already been determined and fixed (for instance using the method given in § 3.4).

The formulation of the PROBLEM 2B (2.16) is the most adapted to the finite element method. Using the domain approximation of the preceding section, the problem can be approached in the following manner:
the piecewise linear functions (polyhedral graph in 2D) used are totally described by the vector of nodes values. Furthermore, These functions belong to the set of functions H.

Re-taking the weak formulation of the PROBLEM 2B, with [Fro], the first term of (2.16) :

$$\int_{\Omega^e} \sigma^e < \underline{grad}\, \Phi^e \mid \underline{grad}\, u^e > d\tau$$

has a value which can be approached by:

$$< \mathbf{A}\, \underline{\Phi}^e \mid \underline{u}^e >$$

where $\mathbf{A}$ is a square symmetric matrix of size N_n.
N_n is the number of nodes of the discretization of Ω^e.
This matrix is a function of the coordinates of the nodes and the conductivity σ^e.

$$\underline{\Phi}^e = \begin{pmatrix} \underline{\Phi}^e(1) \\ \underline{\Phi}^e(2) \\ \cdot \\ \cdot \\ \underline{\Phi}^e(i) \\ \underline{\Phi}^e(N_n) \end{pmatrix} \text{ and } \underline{u}^e = \begin{pmatrix} \underline{u}^e(1) \\ \underline{u}^e(2) \\ \cdot \\ \cdot \\ \underline{u}^e(i) \\ \underline{u}^e(N_n) \end{pmatrix}$$

are the vectors of N_n components containing the nodal potential value.
$\mathbf{A}$, the stiffness matrix obtained by assembling elementary stiffness matrices calculated as following depending on the element. The assembly procedure is given in § 3.2.4.
The computation of the stiffness matrices are detailed below for triangular and tetrahedra elements.

3.2.1 2D elementary stiffness matrix computation

From [Fro], the following integral can be evaluated on a triangle T_{el} of vertices i, j, k (Figure 3.1) as:

$$\int_{T_{el}} < \underline{grad}\, \Phi^e | \underline{grad}\, u^e > dA \approx \frac{1}{4|T_{el}|} (\underline{\Phi}^e(i), \underline{\Phi}^e(j), \underline{\Phi}^e(k)) \mathcal{M} \begin{pmatrix} \underline{u}^e(i) \\ \underline{u}^e(j) \\ \underline{u}^e(k) \end{pmatrix} \tag{3.1}$$

By $\approx$, we mean "can be approached by".

$$\mathcal{M} = \begin{pmatrix} y_{32}^2 + x_{32}^2 & y_{32}y_{13} + x_{32}x_{13} & y_{32}y_{21} + x_{32}x_{21} \\ y_{13}y_{32} + x_{13}x_{32} & y_{13}^2 + x_{13}^2 & y_{13}y_{21} + x_{13}x_{21} \\ y_{21}y_{32} + x_{21}x_{32} & y_{21}y_{13} + x_{21}x_{13} & y_{21}^2 + x_{21}^2 \end{pmatrix}$$

and with $x_{mn} = x_m - x_n$, $y_{mn} = y_m - y_n$

and $|T_{el}| = \frac{1}{2}\begin{vmatrix} x_i & x_j & x_k \\ y_i & y_j & y_k \\ 1 & 1 & 1 \end{vmatrix}$

Therefore, the transformation of the preceding integral on a triangle T_{el} into a matrix form gives :

$$\boxed{\sigma^e \int_{T_{el}} < \underline{grad}\,\Phi^e | \underline{grad}\,u^e > dA \approx < \mathbf{a}_{el}\,\underline{\Phi}^e | \underline{u}^e >} \tag{3.2}$$

with $\mathbf{a}_{el}$ is a 3×3 symmetric matrix called the elementary stiffness matrix for the triangle T_{el}.

$$\boxed{\mathbf{a}_{el_{i,j}} = \frac{\sigma^e}{4|T_{el}|}\mathcal{M}_{ij}} \tag{3.3}$$

3.2.2 3D elementary stiffness matrix computation

On a tetrahedra E_{el} of vertices i, j, k, l (Figure 3.4), from [Dav86], the integral $\int_{E_{el}} < \underline{grad}\,\Phi^e | \underline{grad}\,u^e > d\tau$ can be approached by:

$$< \mathbf{a}_{el}\,\underline{\Phi}^e | \underline{u}^e > \tag{3.4}$$

where in this case, $\mathbf{a}_{el}$ is a 4×4 symmetric matrix of the tetrahedral element E_{el}.

Each term $\mathbf{a}_{el_{i,j}}$ of this matrix is calculated as following:

$$\boxed{\mathbf{a}_{el_{i,j}} = \frac{\sigma^e}{36V}(b_i b_j + c_i c_j + d_i d_j)} \tag{3.5}$$

where $b_i = -\begin{vmatrix} 1 & y_j & z_j \\ 1 & y_k & z_k \\ 1 & y_l & z_l \end{vmatrix}$, $c_i = -\begin{vmatrix} x_j & 1 & z_j \\ x_k & 1 & z_k \\ x_l & 1 & z_l \end{vmatrix}$,

$d_i = -\begin{vmatrix} x_j & y_j & 1 \\ x_k & y_k & 1 \\ x_l & y_l & 1 \end{vmatrix}$ and $V = \begin{vmatrix} x_i & y_i & z_i & 1 \\ x_j & y_j & z_j & 1 \\ x_k & y_k & z_k & 1 \\ x_l & y_l & z_l & 1 \end{vmatrix}$

3.2.3 Interfacial terms

The other terms of the formulation (2.16) concern the interface conditions. With the hypothesis that each potential is known, in (2.16), we have a sum of integrals, where each integral is under the form :

$$\int_{\Gamma} \varphi\,(V - \Phi^e)\,u^e dS \tag{3.6}$$

Γ is a boundary of the type $\Gamma^i(V_i)$ or Γ_j^m.
V is the fixed known potential of a given electrode.

To evaluate this integral for a given electrode, we compute the contribution of each node at a metal-electrolyte interface.

dS is the length element for 2D problems and dS is the surface element in 3D problems.

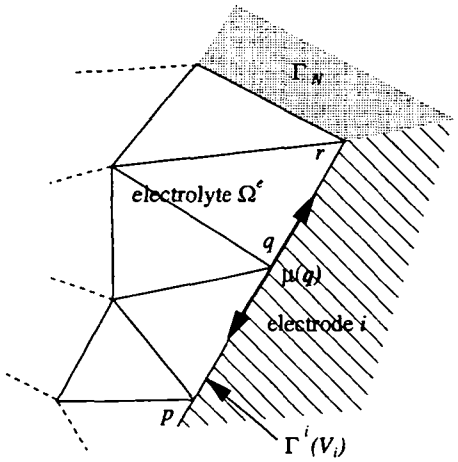

Figure 3.6: Computation of $\mu(q)$ on Γ (2D case)

For the node $q \in \Gamma \in \mathbb{R}^2$, as shown in Figure 3.6, its contribution to the integral (3.6) gives:

$$\varphi(V - \underline{\Phi}^e(q))\,\underline{u}^e(q)\,\mu(q) \tag{3.7}$$

where

$$\mu(q) = \frac{1}{2}(|pq| + |qr|)$$

p and r are the neighbor vertices of q on the interface $\Gamma^i(V_i)$ as shown in Figure 3.6.
If we consider the node r (in the corner, in contact with an insulator):

$$\mu(r) = \frac{1}{2}|qr|.$$

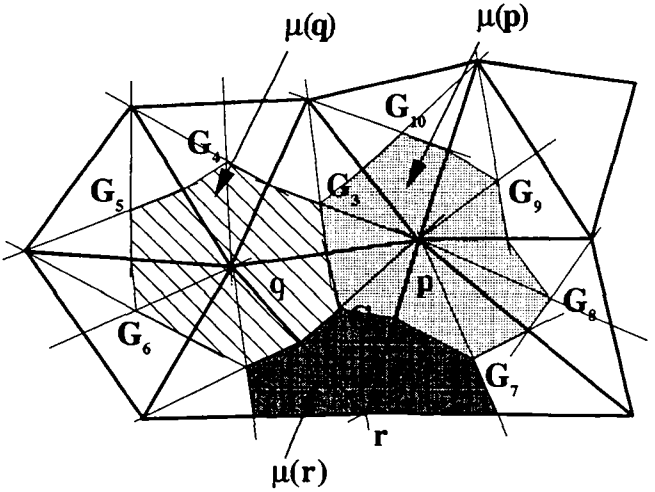

Figure 3.7: Computation of $\mu(q)$ on Γ (3D case)

For the node $q \in \Gamma \in \mathbb{R}^3$ as shown in Figure 3.7, its contribution to the integral (3.6) is the same as (3.7):

$$\varphi\,(V - \underline{\Phi}^e(q))\,\underline{u}^e(q)\,\mu(q)$$

and in this case

$$\mu(q) = \frac{1}{3}[\text{sum of the areas of the triangles having } q \text{ in common}]$$

To determine the third of the area of each triangle, the gravity center G_i each triangle is used as shown in Figure 3.7.

Then we approach $\int_\Gamma \varphi\,(V - \Phi^e)\,u^e dS$ by:

$$\sum_{q\in\Gamma} \varphi\,(V - \Phi^e)\mu(q)\underline{u}^e(q)$$

which we rewrite: $- < \underline{\mathbf{B}}_\Gamma(\underline{\Phi}^e)|\underline{u}^e >$

$\underline{\mathbf{B}}_\Gamma(\underline{\Phi}^e)$ is a vector depending on the interface Γ. Its number of components is the number of nodes of the discretization of Γ.

To take in account **each** interface electrode-electrolyte Γ of the type $\Gamma^i(V_i)$ or Γ_j^m, we build a vector $\underline{\mathbf{B}}(\underline{\Phi}^e)$ of N_n components having the following form:

$$\underline{\mathbf{B}}(\underline{\Phi}^e) = \left.\begin{pmatrix} 0 & \leftarrow \text{node} \notin \Gamma \\ \vdots & \\ -\mu(p)\varphi\,(V_1 - \underline{\Phi}^e(p)) & \leftarrow \text{node}\, p \in \Gamma^1(V_1) \\ \vdots & \\ -\mu(q)\varphi\,(\Phi_1^m - \underline{\Phi}^e(q)) & \leftarrow \text{node}\, q \in \Gamma_1^m \\ \vdots & \\ 0 & \leftarrow \text{node} \notin \Gamma \\ -\mu(r)\varphi\,(\Phi_1^m - \underline{\Phi}^e(r)) & \leftarrow \text{node}\, r \in \Gamma_1^m \\ 0 & \leftarrow \text{node} \notin \Gamma \\ -\mu(s)\varphi\,(\Phi_j^m - \underline{\Phi}^e(s)) & \leftarrow \text{node}\, s \in \Gamma_j^m \\ 0 & \leftarrow \text{node} \notin \Gamma \\ -\mu(t)\varphi\,(V_2 - \underline{\Phi}^e(t)) & \leftarrow \text{node}\, t \in \Gamma^2(V_2) \\ \vdots & \end{pmatrix}\right\} N_n$$

3.2.4 Assembly procedure

Let $\mathcal{T}^e$ the set of all the elements mapping $\Omega^e \in \mathbb{R}^2$ or $\mathbb{R}^3$.
$T^i(V_i)$ the set of all the faces mapping $\Gamma^i(V_i) \in \mathbb{R}$ or $\mathbb{R}^2$.
Then the PROBLEM 2B (2.16) is approached by:

$$\begin{cases} \displaystyle\sum_{\tau \in \mathcal{T}^e} \int_\tau \sigma^e < \underline{grad}\,\Phi^e \mid \underline{grad}\,u^e > d\tau \\ \\ \displaystyle -\sum_{i=1}^{N_f} \left[\sum_{T \in T_{i(V_i)}} \int_T \varphi\,(V_i - \Phi^e)\, u^e dS \right] \\ \\ \displaystyle -\sum_{i=1}^{N_b} \left[\sum_{T \in T_{i(V_i)}} \int_T \varphi\,(\Phi_i^m - \Phi^e)\, u^e dS \right] = 0 \\ \\ \text{for all } u^e \in H \end{cases} \tag{3.8}$$

which can be rewritten with (3.4) and (3.8):

$$\sum_{\tau \in \mathcal{T}^e} < \mathbf{a}_{el_\tau} \underline{\Phi}^e \,|\, \underline{u}^e > \; + \; < \underline{\mathbf{B}}\,(\underline{\Phi}^e) \,|\, \underline{u}^e >= 0 \tag{3.9}$$

which gives:

$$< \mathbf{A}\,\underline{\Phi}^e \,|\, \underline{u}^e > + < \underline{\mathbf{B}}(\underline{\Phi}^e) \,|\, \underline{u}^e >= 0 \tag{3.10}$$

Finally, the PROBLEM 2B (Eq. 2.16) is transformed into:

Find $\underline{\Phi}^e$, solution of the system:

$$\boxed{\mathbf{A}\,\underline{\Phi}^e + \underline{\mathbf{B}}(\underline{\Phi}^e) = 0} \tag{3.11}$$

1. The over-all stiffness matrix noted $\mathbf{A}$, for both 2D and 3D cases, is built by adding together all contributions of elementary matrices $\mathbf{a}_{el}$ where the nodes i and j appear to the i, j position of $\mathbf{A}$. $\mathbf{A}$ is a symmetric matrix, it is also sparse since the i, j location contains a non-zero element only when nodes i and j are in the same element. For a system with a large number of elements most of $\mathbf{A}$ will be zero.

   Next chapter deals with the storage of such matrices in order to reduce memory occupation and therefore time computation.

2. (3.11) is a system of non-linear equations, composed of a linear part $\mathbf{A}\,\underline{\Phi}^e$, coming from the electrolyte and a non-linear part, $\underline{\mathbf{B}}(\underline{\Phi}^e)$, vector of N_n components. Most of its components of are null, the only non-null values are those coming from interfaces where an extended *Butler-Volmer* condition is fixed.

The numerical solving of the non-linear system (3.11) is fully detailed in § 3.3.

To illustrate the form of the non-linear system of equations that we have obtained, we consider the part of the mesh in Figure 3.8. Some nodes of a triangulation are shown and we express the second and the third line of the system (3.11) of equations.
The second line of the system of equations (corresponding to the node 2) is, in this case:

$$\begin{cases} \mathbf{A}_{2,1}\underline{\Phi}^e(1) + \mathbf{A}_{2,2}\underline{\Phi}^e(2) + \mathbf{A}_{2,3}\underline{\Phi}^e(3) + \mathbf{A}_{2,4}\underline{\Phi}^e(4) + \\ \mathbf{A}_{2,5}\underline{\Phi}^e(5) + \mathbf{A}_{2,6}\underline{\Phi}^e(6) + \mathbf{A}_{2,7}\underline{\Phi}^e(7) = 0 \end{cases} \tag{3.12}$$

This is an equation relative to a node in the electrolyte.
For a node at the interface $\Gamma^i(V_i)$, we have, for the equation relative to the node 3:

$$\begin{cases} \mathbf{A}_{3,2}\underline{\Phi}^e(2) + \mathbf{A}_{3,3}\underline{\Phi}^e(3) + \mathbf{A}_{3,5}\underline{\Phi}^e(5) + \\ \mathbf{A}_{3,7}\underline{\Phi}^e(7) - \mu(3)\varphi(V_i - \underline{\Phi}^e(3)) = 0 \end{cases} \tag{3.13}$$

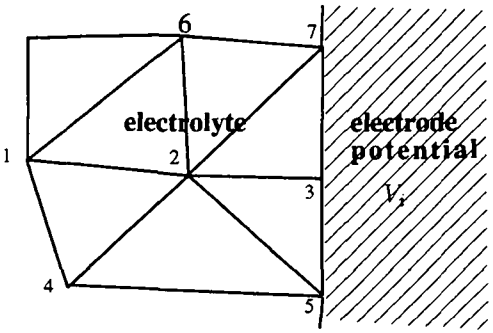

Figure 3.8: Part of a mesh with interfacial nodes

Important remark

As shows Eq. (3.13), the component k of $\mathbf{B}(\underline{\Phi}^e)$ depends **only** on the contribution $(-\mu(k)\varphi(V_i - \underline{\Phi}^e(k))$ of this node and any other one. This is very important for the numerical solving of the system (3.11).

3.3 Numerical solving of the non-linear system

The procedure to solve the system (Eq. 3.11) is described below, particularly the non-linear system which represents the more delicate part of the problem.
$\mathbf{A}\,\underline{\Phi}^e + \underline{\mathbf{B}}(\underline{\Phi}^e) = 0$ is a non-linear part composed N_n equations.
$\mathbf{A}$ is a sparse, symmetric, $N_n \times N_n$ matrix, the term $\mathbf{A}\,\underline{\Phi}^e$ is the linear part of the whole system coming from the discretized domain Ω_h^e of conductivity σ^e.
$\underline{\mathbf{B}}(\underline{\Phi}^e)$ is a vector of N_n components, coming from metal-solution conditions and includes the participation of the fixed potential values V_i and the bipolar electrodes potential values Φ_i^m $(i = 1..N_b)$.

3.3.1 Algorithm of the numerical solving

The method described here is based on a non-linear alternating direction method proposed by [Kel69]. We refer in the following of this work as Method of *Kellogg*.
This iterative method has the following scheme:

1. **We choose a parameter $\lambda > 0$.**

2. **From an initial vector $\underline{\Phi}_0^e$ we build two sequences $\underline{\Phi}_n^e$ and $\underline{\Phi}_{n+\frac{1}{2}}^e$**

$$\lambda[\underline{\Phi}_{n+\frac{1}{2}}^e - \underline{\Phi}_n^e] \quad + \mathbf{A}\,\underline{\Phi}_{n+\frac{1}{2}}^e + \underline{\mathbf{B}}\,(\underline{\Phi}_n^e) \quad = \underline{0} \qquad (3.14)$$

$$\lambda[\underline{\Phi}_{n+1}^e - \underline{\Phi}_{n+\frac{1}{2}}^e] + \mathbf{A}\,\underline{\Phi}_{n+\frac{1}{2}}^e + \underline{\mathbf{B}}\,(\underline{\Phi}_{n+1}^e) = \underline{0} \qquad (3.15)$$

Under some conditions on φ (satisfied here for large enough potentials), we have:

$$\lim_{n\to\infty} \underline{\Phi}_n^e = \lim_{n\to\infty} \underline{\Phi}_{n+\frac{1}{2}}^e = \underline{\Phi}^e$$

with $\underline{\Phi}^e$ solution of the non-linear system $\mathbf{A}\,\underline{\Phi}^e + \underline{\mathbf{B}}(\underline{\Phi}^e) = 0$

3. **First computation**

The equation (3.14) can be rewritten:

$$(\lambda I + \mathbf{A})\,\underline{\Phi}^e_{n+\frac{1}{2}} = \lambda\,\underline{\Phi}^e_n - \underline{\mathbf{B}}\,(\underline{\Phi}^e_n) \tag{3.16}$$

(I : unit matrix N_h x N_h)
knowing $\underline{\Phi}^e_n$, (3.16) allows the computation of $\underline{\Phi}^e_{n+\frac{1}{2}}$ by solving the linear system.

4. **Second computation**

The equation (3.15) can be rewritten:

$$\lambda\,\underline{\Phi}^e_{n+1} + \underline{\mathbf{B}}\,(\underline{\Phi}^e_{n+1}) = (\lambda I - \mathbf{A})\,\underline{\Phi}^e_{n+\frac{1}{2}} \tag{3.17}$$

This is a non-linear system of equations for $\underline{\Phi}^e_{n+1}$.
$\underline{\Phi}^e_{n+\frac{1}{2}}$ has been obtained with (3.16) from the first computation.

For a node q at the interface electrode-electrolyte $\Gamma^i(V_i)$, we note:

$$\underline{g}(q) = (\lambda I + \mathcal{A})\,\underline{\Phi}^e_{n+\frac{1}{2}}(q)$$

The potential of a bipolar electrode i is fixed and is equal to V_i.
The potential at the node q in the electrolyte is $\underline{\Phi}^e(q)$.

With (3.7), $\underline{\mathbf{B}}\,(\underline{\Phi}^e(q))$ becomes: $-\mu(q)\varphi\,(V_i - \underline{\Phi}^e(q))$

and finally, we have to solve the following equation in each node of the interface Γ^m

$$\lambda\,\underline{\Phi}^e(q) - \mu(q)\varphi\,(V_i - \Phi^e(q)) = \underline{g}(q) \tag{3.18}$$

This equation is of the type: $\lambda x - \mu\varphi(a - x) = b$

with: $x = \underline{\Phi}^e(q)$, $a = V_i$, and $b = \underline{g}(q)$

5. **Solve** $\lambda x - \mu\varphi(a - x) = b$

We describe in § 3.3.2 the method used to solve this equation.

3.3.2 Solving an equation of the type $\lambda x - \mu\varphi(a - x) = b$

$$\lambda x - \mu\varphi(a - x) = b \tag{3.19}$$

λ and μ are two positive real numbers.
a et b are two real numbers.
φ is an interfacial function such as described in § 1.2. It is a non-decreasing, continuous and bounded function. An example is given in Figure 3.9.

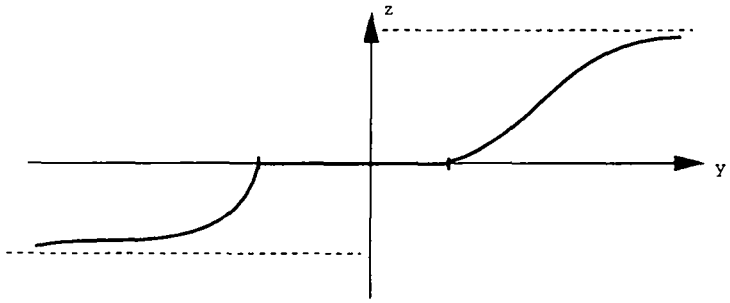

Figure 3.9: Typical graph of $y \longmapsto \varphi(y)$

(3.19) has always an unique solution that we compute in the following manner:

Let $y = a - x$.
Then, (3.19) becomes:

$$\lambda a - \lambda y - \mu\varphi(y) = b$$

or

$$\varphi(y) = -\frac{\lambda}{\mu}y + \frac{\lambda a - b}{\mu} \tag{3.20}$$

The solution of (3.20) is the intersection of the curve $\mathcal{C}$ of equation $z = \varphi(y)$ and d of equation $z = -\frac{\lambda}{\mu}y + \frac{\lambda a - b}{\mu}$.

Because the slope of d is always negative, the intersection of d and C is always reduced to a point. The retained method takes in account three factors:

1. φ is not differentiable in every point.
2. φ is difficult to define.
3. The solving of this equation is computed a very large number of times.

We replace C by a polygonal line and the solution is the intersection of this line with a straight line.

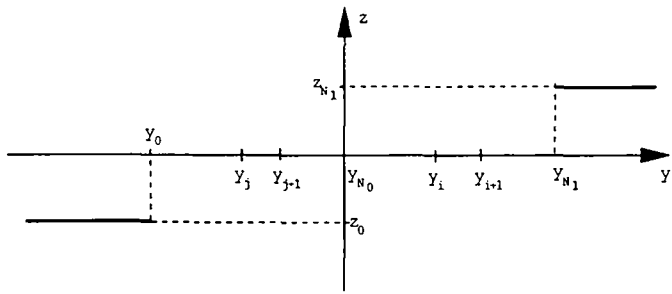

Figure 3.10: Approximation of C ($z = \varphi(y)$) by a polygonal line

$$y_0 < y_1 < ... < y_j < ... < y_{N_0} < ... < y_i < ... < y_{N_1}$$

$$z_k = \varphi(y_k)$$

$$z_0 \leq z_1 \leq ... \leq ...z_j \leq ... \leq z_{N_0} \leq ... \leq z_i \leq ... \leq z_{N_1}$$

Then this new function φ is defined by:

$$\varphi(y) = \begin{cases} z_{N_1} & \text{if } y \geq y_{N_1} \\ z_i + m_i(y - y_i) & \text{if } y_i \leq y < y_{i+1}, i = 0, 1, ..., (N_1 - 1) \\ z_0 & \text{si } y < y_0 \end{cases}$$

with

$$m_i = \frac{z_{i+1} - z_i}{y_{i+1} - y_i}$$

To find the intersection of d and $\mathcal{C}$:

$$\begin{cases} z = \varphi(y) & : \mathcal{C} \\ \frac{z}{\frac{\lambda a - b}{\mu}} + \frac{y}{\frac{\lambda a - b}{\lambda}} = 1 & : d \end{cases}$$

Defining the following segments, we search which segment d crosses.

$$\begin{aligned} &S_i = [(y_i, z_i); (y_{i+1}, z_{i+1})];\ i = 0, 1, ..., (N_1 - 1) \\ &S_{-1} =](-\infty; z_0); (y_0, z_0)]; \\ &S_{N_1} = [(y_{N_1}, z_{N_1}) : (+\infty; z_{N_1})[, \end{aligned}$$

Introducing the function $\Phi(y, z) = \lambda y + \mu z - (\lambda a - b)$, the equation of d is: $\Phi(y, z) = 0$
Then the algorithm of researching the solution is:

IF $\lambda a - b > 0$
$i = N_0 - 1$
LABEL
$i := i + 1$
$\Phi_i = \Phi(y_i, z_i); \Phi_{i+1} = \Phi(y_{i+1}, z_{i+1})$
if $\Phi_i = 0, (y_i, z_i)$ is the solution $\longmapsto$END.
if not
if $\Phi_{i+1} = 0, (y_{i+1}, z_{i+1})$ is the solution $\longmapsto$ END
else
if $\Phi_i \Phi_{i+1} < 0$, d cuts S_i: solution 1: $\longmapsto$ END
else
if $i + 1 < N_1$ Return LABEL
else:
$i + 1 = N_1$; d cuts S_{N_1}: solution 2 $\longmapsto$ END

IF $\lambda a - b < 0$
$i = -1$
LABEL
$i := i + 1$
$\Phi_i = \Phi(y_i, z_i); \Phi_{i+1} = \Phi(y_i, z_i)$
if $\Phi_0 > 0$, d cuts S_{-1}: solution 3: $\longmapsto$ END
else
if $\Phi_i = 0$, $(y_i, z_i))$ is solution: $\longmapsto$ END
else
if $\Phi_{i+1} = 0, (y_{i+1}, z_{i+1})$ is solution: $\longmapsto$ END
else
if $\Phi_i \Phi_{i+1} < 0$, d cuts S_i: solution1: $\longmapsto$ END
else Return LABEL

Solution 1: intersection of S_i and d: (y_s, z_s) or (x_s, z_s) with $x_s = a - y_s$.

$$\begin{cases} z &= z_i + m_i(y - y_i) \\ z &= \dfrac{\lambda}{\mu} y + \dfrac{\lambda a - b}{\mu}; \end{cases}$$

$$\begin{cases} x_s &= \dfrac{\mu m_i (a - y_i) + b + \mu z_i}{\mu m_i + \lambda} \\ z_s &= \dfrac{\lambda m_i (a - y_i) - m_i b + \lambda z_i}{\mu m_i + \lambda}; \end{cases}$$

Solution 2

$y \geq y_{N_1}$; $z_s = z_{N_1}$; $x_s = a - y_s$

$$\left\| \begin{array}{rcl} x_s & = & \dfrac{\mu}{\lambda} z_{N_1} + \dfrac{b}{\lambda} \\ z_s & = & z_{N_1} \\ y_s & = & -\dfrac{\mu}{\lambda} z_{N_1} + \dfrac{\lambda a - b}{\lambda}. \end{array} \right.$$

Solution 3

$y < y_0$;, $z_s = z_0$

$$\left\| \begin{array}{rcl} x_s & = & \dfrac{\mu}{\lambda} z_0 + \dfrac{b}{\lambda} \\ z_s & = & z_0 \\ y_s & = & -\dfrac{\mu}{\lambda} z_0 + \dfrac{\lambda a - b}{\lambda}. \end{array} \right.$$

3.4 Determination of the bipolar electrodes potential

To determine the potential V_{b_j} of each bipolar electrode $j = 1, .., N_b$, we define the numerical approximation $\mathcal{J}$ of the functional J (2.18).

$$\mathcal{J}(\Phi_1^m, \Phi_2^m, ..., \Phi_{N_b}^m, \underline{u}^e) \approx J(\Phi_1^m, \Phi_2^m, ..., \Phi_{N_b}^m, u^e) \tag{3.21}$$

And to determine the N_b unknown values of the potential V_{b_j} of the bipolar electrodes and the potential distribution $\underline{\Phi}^e$) in the electrolyte, we have to find the minimum of $\mathcal{J}(\Phi_1^m, \Phi_2^m, ..., \Phi_{N_b}^m, \underline{u}^e)$ as formulated in PROBLEM 3A (2.18):

$$\boxed{\begin{array}{l} \mathcal{J}(V_{b_1}, V_{b_2}, ..., V_{b_{N_b}}, \underline{\Phi}^e) < \mathcal{J}(\Phi_1^m, \Phi_2^m, ..., \Phi_{N_b}^m, \underline{u}^e) \\ \\ \text{for all } \Phi_j^m \ (j = 1, ..., N_b) \in \mathbb{R} \text{ and all } \underline{u}^e \in \mathbb{R}^{N_n}. \end{array}} \tag{3.22}$$

We explain now, how we compute $\mathcal{J}(\Phi_1^m, \Phi_2^m, ..., \Phi_{N_b}^m, \underline{u}^e)$ and how we find the minimum of this functional.

3.4.1 Computation of $\mathcal{J}$

The first term of (2.17): $\frac{1}{2}\int_{\Omega^e} \sigma^e \|\underline{grad}\, u^e\|^2 d\tau$, using (3.2), is approached by:

$$\frac{1}{2}\sum_{\tau \in \mathcal{T}^e} \int_\tau \sigma^e \ < \underline{grad}\, \underline{u}^e \,|\, \underline{grad}\, \underline{u}^e > d\tau = \frac{1}{2} < \mathbf{A}\underline{u}^e | \underline{u}^e > \tag{3.23}$$

where $\mathbf{A}$ represents the over-all stiffness matrix.

To compute terms of the form

$$\int_{\Gamma} \psi(\Phi^m - u^e) dS$$

similarly as in (3.7), for one node $q \in \Gamma_j^m$, its contribution to the integral is approached by:

$$\psi(\Phi^m - \underline{u}^e(q))\mu(q) \tag{3.24}$$

Γ is a boundary electrode-electrolyte and can be either of the type Γ_j^m or $\Gamma^i(V_i)$.
The sum of those terms for one given electrode is:

$$\mathcal{C} = \sum_{q \in \Gamma} \psi(\Phi^m - \underline{u}^e(q))\mu(q) \tag{3.25}$$

that gives finally an expression of $\mathcal{J}(\Phi_1^m, \Phi_2^m, ..., \Phi_{N_b}^m, \underline{u}^e)$:

$$\boxed{\mathcal{J}(\Phi_1^m, \Phi_2^m, ..., \Phi_{N_b}^m, \underline{u}^e) = \frac{1}{2} < \mathbf{A}\underline{u}^e | \underline{u}^e > + \sum_{k=1}^{N_b+N_f} \mathcal{C}_k} \tag{3.26}$$

We obtain then a numerical expression of the functional $\mathcal{J}$ that depends on the potential of the bipolar electrodes : $\Phi_1^m, \Phi_2^m, ..., \Phi_{N_b}^m$ and on the potential vector in the electrolyte $\underline{u}^e$. The computation sequences of $\mathcal{J}$ are the following:

1. We impose $\Phi_1^m, \Phi_2^m, ..., \Phi_{N_b}^m$. We transform then that problem to a known problem where the potential of each electrode is known.

2. We solve the system (3.11) which gives $\underline{u}^e$

$$\mathbf{A}\,\underline{u}^e + \underline{\mathbf{B}}(\underline{u}^e) = 0$$

3. Having $\underline{u}^e$, we compute

$$\frac{1}{2} < \mathbf{A}\underline{u}^e | \underline{u}^e > + \sum_{k=1}^{N_b+N_f} \mathcal{C}_k$$

3.4.2 Minimization of $\mathcal{J}$

To find the minimum of the functional $\mathcal{J}(\Phi_1^m, \Phi_2^m, ..., \Phi_{N_b}^m, \underline{u}^e)$, the method we used is a general method of descent [J.L71] that we describe below.

$\underline{\Phi}_k^m = \begin{pmatrix} \Phi_{1_k}^m \\ \cdot \\ \cdot \\ \Phi_{N_{b_k}}^m \end{pmatrix}$ is the vector containing the imposed potentials of each bipolar electrode at the step k.

It consists of building a sequence $\underline{\Phi}_k^m$ such that

$$\mathcal{J}(\underline{\Phi}_{k+1}^m, \underline{u}^e) < \mathcal{J}(\underline{\Phi}_k^m, \underline{u}^e) \qquad \forall k. \tag{3.27}$$

We note :

$$\underline{\Phi}_{k+1}^m = \underline{\Phi}_k^m - \rho_k \underline{\omega}_k, \qquad \|\underline{\omega}_k\| = 1, \qquad \rho_k > 0 \tag{3.28}$$

The choice of $\underline{\omega_k}$ and ρ_k is given by [J.L71]:

$$\underline{\omega}_k = \frac{\underline{v_k}}{\|\underline{v_k}\|} \qquad \underline{v_k} = \begin{pmatrix} \partial_{\Phi_{1_k}^m} \mathcal{J} \\ \cdot \\ \cdot \\ \partial_{\Phi_{N_{b_k}}^m} \mathcal{J} \end{pmatrix} \tag{3.29}$$

In order to simplify the notations, we note :

$$\mathcal{J}_0 = \mathcal{J}(\underline{\Phi}_0^m, \underline{u}^e)$$

So,

$$\mathcal{J}_h = \mathcal{J}(\underline{\Phi}_h^m, \underline{u}^e) = \mathcal{J}(\underline{\Phi}_0^m - h\underline{\omega}_0, \underline{u}^e)$$

Then the choice of ρ is described in the following algorithm (Figure 3.11).

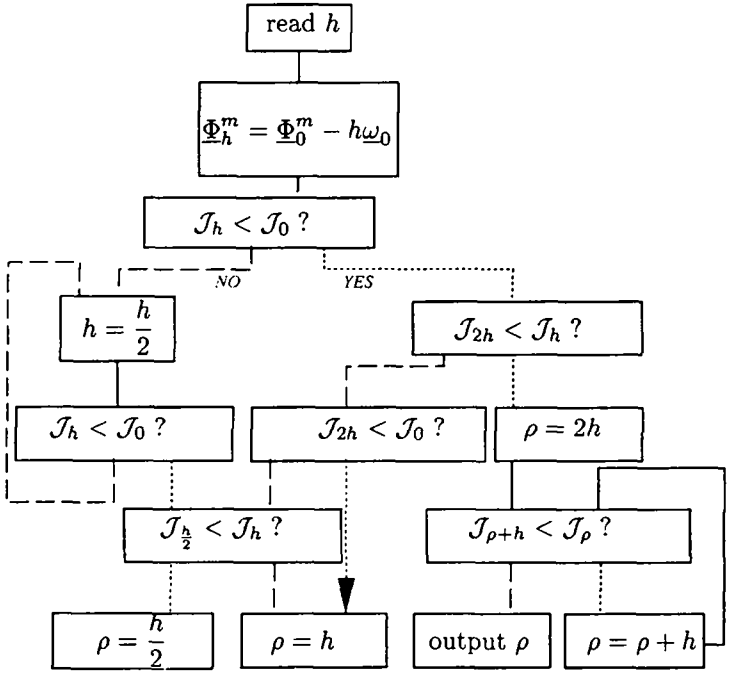

Figure 3.11: Algorithm of minimization of $\mathcal{J}$

3.5 Prismatic finite element

For three-dimensional geometries made of stacking of layers, we have developed a finite element which takes into account these particular geometries. For such cases, the two-dimensional mesh is made using the SIMAIL package and the nodes and elements are renumbered in order to optimize the storage. The finite element we have chosen is obtained by elevating a triangle. Each prism (pentahedra) built has a constant height h as shown in Figure 3.12. We model electrochemical cells which have such geometries and computations results are shown in § 5.5.

3.5.1 Domain approximation

The restriction of an approached function $\tilde{u}$ to the prism is the linear interpolation between its values on the two triangles T and T'.

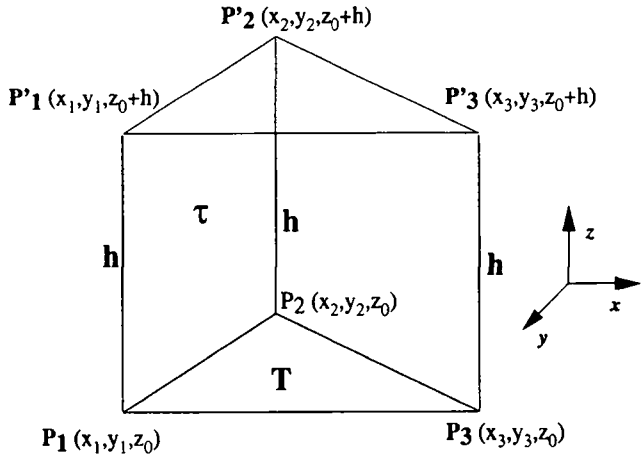

Figure 3.12: Prismatic finite element with a triangular base

$\tilde{u}$ is built using a linear interpolation on the z axis et we have:

$$\tilde{u}(x,y,z) = u(x,y) + \frac{z - z_0}{h}\left(u'(x,y) - u(x,y)\right) \tag{3.30}$$

where $u(x,y)$ is defined on the inferior plane $(z = z_0)$
and $u'(x,y)$ is defined on the superior plane $(z = z_0 + h)$ of the prism of height h.

On each triangle T, T' the functions $u(x,y)$ and $u'(x,y)$ are approached by ordinary finite element, linear affine.
Thus, a function $\tilde{u}$ is determined on a prism by its 6 values at the 6 vertices of the prism.
Using this finite element, we compute the different terms of the PROBLEM 2B (2.16).

3.5.2 Elementary stiffness matrix

Integral of the form $\int_\tau \sigma^e < \underline{grad}\,\tilde{u} | \underline{grad}\,\tilde{v} > d\tau$
have to be approached.
The calculation is now described:

Remark: $\tilde{u} = \tilde{u}(x,y,z)$ but $u = u(x,y)$.
Taking the gradient of $\tilde{u}$ (3.30), we obtain:

$$\begin{aligned}
\underline{grad}\,\tilde{u} &= \begin{pmatrix} \underline{grad}\,u \\ 0 \end{pmatrix} + \begin{pmatrix} \frac{z - z_0}{h}\,\underline{grad}(u' - u) \\ \frac{1}{h}\,(u' - u) \end{pmatrix} \\
&= \begin{pmatrix} \frac{h - z + z_0}{h}\,\underline{grad}(u) + \frac{z - z_0}{h}\,\underline{grad}(u') \\ \frac{1}{h}(u' - u) \end{pmatrix} \\
&= \begin{pmatrix} A(z)\,\underline{grad}\,u + B(z)\,\underline{grad}\,u' \\ \frac{1}{h}\,(u' - u) \end{pmatrix}
\end{aligned}$$

with $A(z) = \dfrac{h - z + z_0}{h}$ and $B(z) = \dfrac{z - z_0}{h}$

Similarly,

$$\underline{grad}\,\tilde{v} = \begin{pmatrix} A(z)\,\underline{grad}\,v + B(z)\,\underline{grad}\,v' \\ \frac{1}{h}\,(v' - v) \end{pmatrix}$$

Then

$$\begin{aligned} < \underline{grad}\,\tilde{u} | \underline{grad}\,\tilde{v} > \; &= A^2(z) \; < \underline{grad}\,u | \underline{grad}\,v > \\ &+ A(z)B(z) \; < \underline{grad}\,u' | \underline{grad}\,v > \\ &+ B^2(z) \; < \underline{grad}\,u' | \underline{grad}\,v' > \\ &+ \frac{1}{h^2}\,(u'-u)(v'-v) \end{aligned}$$

Now, on the prism τ, we evaluate:

$$\int_\tau \sigma^e \; < \underline{grad}\,\tilde{u} | \underline{grad}\,\tilde{v} > \, d\tau = \int_T \left[\int_{z_0}^{z_0+h} \sigma^e \; < \underline{grad}\,\tilde{u} | \underline{grad}\,\tilde{v} > \, dz \right] ds$$

We suppose that on τ, σ^e is independent of z, then $\sigma^e = \sigma^e(x,y)$ and:

$$\begin{aligned} &\int_\tau \sigma^e \; < \underline{grad}\,\tilde{u} | \underline{grad}\,\tilde{v} > \, d\tau = \int_T \sigma^e \left[< \underline{grad}\,u | \underline{grad}\,v > \int_{z_0}^{z_0+h} A^2(z) dz \right. \\ &+ (\sigma^e \; < \underline{grad}, u' | \underline{grad}\,v > + \sigma^e \; < \underline{grad}\,u | \underline{grad}\,v' >) \int_{z_0}^{z_0+h} A(z)B(z) dz \\ &\left. + \sigma^e \; < \underline{grad}\,u' | \underline{grad}\,v' > \int_{z_0}^{z_0+h} B^2(z) dz \right] \end{aligned}$$

The calculations of the integrals of $A^2(z)$, $A(z)B(z)$ and $B^2(z)$ give:

$$\begin{aligned} \int_{z_0}^{z_0+h} A^2(z)\,dz \quad &= \int_{z_0}^{z_0+h} \frac{1}{h^2}\,(-z+z_0+h)^2\,dz \quad &= \frac{h}{3} \\ \int_{z_0}^{z_0+h} A(z)B(z)\,dz \quad &= \int_{z_0}^{z_0+h} \frac{1}{h^2}\,(z-z_0)(-z+z_0+h)\,dz \quad &= \frac{h}{6} \\ \int_{z_0}^{z_0+h} B^2(z)\,dz \quad &= \int_{z_0}^{z_0+h} \frac{1}{h^2}\,(z-z_0)^2\,dz \quad &= \frac{h}{3} \end{aligned}$$

Thus,

$$\begin{aligned} &\int_\tau \sigma^e \; < \underline{grad}\,\tilde{u} | \underline{grad}\,\tilde{v} > \; d\tau = \int_T \sigma^e \left[\frac{h}{3} \; < \underline{grad}\,u | \underline{grad}\,v > \right. \\ &+ \frac{h}{6} \; < \underline{grad}\,u' | \underline{grad}\,v > + \frac{h}{6} \; < \underline{grad}\,u | \underline{grad}\,v' > \\ &\left. + \frac{h}{3} \; < \underline{grad}\,u' | \underline{grad}\,v' > \right] ds + \int_T \frac{\sigma^e}{h^2} (u'-u)\,v' ds - \int_T \frac{\sigma^e}{h^2} (u'-u)\,v ds \end{aligned}$$

Our approximation of functions f on an element τ is given by its values at the 6 nodes that we note:

$\underline{f} = \begin{pmatrix} f_1 \\ f_2 \\ f_3 \end{pmatrix}$: values at the 3 nodes P_1, P_2, P_3 and

$\underline{f'} = \begin{pmatrix} f'_1 \\ f'_2 \\ f'_3 \end{pmatrix}$: values at the 3 nodes P'_1, P'_2, P'_3

From [Fro], on a triangle, we have:

$$\int_T f\, v\, ds = \frac{|D_{xy}|}{24} (f1, f2, f3) \underbrace{\begin{pmatrix} 2 & 1 & 1 \\ 1 & 2 & 1 \\ 1 & 1 & 2 \end{pmatrix}}_{\mathcal{F}} \begin{pmatrix} v_1 \\ v_2 \\ v_3 \end{pmatrix} \qquad (3.31)$$

with $\mathcal{F} = \begin{pmatrix} 2 & 1 & 1 \\ 1 & 2 & 1 \\ 1 & 1 & 2 \end{pmatrix}$, which gives, supposing σ^e constant on T:

$$\frac{\sigma^e}{h^2} \int_T (u' - u)\, v'\, ds - \frac{\sigma^e}{h^2} \int_T (u' - u)\, v\, ds =$$

$$\frac{\sigma^e\, |D_{xy}|}{24\, h} \left[(u'_1 - u_1, u'_2 - u_2, u'_3 - u_3)\, \mathcal{F} \begin{pmatrix} v'_1 \\ v'_2 \\ v'_3 \end{pmatrix} \right.$$

$$\left. - (u'_1 - u_1, u'_2 - u_2, u'_3 - u_3)\, \mathcal{F} \begin{pmatrix} v_1 \\ v_2 \\ v_3 \end{pmatrix} \right]$$

with: $|D_{xy}| = 2\,\text{Area}(T) = \begin{vmatrix} x_1 & x_2 & x_3 \\ y_1 & y_2 & y_3 \\ 1 & 1 & 1 \end{vmatrix}$

From [Fro], we have also:

$$\int_T \sigma^e \; < \underline{grad}\, u | \underline{grad}\, v > \; ds \; = \; \frac{\sigma^e}{2\,|D_{xy}|}\,(u_1,u_2,u_3)\,\mathcal{M}\begin{pmatrix} v_1 \\ v_2 \\ v_3 \end{pmatrix}$$

$$\text{with } \mathcal{M} \; = \begin{pmatrix} y_{32}^2 + x_{32}^2 & y_{32}y_{13} + x_{32}x_{13} & y_{32}y_{21} + x_{32}x_{21} \\ y_{13}y_{32} + x_{13}x_{32} & y_{13}^2 + x_{13}^2 & y_{13}y_{21} + x_{13}x_{21} \\ y_{21}y_{32} + x_{21}x_{32} & y_{21}y_{13} + x_{21}x_{13} & y_{21}^2 + x_{21}^2 \end{pmatrix}$$

with $x_{ij} = x_i - x_j,\; y_{ij} = y_i - y_j$

Finally:

$$\int_\tau \sigma^e \; < \underline{grad}\, \tilde{u} | \underline{grad}\, \tilde{v} > \; d\tau \; \approx$$

$$\frac{\sigma^e\, h}{12\,|D_{xy}|}\left[2\,(u_1,u_2,u_3)\,\mathcal{M}^t\begin{pmatrix} v_1 \\ v_2 \\ v_3 \end{pmatrix} + (u_1',u_2',u_3')\,\mathcal{M}^t\begin{pmatrix} v_1 \\ v_2 \\ v_3 \end{pmatrix}\right.$$
$$\left. + 2\,(u_1',u_2',u_3')\,\mathcal{M}^t\begin{pmatrix} v_1' \\ v_2' \\ v_3' \end{pmatrix} + (u_1,u_2,u_3)\,\mathcal{M}^t\begin{pmatrix} v_1' \\ v_2' \\ v_3' \end{pmatrix}\right]$$
$$+ \frac{\sigma^e\,|D_{xy}|}{24\,h}\left[(u_1'-u_1,u_2'-u_2,u_3'-u_3)\,\mathcal{F}\begin{pmatrix} v_1' \\ v_2' \\ v_3' \end{pmatrix}\right.$$
$$\left. - (u_1'-u_1,u_2'-u_2,u_3'-u_3)\,\mathcal{F}\begin{pmatrix} v_1 \\ v_2 \\ v_3 \end{pmatrix}\right]$$

that we can rewrite:

$$\int_\tau \sigma^e < \underline{grad}\,\tilde{u} | \underline{grad}\,\tilde{v} > d\tau \approx$$

$$\frac{\sigma^e h}{12\,|D_{xy}|} \left[(u_1, u_2, u_3, u'_1, u'_2, u'_3) \begin{pmatrix} 2\mathcal{M} & \mathcal{M}^t \\ \mathcal{M}^t & 2\mathcal{M} \end{pmatrix} \begin{pmatrix} v_1 \\ v_2 \\ v_3 \\ v'_1 \\ v'_2 \\ v'_3 \end{pmatrix} \right] +$$

$$+ \frac{\sigma^e\,|D_{xy}|}{24\,h} \left[(u_1, u_2, u_3, u'_1, u'_2, u'_3) \begin{pmatrix} \mathcal{F} & -\mathcal{F} \\ -\mathcal{F} & \mathcal{F} \end{pmatrix} \begin{pmatrix} v_1 \\ v_2 \\ v_3 \\ v'_1 \\ v'_2 \\ v'_3 \end{pmatrix} \right]$$

Under a vector form:

$$\int_\tau \sigma^e < \underline{grad}\,\tilde{u} | \underline{grad}\,\tilde{v} > d\tau \approx$$

$$\frac{\sigma^e\,|D_{xy}|}{24\,h} (\underline{u}^t, \underline{u'}^t) \begin{pmatrix} \mathcal{F} & -\mathcal{F} \\ -\mathcal{F} & \mathcal{F} \end{pmatrix} \begin{pmatrix} \underline{v} \\ \underline{v'} \end{pmatrix}$$
$$+ \frac{\sigma^e h}{12\,|D_{xy}|} (\underline{u}^t, \underline{u'}^t) \begin{pmatrix} 2\mathcal{M} & \mathcal{M} \\ \mathcal{M} & 2\mathcal{M} \end{pmatrix} \begin{pmatrix} \underline{v} \\ \underline{v'} \end{pmatrix}$$

Then this integral can be approached by:

$$< \mathbf{a}_{el}\,\tilde{\underline{u}}\,|\,\tilde{\underline{v}} >$$

with $\mathbf{a}_{el}$ (6×6), the stiffness elementary matrix.

$$\mathbf{a}_{el} = \frac{\sigma^e\,|D_{xy}|}{24\,h} \begin{pmatrix} \mathcal{F} & -\mathcal{F} \\ -\mathcal{F} & \mathcal{F} \end{pmatrix} + \frac{\sigma^e h}{12\,|D_{xy}|} \begin{pmatrix} 2\mathcal{M} & \mathcal{M} \\ \mathcal{M} & 2\mathcal{M} \end{pmatrix} \tag{3.32}$$

3.5.3 Interfacial terms

In this particular case, boundary conditions are applied on triangular faces of the prisms. Then the evaluation of interfacial terms is made as exactly the same as in § 3.2.3.

From here, the assembly procedure remains the same as § 3.2.4 and we obtain also the same nonlinear system of equations (3.11) to solve. The major difference here is the storage of the over-all stiffness matrix. We describe in the following sections how the storage and the numbering of the nodes and the elements is done and afterwards the method of numerical solving the linear system using an iterative method is explained.

3.5.4 Construction of the over-all stiffness matrix

Strategy of numbering the mesh

The main advantage of this method is the very small memory occupation for the storage of matrices. The method described here allows us to store a $N \times N$ matrix with only 11 vectors of N components. We detail in the following how we numbered the mesh in Figure 3.13.

For a node i,
we search all the elements (triangle of the layer k) having the node i in common
There are 6 elements : $T_1, T_2, T_3, T_4, T_5, T_6$
This corresponds to 6 faces of prisms to the superior layer $k+1$ and 6 faces of prisms to the inferior layer $k-1$.
We note :

n the number of nodes per line
N the number of nodes per layer,
$Nelem$ the number of elements of the 2D mesh,
NTN the total number of nodes (number of layers x N),
NTE the total number of elements (number of slices x $Nelem$).

Let :
τ_1 the prism which has T_1 as the superior horizontal face
τ_1' the prism which has T_1 as the inferior horizontal face
The nodes of this prism are:
$\tau_1 : (i+n-N, i+1-N, i-N, i+n, i+1, i)$
$\tau_1' : (i+n, i+1, i, i+n+N, i+1+N, i+N)$

Then, we build τ_i and τ_i' for $i = 1$ to 6.

Storage of the over-all stiffness matrix

The over-all stiffness matrix $\mathbf{A}$ is of size $NTN \times NTN$. This sparse matrix, due to the numbering is stored as following (Figure 3.14).

For each element τ from 1 to NTE
for $i = 1, 6$
for $j = 1, 6$
we find the node having the number corresponding to i, we note N_i,
we find the node having the number corresponding to j, we note N_j,
at the position (N_i, N_j) of $\mathbf{A}$, we sum the contribution of $a_{el}(i, j)$

The numbering of the nodes such as Figure 3.14 give then a symmetric matrix which has 21 diagonal vectors of (maximal) length NTN. As $\mathbf{A}$ is symmetric, we store only 11 vectors of the upper triangle.

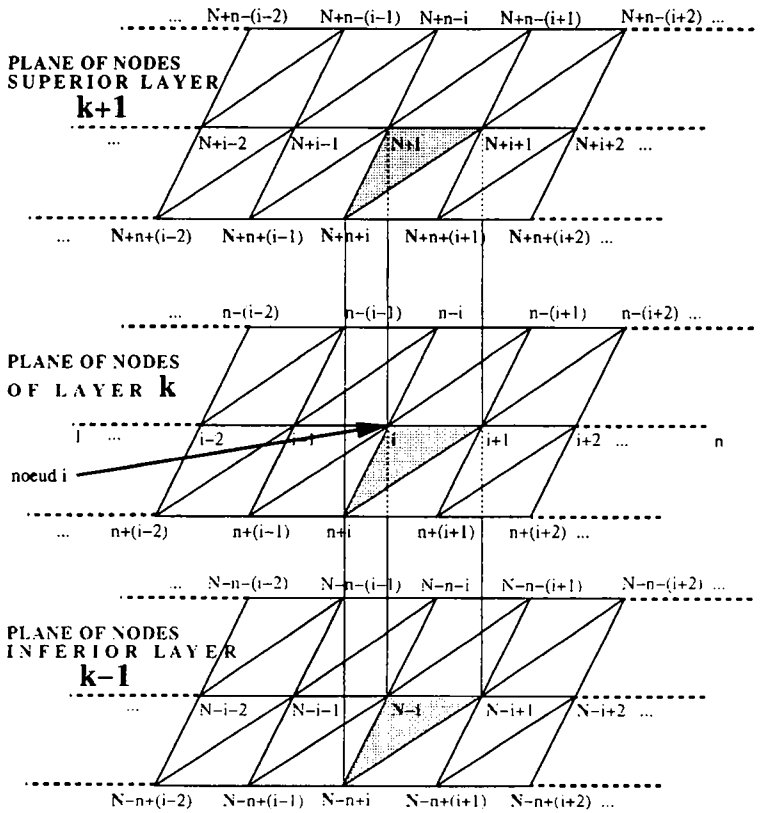

Figure 3.13: Construction and numbering the mesh

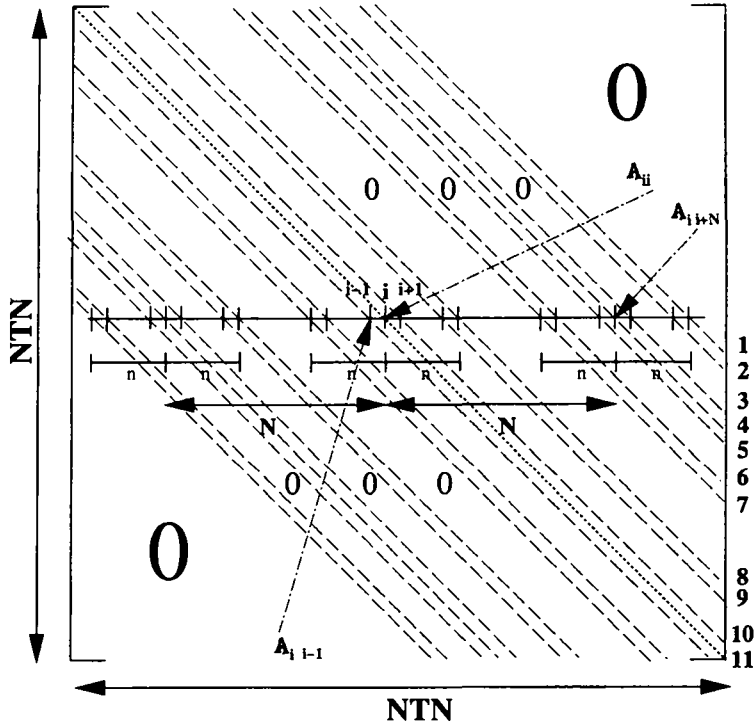

Figure 3.14: Structure of the matrix **A**

These vectors correspond to:

1 :	$\mathbf{A}_{i,i+N+n}$	2 :	$\mathbf{A}_{i,i+N+n+i}$	3	$\mathbf{A}_{i,i+N+1}$
4 :	$\mathbf{A}_{i,i+N+1}$	5 :	$\mathbf{A}_{i,i+N-1}$	6 :	$\mathbf{A}_{i,i+N-n+1}$
7 :	$\mathbf{A}_{i,i+N-n}$	8 :	$\mathbf{A}_{i,i+n}$	9 :	$\mathbf{A}_{i,i+n-1}$
10 :	$\mathbf{A}_{i,i+1}$	11 :	$\mathbf{A}_{i,i}$ (diagonal terms)		

Numerical solving of the linear system

To solve linear systems of equations, we employed a conjugate gradient method [Bar93]. This powerful method allows us here to solve a linear system $A\underline{x} = \underline{b}$ iteratively by a method of descent.
At each iteration, we determine a vector $\underline{p}_k$ and a scalar α_k.
And we can calculate :
$\underline{x}_{k+1} = \underline{x}_k + \alpha_k \underline{p}_k$
with the objective of minimizing a functional.
$\underline{r} = A\underline{x} - \underline{b}$ is the residue of the system $A\underline{x} = \underline{b}$.
We initialize the variables in choosing $\underline{x}_0$ et $\underline{p}_0 = \underline{r}_0$

$$\begin{cases} \underline{x}_0 \\ \underline{p}_0 = \underline{r}_0 = \underline{p} - A\underline{x}_0 \end{cases}$$

For $k = 0, 1....$

$$\begin{cases} \alpha_k = \dfrac{\|\underline{r}_k\|^2}{< A\underline{p}_k \mid \underline{p}_k >} \\ \underline{x}_{k+1} = \underline{x}_k + \alpha_k \underline{p}_k \\ \underline{r}_{k+1} = \underline{r}_k - \alpha_k A\underline{p}_k \\ \beta_{k+1} = \dfrac{\|\underline{r}_{k+1}\|^2}{\|\underline{r}_k\|^2} \\ \underline{p}_{k+1} = \underline{r}_{k+1} \beta_{k+1} \underline{p}_k \end{cases}$$

The test to stop iterations is made on $\|\underline{r}_k\|$. If $\|A\underline{x} - \underline{b}\|$ is lower than a fixed tolerance , we store the result at this iteration.

Chapter 4

The Finite Element Software

4.1 General organization

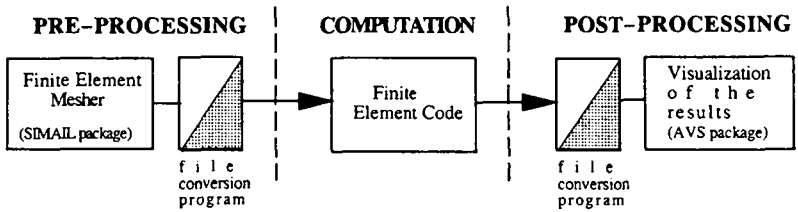

Figure 4.1: Software organization

The Finite Element code built is able to compute primary and secondary potential and current distribution. It is a part a full package that we have divided into three parts. The two other parts consist of commercial software: SIMAIL [SIM] is a Finite Element mesh generator and AVS (Advanced Visual Systems) [AVS] is a complex visualizing tool we use for graphical representations of computations. That version runs on Silicon Graphics workstations (UNIX) and the finite element code has been written in Fortran. Conversion routines from the output of the mesh generator to the code are written in C++ and conversion routines from the code to the post-processing are written in FORTRAN.

We describe in this chapter the programming and numerical aspects: data organization, format of the data structures and algorithms of numerical solving.

Finally, because we use iterative methods for large systems solving, the influence of each parameter of methods that we employ have been studied to validate and optimize the code.

4.2 Data pre-processing

To generate a mesh, following methods of [Geo91] and using the SIMAIL package, we obtain at the end a binary file. To extract the mesh information, we wrote the file conversion routine which gives us a mesh structure in ASCII having the following structure for both two and three-dimensional geometries:

title of the mesh
dimension, number of nodes, number of elements, number of faces
for i=1...number of nodes:
    node i, reference, x_i, y_i, *(*z_i*, if 3D)*
    element j, number of nodes of the element, domain,
for j=1...number of elements:
    1st node, 2nd node, 3rd node, (4th node, if 3D)
for k=1...number of faces:
    face k, number of nodes of the face, reference,
    1st node, 2nd node, (3rd node,if 3D the face is a triangle)

reference is the code (integer) we attribute to a node which has a boundary condition, we have adopted the following convention: if the reference is lower than 10, the corresponding value of the potential is fixed and **known**.
If the reference is greater than 11, the corresponding value of the potential is fixed and **unknown**. Both references correspond to an interfacial condition (extended *Butler-Volmer* function).

If there is no boundary condition, then the reference is null.
For a two-dimensional element (triangle), if two nodes have the same non-null reference, then a referenced face (segment) is created in the file as showed above. For a three-dimensional element (tetrahedra), three nodes have the same non-null reference, then a referenced face (triangle) is created in the file as shown above.
domain is the code (integer) we attribute to an element to specify its electrical conductivity.

4.3 The Finite Element code

4.3.1 Computation sequences

Figure 4.2 gives the organization of the computation sequences which have been implemented.

Each block from 1 to 5 is now described below:

Block 1

This is the part which reads the mesh information (from the preceding paragraph), and initializes the program with the following data:

1. DIM: space dimension (2 or 3),
2. N_n: number of nodes,
3. N_t: number of elements,
4. N_s: number of sides,
5. N_f: number of fed electrodes ($reference \leq 10$) at a fixed known potential,
6. N_b: number of bipolar electrodes ($reference \geq 11$) at a floating unknown potential.

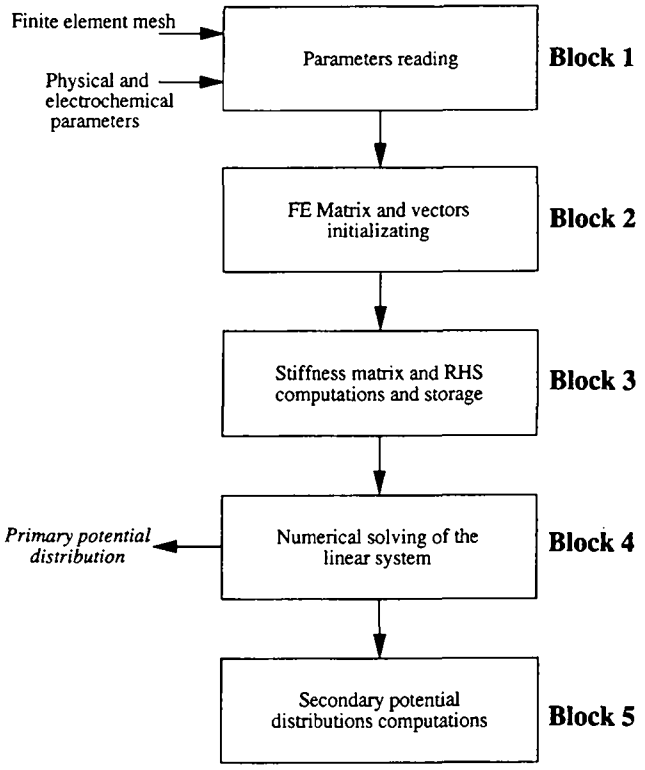

Figure 4.2: Computation sequences

Physical and electrochemical parameters are now introduced:

Input data of the program

1. potential of each electrode, **vector of N_f real numbers**,
2. conductivity of the electrolyte, **a real function of x, y, z or of the domain number from the mesh data**,
3. sampled generalized *Butler-Volmer* current-potential function φ given in a file of the type (x, y),

4. "*Kellogg*" parameter ($\lambda > 0$, see § 3.3)

5. ϵ_{kellog} is the relative error tolerance for the non-linear system solving

6. ϵ_{min} is the relative error tolerance for the minimization process.

Block 2

From the size information obtained previously, that block initializes and allocate dynamic memory for the storage of the stiffness matrix, solution vector and all other auxiliary vectors needed for the calculations.

The storage method chosen for the stiffness matrix is skyline coded [LT93]. This block also computes the length of vectors for the storage of the stiffness matrix under that form.

Block 3

This module computes elementary stiffness matrices, makes the assembly and stores the values of the over-all stiffness matrix in a vector of real numbers of double precision.

Block 4

This module computes first an LU factorization of the stiffness matrix [LT93] and stores it in a vector that will be used a large number of times further. To solve the linear system (linear part of (3.11)) which gives the potential in each node, we use a penalty method of the boundary conditions. Then, a Gauss method [LT93] is employed now to find the unknown vector of potentials. Finally, this is the **primary solution** that has been calculated and stored.

Block 5

This is the "heart" of our problem and we totally dedicate the next section to that part.

4.3.2 Programming the non-linear part

In function of the number of the bipolar electrodes in the cell, three different data flow charts are presented. Algorithms that have been have programmed are detailed in each data flow chart:

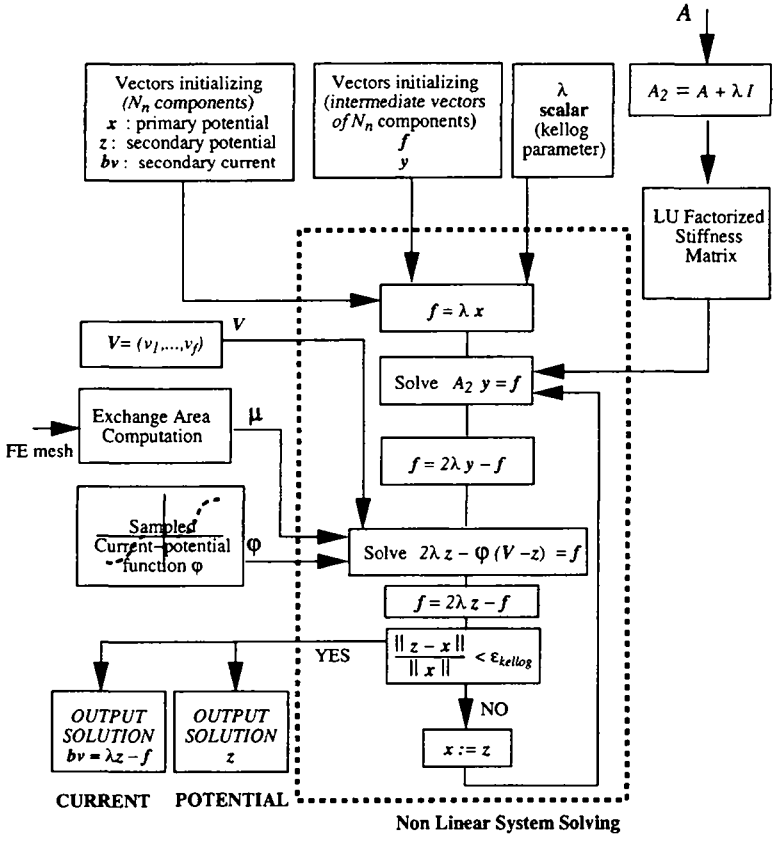

Figure 4.3: Computation sequences : no bipolar electrode

1. **No bipolar electrode**

In this case, the system is strictly composed of N_f electrodes at a fixed known potential with the extended *Butler-Volmer* function φ at interfaces electrodes-electrolyte.
Then the numerical solving of the non-linear system Eq. (3.11) using the method of *Kellogg* as it has been described in § 3.3 is shown in Figure 4.3.
The primary solution vector $\mathbf{x}$ is obtained from the block 4, and the stiffness matrix from the block 3.
The exchange area computation is made from the faces information extracted from the mesh data and computed as explained in § 3.2.3 in two or three dimensions.
To obtain $\mathbf{A}_2 = \lambda\mathbf{I} + \mathbf{A}$, we add the value of λ in each diagonal term of $\mathbf{A}$. $\mathbf{A}_2$ is LU factorized and the solving of the linear system: $\mathbf{A}_2 y = f$ is rapidly made using a Gauss method.

The solving of the system of the form : $2\lambda z - \varphi(V_i - z) = f$. has been described in § 3.3.2.

2. **One bipolar electrode**

Compared to the system without any bipolar electrode, the difference is the parameter U_{bip} representing the bipolar electrode potential which is unknown. It has a default value as an input data and the code determines its real physical potential by calculating iteratively the term : $I_{tot} = \int_{\Gamma^m} \varphi(U_{bip} - z)ds$ as shown in Figure 4.4. Once the condition $|I_{tot}| < \epsilon_{min}$ is satisfied, the bipolar potential has been adjusted to its physical value.
The term δ_u is fixed relatively to the cell potential (typically 0.001).
The non-linear part of the system is exactly the same as the one described just before.

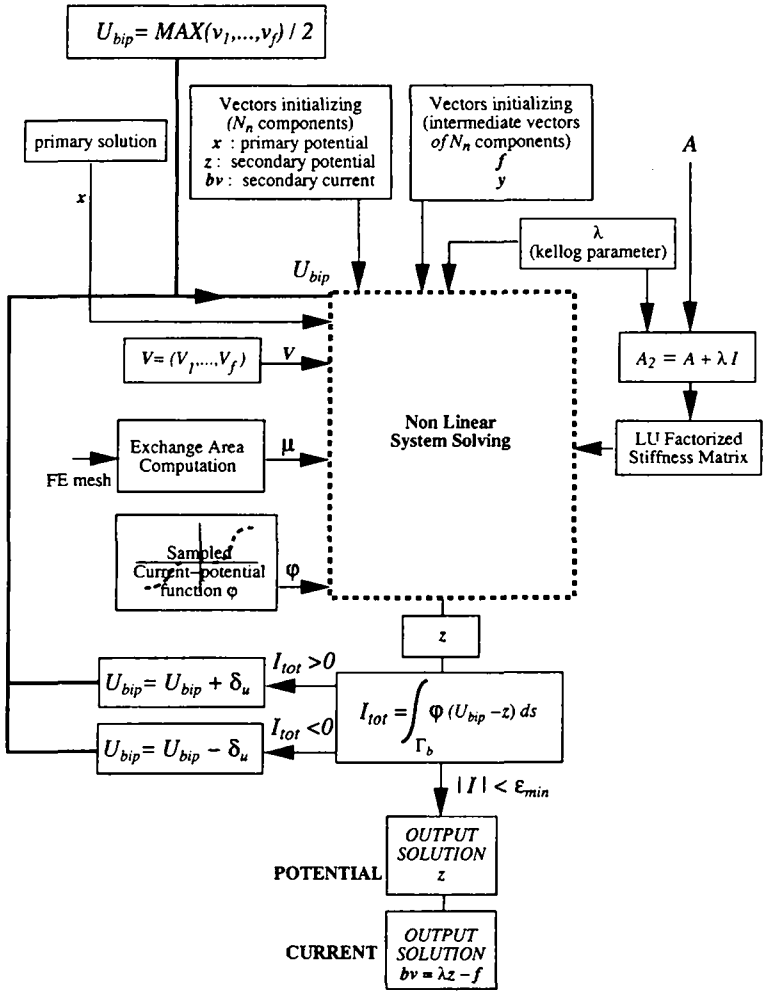

Figure 4.4: Computation sequences : one bipolar electrode

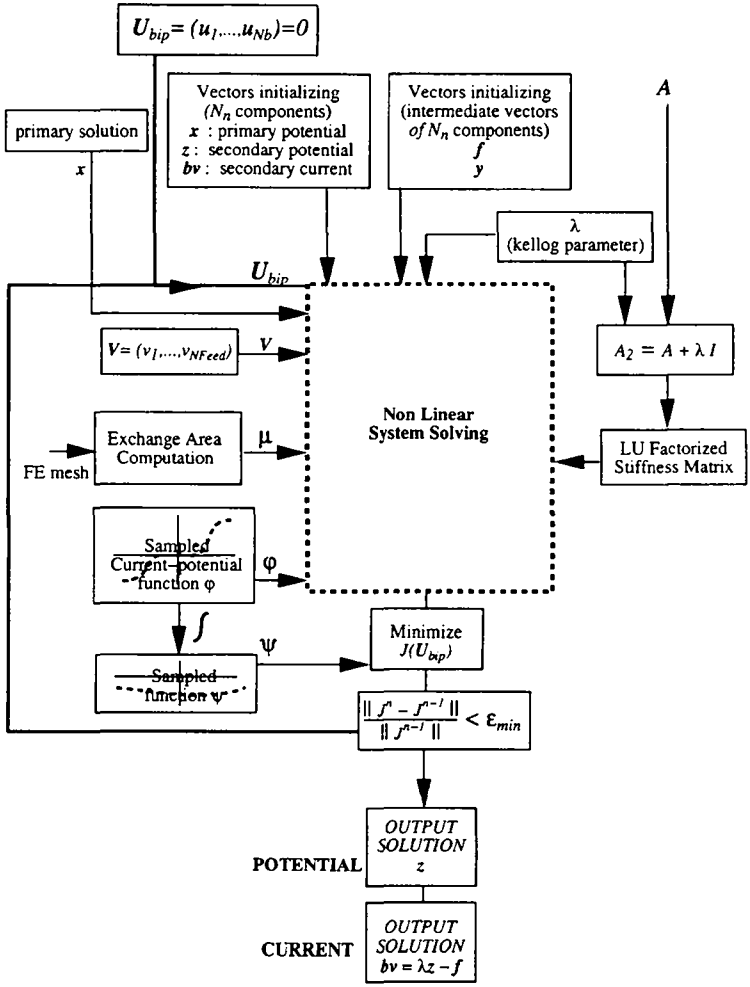

Figure 4.5: Computation sequences : several bipolar electrodes

3. **Several bipolar electrodes**

   Here N_b bipolar electrodes are at unknown potentials. We use then an iterative scheme of minimization of a functional J as described § 3.4.2 instead of the preceding method that checks if the total current crossing the bipolar electrode is near to zero. This is the major difference between Figure 4.4 and Figure 4.5.

4.4 Data post-processing

This part consists of building a new file in a specific format readable by the software AVS [AVS]. It is an interactive tool for scientific visualization. It includes the following subsystems:

1. **Image Viewer** is a high-level tool for manipulating and viewing images.

2. **Graph Viewer** is a high-level tool for graphing data.

3. **Geometry Viewer** allows to compose "scenes" that contain geometrically-defined objects. The objects must have been created by programs or AVS modules that use AVS's GEOM programming library. One can transform the objects themselves (move, rotate, scale); one can change the viewing parameters (e.g. move the eye point, perspective view, etc.); and one can control the way in which the graphical images are rendered (lighting and shading, Z- buffering, etc.).

4. **Network Editor** (Figure 4.6) is a visual programming interface for connecting computational modules together into networks that perform visualization functions. The network we built for our needs is shown in Figure 4.6

From the computations, we obtain the following output:

1. z: vector of N_n components giving the potential of each node of the mesh.

2. bv: vector of N_n components giving the normal component of the current crossing the metal-electrolyte interface.

3. μ: vector of N_n components giving the exchange area (see § 3.2.3)

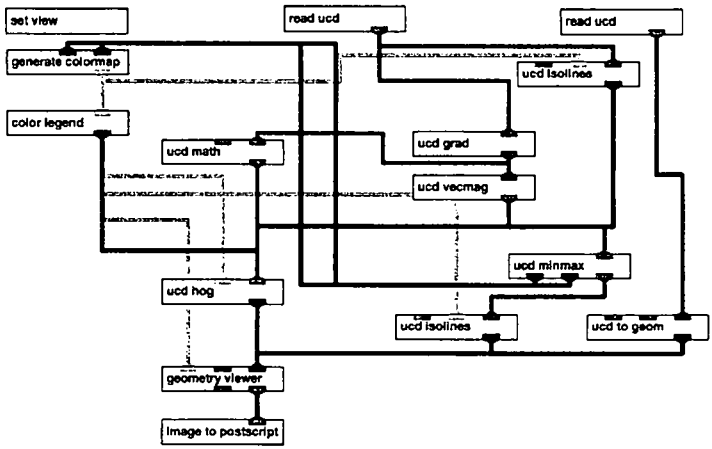

Figure 4.6: AVS network for current and potential distributions visualization

Then, respecting the input format of AVS, we have written a conversion routine which reads the mesh, the results and writes the needed information in a binary file (with the suffix *.inp*).

The module **read ucd** of AVS reads this file and the network displays the following information in 5 fields:

1. For an interfacial node : the potential of the metal, else 0.
2. The potential in the electrolyte.
3. For an interfacial node : the potential jump, else 0.
4. For an interfacial node : the current density, else 0.
5. The current vector (2D or 3D) in the whole system.

It also displays equipotential lines or surfaces. So this tool allows us to investigate the local behavior of electrodes. Computation results are shown in details in chapter 5.

4.5 Software validation

We deal in this section with numerical aspects of the program. Some tests have been made to study the influence of the variation of parameters of the program on the quality (convergence, errors) of the expected solution.

4.5.1 2D tests

Two dimensional tests have been undertaken on a rectangular reactor (Figure 4.7) of $40 \times 16\,\mathrm{mm}^2$ with two current feeders and at each interface electrode-electrolyte, the extended *Butler-Volmer* function is given, it provides from experiments and is displayed in Figure 4.9. It is the behavior of the Ni electrode in 1 N NaOH.
Three regular meshes of different steps have been made (Figure 4.8).

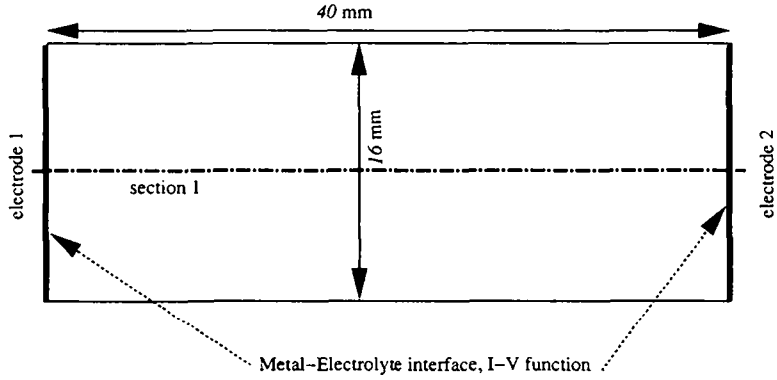

Figure 4.7: Geometry of the reactor

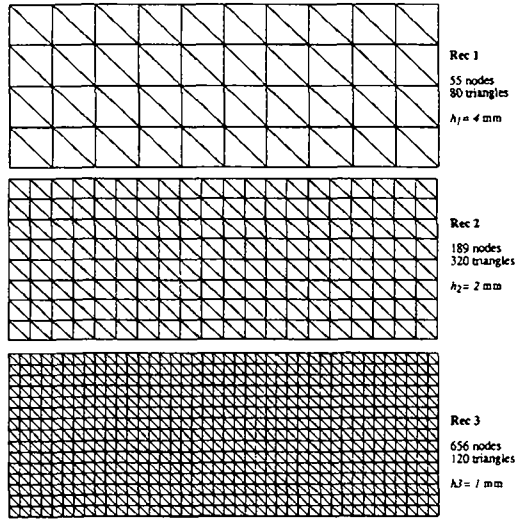

Figure 4.8: Finite element meshes of different steps

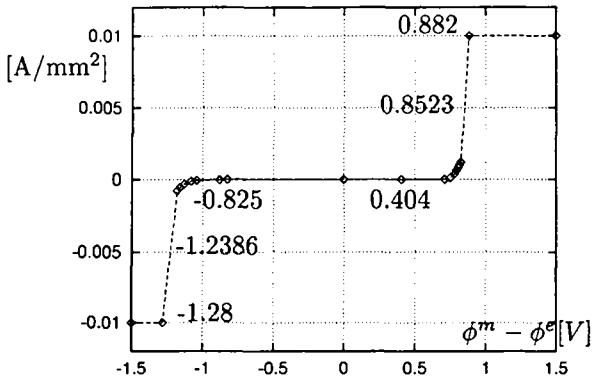

Figure 4.9: Extended *Butler-Volmer* function used

4.5.2 Comparison with an unidimensional calculation

We fix constant the electrolyte conductivity σ^e.

The problem we solve here is unidimensional, and we are able to get the exact solution without computing. In Figure 4.7, we consider the section 1 of the reactor and we proceed in the following manner to test the performances of the software.

We fix a constant value for the current density i according to potential jumps that we find on the curve Figure 4.9.

We fix σ^e. Then we evaluate the potential cell to apply to get the fixed current density in the whole cell. The potential jump at the anode is δ_1, given by Figure 4.9 and the potential jumps at the cathode is δ_2. The ohmic drop δ in the cell is obtained from Ohm's law:

$$\delta = \frac{l}{\sigma^e} i \tag{4.1}$$

And the cell potential is $V = \delta_1 + \delta + \delta_2$.
The following table gives the calculations for current densities fixed to $i = 0.01\,[\text{A.mm}^{-2}]$ and $i = 0.005\,[\text{A.mm}^{-2}]$, for three different values of conductivity σ^e from 1 to $0.01\,[\Omega^{-1}.\text{mm}^{-1}]$

Case	i[A.mm^{-2}]	σ^e	δ_1[V]	δ_2[V]	δ[V]	V[V]
U_1	0.01	1	1.28	0.882	0.4	2.563
U_2	0.005	1	1.2386	0.8523	0.2	2.291
U_3	0.01	0.1	1.28	0.882	4	6.163
U_4	0.005	0.1	1.2386	0.8523	2	4.091
U_5	0.01	0.01	1.28	0.882	40	41.163
U_6	0.005	0.01	1.2386	0.8523	20	22.091

Then simulations have been performed with the applied cell potential U_1 to U_6 for the three meshes (Figure 4.8). The following table gives also the value of λ, the parameter used in the method of *Kellogg* (§ 3.3) and the number of iterations n_{it} needed for a relative error $\epsilon_{kellog} = 10^{-6}$

Mesh	σ^e[Ω^{-1}.mm^{-1}]	V[V]	i[A.mm^{-2}]	λ	n_{it}
Rec 1	1	2.563	0.01	0.1	253
Rec 2	1	2.563	0.01	0.1	295
Rec 3	1	2.563	0.01	0.1	974
Rec 1	1	2.291	0.00527	0.1	256
Rec 2	1	2.291	0.00527	0.1	247
Rec 3	1	2.219	0.00527	0.1	759
Rec 1	0.1	6.163	0.01	0.1	291
Rec 2	0.1	6.163	0.01	0.1	875
Rec 3	0.1	6.163	0.01	0.1	2100
Rec 1	0.1	4.091	0.00504	0.1	111
Rec 2	0.1	4.091	0.00504	0.1	362
Rec 3	0.1	4.091	0.00504	0.1	1157
Rec 1	0.01	42.163	0.01	0.01	304
Rec 2	0.01	42.163	0.01	0.01	916
Rec 3	0.01	42.163	0.01	0.01	2732
Rec 1	0.01	22.091	0.005	0.01	79
Rec 2	0.01	22.091	0.005	0.01	251
Rec 3	0.01	22.091	0.005	0.01	789

Simulations give the expected results for current densities values and potential jumps. They are exactly what the predicted calculations give. In order to optimize computation time, the dependance of the size of the mesh and the potential is given in the following section.

4.6 Parameters study

4.6.1 Reactor without bipolar electrode

Theoretically, it is very difficult to scale-up the parameter λ. But some information can be added: when we employ the method of *Kellogg*, the parameter λ has an influence only on the diagonal terms of the all-over stiffness matrix $\mathbf{A}$ because we calculate $\mathbf{A}_2 = \lambda\mathbf{I} + \mathbf{A}$. Then, as the all-over stiffness matrix depends on the size of the geometry (mesh) and depends on the different conductivities of the electrolyte, λ has the same dependence.

A first study to minimize time computations (i.e number of iterations n_{it}) has been undertaken for these 6 cases (U_1 to U_6) for the three rectangular meshes. We are interested in finding the dependence of that delicate parameter λ in function of the size of the mesh, the cell potential and the conductivity.

In the following, the cases U_1 to U_6 are associated to a cell potential V and a fixed current density i.

Figure 4.10 to Figure 4.12 display the number of iterations in function of λ for a fixed relative error $\epsilon_{kellog} = 10^{-6}$ for the six cases U_1 to U_6.

In all cases, there is a value of λ for which the number of iterations is minimal. It is, of course, of a great interest to predict this parameter in order to minimize the time computations. Some remarks can be made from Figures 4.10, 4.11 , 4.12:

1. The influence of the cell potential for a given mesh has a very weak influence on the value λ. The curves have the same form but the number of iterations increases when the cell potential increases.

2. Changing the size of the grid (Rec 1, Rec 2, Rec 3) show clearly for all cases from U_1 to U_6 that refining the mesh decreases the optimal value of λ.

3. Changing the conductivity of the electrolyte shows clearly for all cases from U_1 to U_6 that reducing the value of the conductivity decreases the optimal value of λ.

Figure 4.13 shows for each optimal value of λ in the case U_1 for the three meshes, the evolution of the relative error (left graph) and the norm of the vector solution (right graph) in function of the number of iterations.

In all these cases, we have supposed σ^e to be constant. Now we are interested to have an idea of the optimal λ when the conductivity has values between 1 and 10^{-2} $[\Omega^{-1}.\text{mm}^{-1}]$.
In Figure 4.14, the left figure represents the variation of the conductivity of the electrolyte in function of the distance, and on the right figure, the number of iterations in function of λ.

The conclusion of this first study is that the estimation of the optimal value λ can be determined by taking a value in the order of magnitude of the lowest conductivity of the electrolyte if the conductivity is lower than approximately $0.1\,[\Omega^{-1}.\text{mm}^{-1}]$. If the minimal conductivity is higher than this value, the optimal λ cannot be greater than 0.1.

This choice confirms previous observations made by J.-Y. Salamin [Sal95] in other cells configurations.

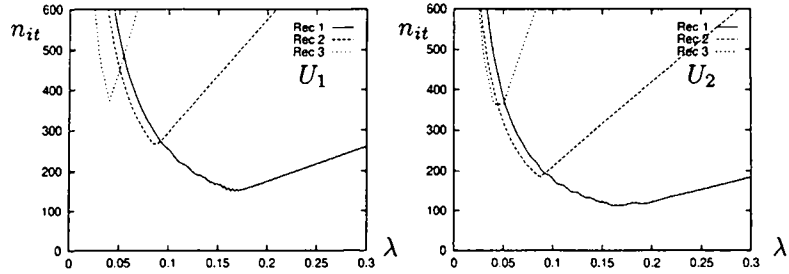

Figure 4.10: $n_{it} = f(\lambda)$, $\sigma^e = 1\,[\Omega^{-1}.\mathrm{mm}^{-1}]$

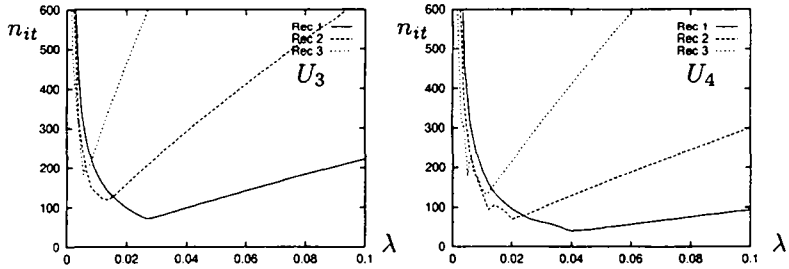

Figure 4.11: $n_{it} = f(\lambda)$, $\sigma^e = 0.1\,[\Omega^{-1}.\mathrm{mm}^{-1}]$

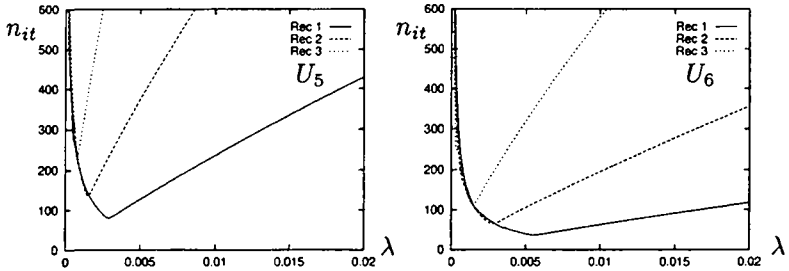

Figure 4.12: $n_{it} = f(\lambda)$, $\sigma^e = 0.01\,[\Omega^{-1}.\mathrm{mm}^{-1}]$

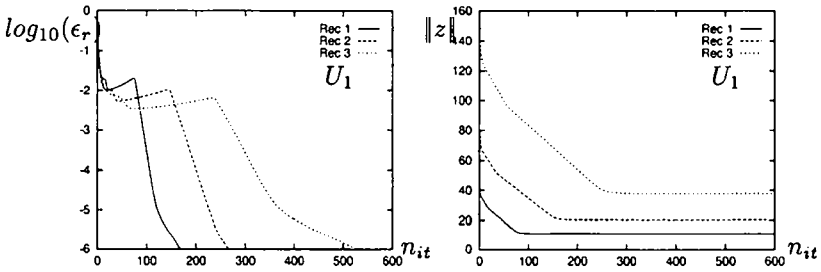

Figure 4.13: Convergence of the norm of the vector solution

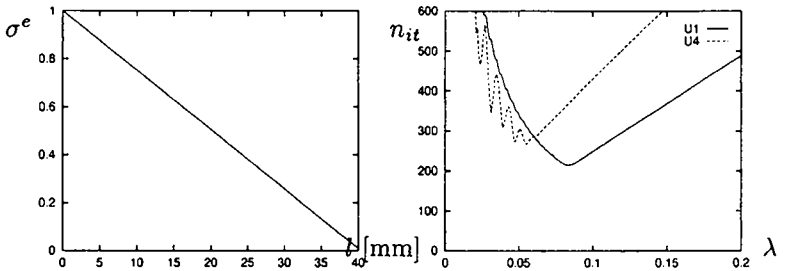

Figure 4.14: $n_{it} = f(\lambda)$ for σ^e variable

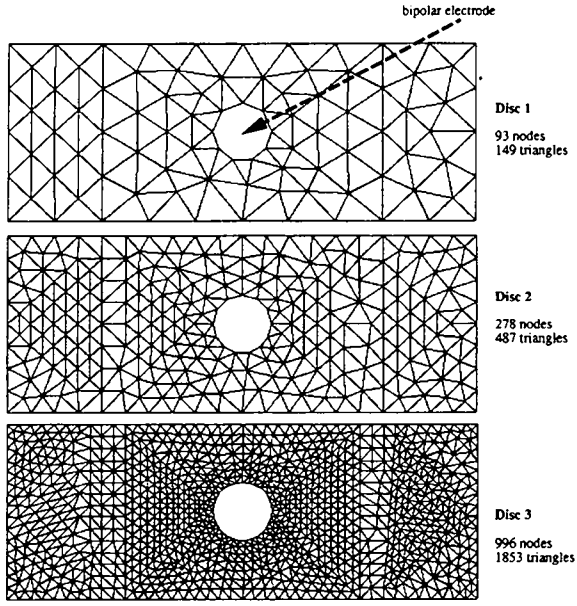

Figure 4.15: Finite element meshes of different steps

4.6.2 Influence of inserting a bipolar electrode

Figure 4.15 shows new meshes $Disc\,1, Disc2$ and $Disc\,3$ which have the same dimensions as $Rec\,1, Rec\,2, Rec\,3$ from Figure 4.8.

Same computations have been made to observe the influence of the bipolar in the case U_1 and compared values for the 3 meshes have been reported in Figure 4.16 and Figure 4.17.

This bipolar electrode has a very weak influence on the systems we studied and the same remarks concerning the estimation of the optimal value of λ as before are available in this case.

4.6.3 3D tests

Figure 4.18 shows the three dimensional meshes of $Rec\,1$, $Rec\,2, Rec\,3$ from Figure 4.8. $Tet\,1, Tet\,2$ and $Tet\,3$ are the elevations of these 2D

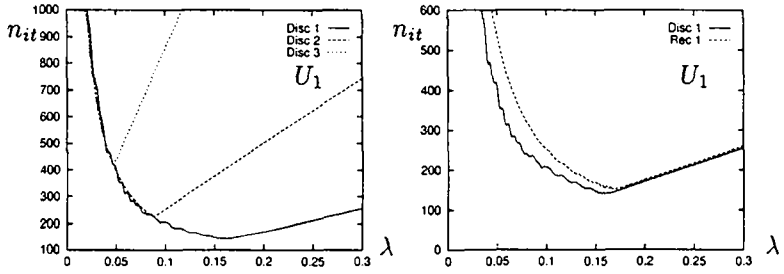

Figure 4.16: $n_{it} = f(\lambda)$

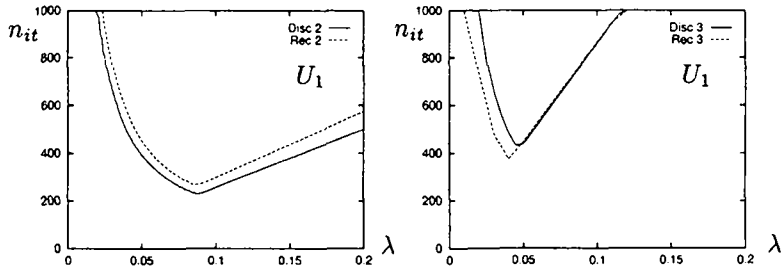

Figure 4.17: $n_{it} = f(\lambda)$

rectangular meshes and we have kept the same step of mesh ($h_1 = 4\,[\text{mm}]$, $h_2 = 2\,[\text{mm}]$, $h_3 = 1\,[\text{mm}]$).

Same computations have been made to observe the influence of the bipolar in the case U_1 and compared values for the 3 meshes have been reported in Figure 4.19 and Figure 4.20. For the case (U_1 : $\sigma^e = 1$, $V = 2.563$), we have compared the variation of the number of iterations for the three meshes $Tet\,1, Tet\,2$ and $Tet\,3$ in function of λ. When comparing with the preceding 2D meshes (Figures 4.19, 4.20), we observed the same behavior and the empiric laws about λ that we have in the first study remain. That is the way we fix this delicate parameter for further computations.

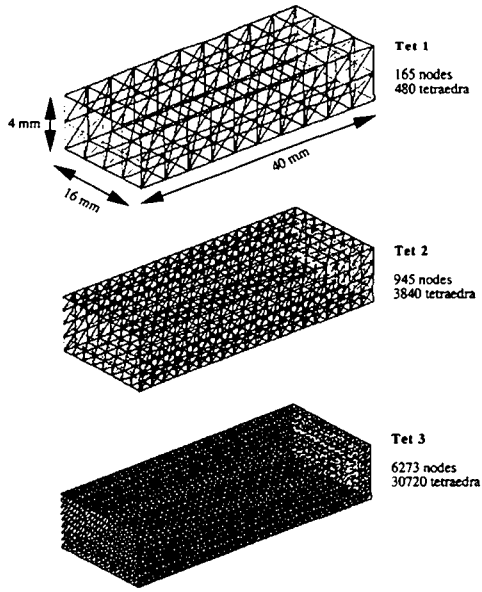

Figure 4.18: Finite element meshes of different steps

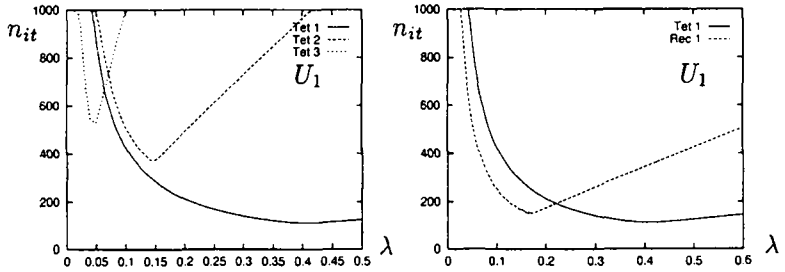

Figure 4.19: $n_{it} = f(\lambda)$

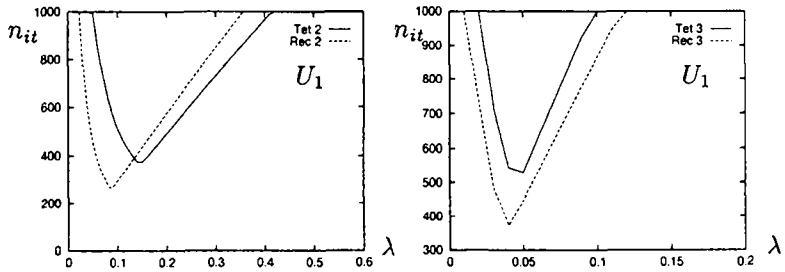

Figure 4.20: $n_{it} = f(\lambda)$

Chapter 5

Computation results

This chapter is exclusively dedicated to two and three-dimensional results obtained from numerical computations of different geometries.

The first experiment is in two dimensions and we compare here numerical simulations results with experiments. This electrolyzer includes one or two bipolar electrodes. Computations are made to test the influence of the orientation in the bipolar electrodes in the reactors. Then results of simulation are compared with experiments.

The second system that has been studied here is the reactor which has been modelled in the work of J.-Y. Salamin [Sal95]. The main differences between the two studies are : our case is three-dimensional and the study comprises the effect of having a small gap in the third dimension and its consequences on the bypass current.

Secondly, we introduce in this case a model concerning the conductivity of the electrolyte. We take in account the bubbles formation during the water electrolysis and compute the same geometry with this new conductivity function.

The third one is the study of a bipolar sphere between two parallel plates. We study in this case the effect of the variation of the conductivity on the behavior of the spheric bipolar electrode.

The fourth one is an application of the 3D model to decontamination of sites and soils polluted with heavy metals, anions, or organic chemicals.

The last experiment deals with the modelling of a three-dimensional electrolyzer for hydrogen production using the finite element method developed under § 3.5.

5.1 Reactor 1 : experimental water electrolyser

5.1.1 Experimental cell of [Mer96]

Figure 5.1 shows a schematic presentation of the bipolar electrochemical cell used. It consists of a Plexiglas rectangular reservoir (width: 5.5, length: 15.6, height: 5 cm).
Two nickel plates (length: 5.3, height : 6, thickness : 0.1 cm) have been placed at the two opposite sides of the reservoir (electrodes 1 and 2) and have been used as current feeders.
A nickel plate (length : 4.4, height : 6, thickness : 0.1 cm) was placed between the two feeders (electrode 3) and can act as a bipolar electrode.
The position of this bipolar electrode is variable and is defined by its distance L from the current feeder 1 and by the angle α.
The configuration used in this part is: $L = 5.0$ cm and $\alpha = 45°$.

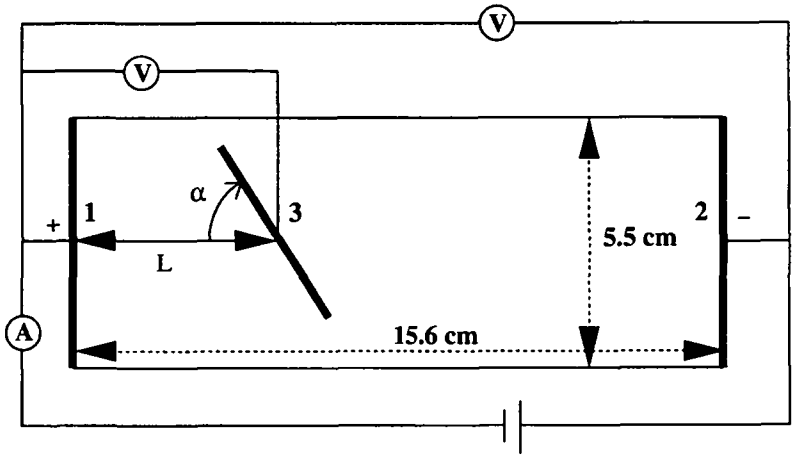

Figure 5.1: Schematic representation of the bipolar cell
1: Anode (Nickel), 2: Cathode (Nickel), 3: Bipolar electrode l=4.4 cm (Nickel), L=5.0 [cm], $\alpha = 45°$, electrolyte: 1N NaOH, T=23°

The electrical circuit used is shown in Figure 5.1.
The measurements were performed by applying a potential difference between the two current feeders (electrodes 1 and 2 in Figure 5.1) and measuring the potential difference between the current feeder 1 (or 2) and the bipolar electrode 3.
The electrolyte used was 1 N NaOH and the working temperature was 23° C.
The extended *Butler-Volmer* function for the Ni electrode in 1 N $NaOH$, has been obtained using a three electrodes system. Ni has been used as working electrode (1.28 cm^2), Pt as counter-electrode and $Hg/Hg_2SO_4.K_2SO_4$ as reference electrode (0.64 [V] (NHE)).
Figure 5.2 shows the behavior of the Ni electrode in 1 N NaOH.

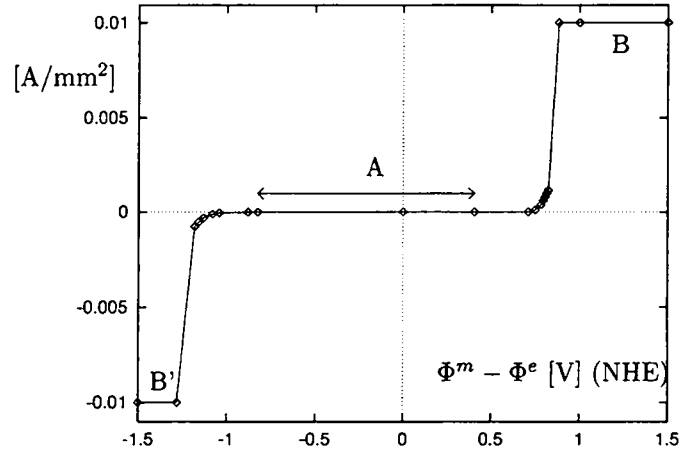

Figure 5.2: Extended *Butler-Volmer* function of Ni electrode in 1N NaOH
A : region of thermodynamic stability of water (1.23 [V])
B, B' : hypothetical limiting current $|i| = 0.01\,[A/mm^2]$

5.1.2 Results with one bipolar electrode

Simulated potential and current distributions

Fig.5.3 shows the computed distribution of potential in the cell with the following input data:

Cell potential	$V = 10$ [V]
Conductivity of the electrolyte	$\sigma^e = 0.017\,[\Omega^{-1}\mathrm{mm}^{-1}]$
Temperature	$T = 23^o$ C

With these data we obtain :

Potential of the bipolar	$V_b = 6.35$ [V]
Total current crossing the cell	$I = 1.28$ [A]

In Figure 5.6, we represent the computed current distribution along each side of the bipolar electrode. This shows the local behavior of the bipolar electrode which cannot be measured.
Figures 5.4 and 5.5 illustrate the computation of the potential of the bipolar electrode V_b. Figure 5.4 shows the graph : $\Phi^m \rightarrow \mathcal{J}(\Phi^m, \Phi^e)$. Then, the solution V_b and Φ^e realized the minimum of $\mathcal{J}(\Phi^m, u^e)$. Figure 5.5 shows that V_b is the physical observable potential of the bipolar electrode when I_{tot}, the total current crossing that electrode is null. In both cases, we obtain the same value of V_b.

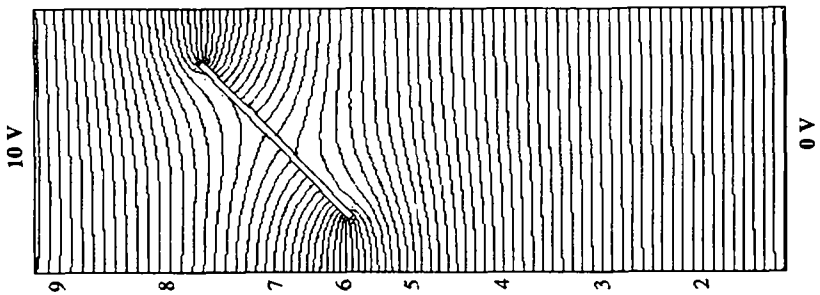

Figure 5.3: Calculated potential distribution of the cell given in Figure 5.1, L=5.0 [cm], $\alpha = 45°$

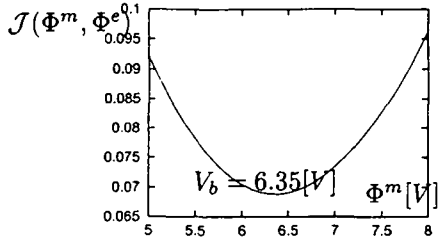

Figure 5.4: Determination of the floating potential V_b using the method of minimization (Figure 4.5)

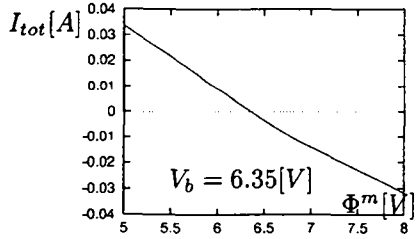

Figure 5.5: Determination of the floating potential V_b using the current conservation method (Figure 4.4)

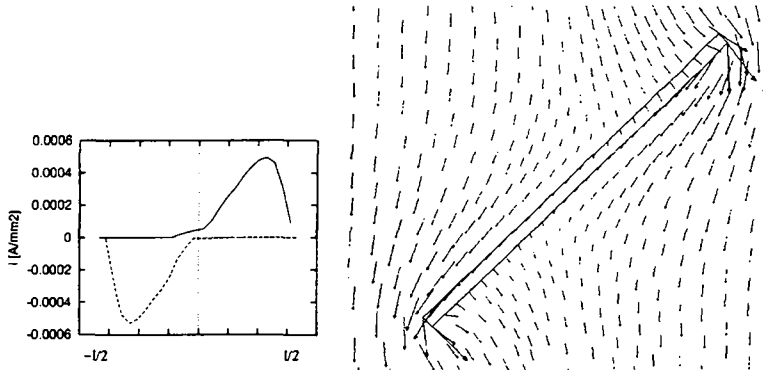

Figure 5.6: Current distribution along the bipolar electrode (l=4.4 cm)

Comparison simulations/measurements of [Mer96]

The graph of 5.7 shows the measured and computed current potential function ($I(V)$) crossing the whole cell, when the cell potential varies from 0 to 10 [V].
The graph of 5.8 shows the measured and computed potential $V_b(V)$ of the bipolar electrode, when the cell potential varies from 0 to 10 V.
Those two graphs show that measurements and simulations perfectly match.

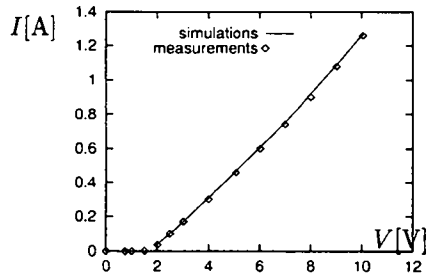

Figure 5.7: Comparison between simulations and measurements, V: cell potential, I: current crossing the cell

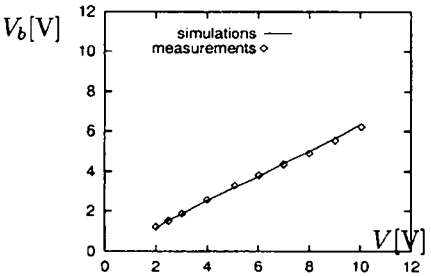

Figure 5.8: Comparison between simulations and measurements, V: cell potential, V_b: difference of potential between the bipolar electrode and the cathode

5.1.3 Results with two bipolar electrodes

A schematic representation of the bipolar cell used for measurements with two bipolar electrodes is given in Figure 5.9.

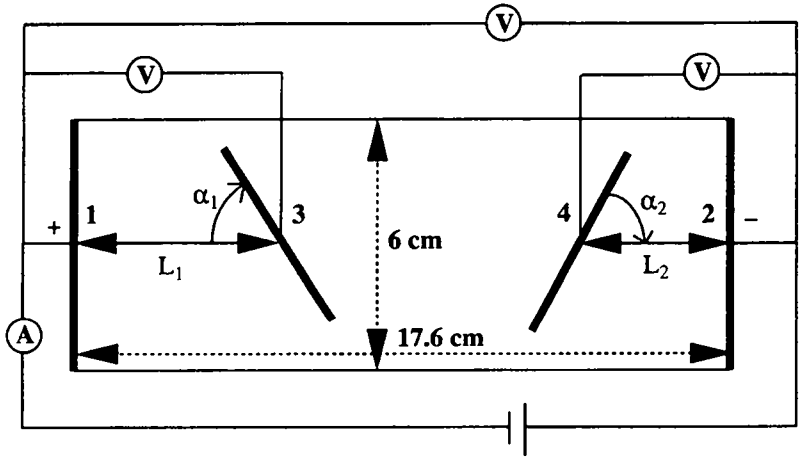

Figure 5.9: Schematic representation of the bipolar cell
1: Anode (Nickel), 2: Cathode (Nickel),
3: Bipolar electrode l=5 cm (Nickel), 4: Bipolar electrode l=5 cm (Nickel), electrolyte: 1N NaOH, T=23°

Three configurations (M1, M2 and M3) have been modelled corresponding to three positions and orientations of the bipolar electrodes (3 and 4). The following table shows where the bipolar electrodes are placed. The length of each bipolar electrode is 5 cm.

Configuration	L_1	α_1	L_2	α_2
	[cm]	[degree]	[cm]	[degree]
M1	5.8	90	11.8	90
M2	5.8	90	8.8	90
M3	5.8	125	11.8	125

The input values are kept identical:

Cell potential	$V = 10$ [V]
Conductivity of the electrolyte	$\sigma^e = 0.017\,[\Omega^{-1}.\mathrm{mm}^{-1}]$
Temperature	$T = 23^o$ C
Current-potential function	Figure 5.2

The mesh of the configuration M3 is shown in Figure 5.10.

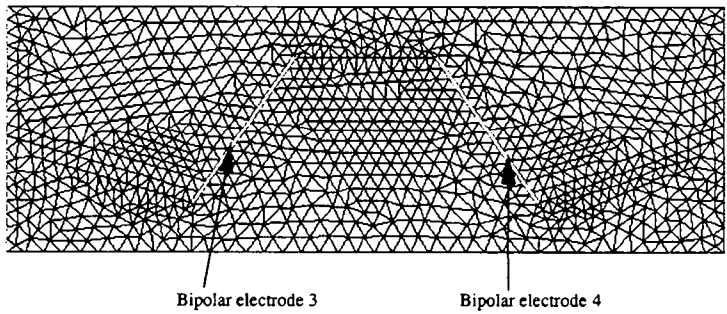

Figure 5.10: Finite element mesh of the cell M3,
1066 nodes, 1958 triangles

The calculated potential distribution is shown in Figure 5.11.

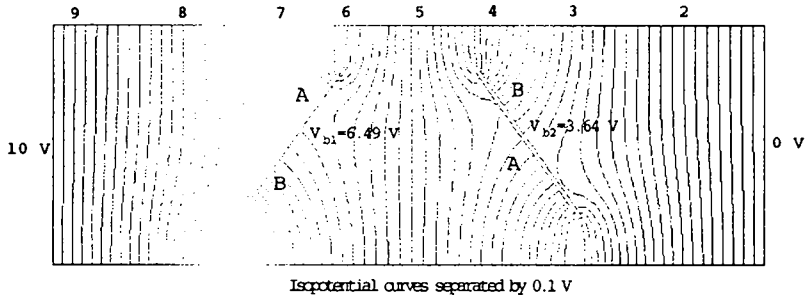

Figure 5.11: Potential distribution in the cell M3

Referring to Figure 5.11, Figure 5.12 and Figure 5.13 give the current distribution along each side of each bipolar electrode.

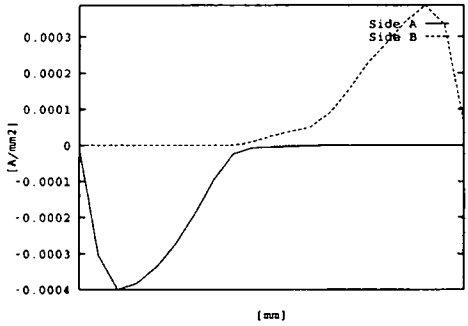

Figure 5.12: Current distribution along the bipolar electrode 3, configuration M3, sides A and B of Figure 5.11

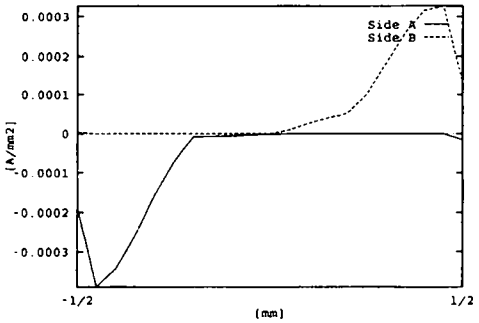

Figure 5.13: Current distribution along the bipolar electrode 4, configuration M3, sides A and B of Figure 5.11

The calculated potential and current distributions along the bipolar electrodes for the the configuration M1 are shown in Figures 5.14 and 5.15

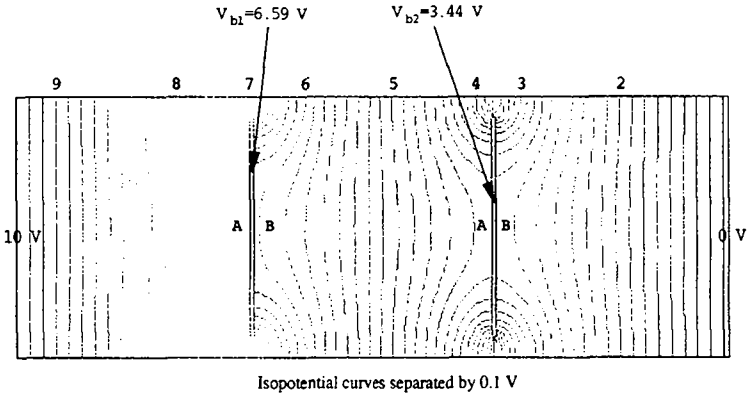

Figure 5.14: Potential distribution in the cell M1, V=10 [V]

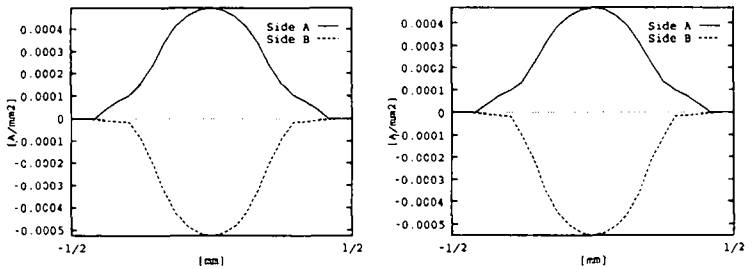

Figure 5.15: Current distribution along the bipolar electrode 3 (left) and bipolar electrode 4 (right),
configuration M1, sides A and B of Figure 5.14

Comparison simulations/measurements of [Mer96]

We give in the following table, compared values of potential of the bipolar electrodes and total current crossing the reactor for the three configurations M1, M2 and M3.
Furthermore, these values have been simulated and measured for two different cell potential (7 [V] and 10 [V]).

U_{cell} [V]: applied difference of potential
V_{b1} [V]: potential of the bipolar electrode 1 **simulated**
V_{b2} [V]: potential of the bipolar electrode 2 **simulated**
V'_{b1} [V]: potential of the bipolar electrode 1 **measured**
V'_{b2} [V]: potential of the bipolar electrode 2 **measured**
I_s [A]: total current crossing the cell **simulated**
I_m [A]: total current crossing the cell **measured**

Mesh	U_{cell}	V_{b1}	V_{b2}	V'_{b1}	V'_{b2}	I_s	I_m
	[V]	[V]	[V]	[V]	[V]	[A]	[A]
M1	10	6.59	3.44	6.47	3.37	1.04	1.05
M1	7	4.53	2.49	4.36	2.33	0.62	0.65
M2	10	5.62	3.4	5.53	3.36	1.04	1.05
M2	7	3.94	2.47	3.77	2.28	0.62	0.65
M3	10	6.49	3.64	6.34	3.38	1.33	1.28
M3	7	4.47	2.66	4.49	2.47	0.80	0.78

Figure 5.16: Compared values of current and potentials

5.1.4 Discussion of the results

The system including one bipolar electrode gives very good results. The two graphs obtained in Figure 5.7 and 5.8 shows clearly that simulations results are very near of experiments.

The variations of the total current in function of the applied potential in Figure 5.7 perfectly follows the experimental data and furthermore depends linearly on the potential as soon as there is an existing current. That means as soon as the applied potential is larger than the thermodynamic barrier of the extended *Butler-Volmer* function.

The same comment is applicable to the variation of bipolar electrode potential in function of the applied potential showed in Figure 5.8.

For the system including two bipolar electrodes, for all configurations M1, M2 and M3, we have obtained values of potential of the bipolar electrodes higher than the experimental values. The relative error for potentials is between 2 and 6 % and between 1 and 4 % for the currents. In all cases, V_{b1} and V_{b2} are higher than V'_{b1} and V'_{b2} in the table given in Figure 5.16.

So, potential jumps at interfaces are smaller than the measured ones and the simulated currents are smaller than the measured ones. Without taking in account the formation of bubbles, we have a very good matching between measurements and simulations.

5.2 Water electrolyzer with one bipolar electrode

The reactor ([Bon92]) built for water electrolysis is made of two current feeders and one bipolar electrode in its middle, it has been modeled by [Sal95] in two dimensions. The study here is three-dimensional: a gap of 2 mm on the y axis has been inserted. Views of this reactor is given in Figure 5.17 and the dimensions of the reactor are given below:

5.2.1 Geometrical data

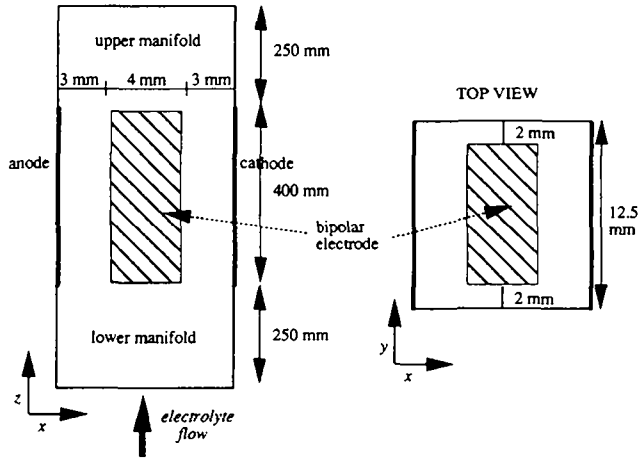

Figure 5.17: Geometry of the reactor

height of the electrodes : 400 mm
thickness of the ending electrodes : 2 mm
thickness of the bipolar electrode : 4 mm
thickness of each compartment : 3 mm
number of compartment : 2
height of the manifold : 250 mm
depth of the electrodes : 12.5 mm
gap for the bipolar electrode : 2 mm

5.2.2 Physical input data

Cell potential : $V = 10$[V]
Electrolyte conductivity (KOH 4M, T=50°) : $\sigma_0^e = 0.02917\,\Omega^{-1}.\text{mm}^{-1}$
The extended *Butler-Volmer* function used here is given by [Sal95]:

$$\varphi(\Phi^m - \Phi^e) = \begin{cases} -10^6\,[\text{A/m}^2] & \text{on }]-\infty; a_c + 6b_c + E_{0c}[\\ -10^{\frac{(\Phi^m - \Phi^e) - E_{0c} - a_c}{b_c}} & \text{on }]a_c + 6b_c + E_{0c}; E_{0c}[\\ 0 & \text{on }]E_{0C}; E_{0a}[\\ 10^{\frac{(\Phi^m - \Phi^e) - E_{0a} - a_a}{b_a}} & \text{on }]E_{0A}; a_a + 6b_a + E_{0a}[\\ 10^6\,[\text{A/m}^2] & \text{on }]a_a + 6b_a + E_{0a}; +\infty[\end{cases}$$

The values for the thermodynamic barrier potential are :

$$E_{0c} = -0.828\text{V},\ E_{0a} = 0.401\text{V}$$

The values of the Tafel parameters are :
For the reduction $a_c = 0.02$ V $b_c = -0.119$ V
For the oxidation $a_a = 0.44$ V $b_a = 0.163$ V

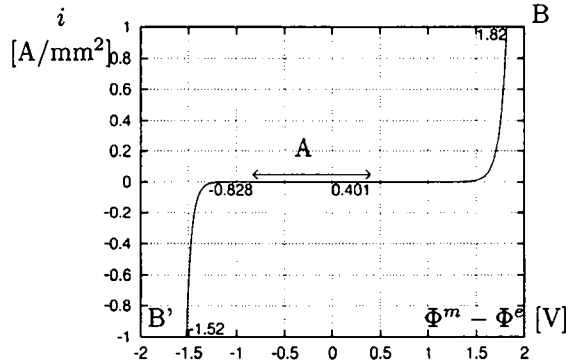

Figure 5.18: Extended *Butler-Volmer* function :
KOH 4M, T=50° and Ni electrode
A : region of thermodynamic stability of water (1.23 [V])
B, B' : hypothetical limiting current $|i| = 1\,[\text{A/mm}^2]$

5.2.3 3D reactor results

Computation results here give the current distributions along each side of the electrode for different depths.

Y0 is the section at the end of the electrode,

Y1 is the section at the quarter depth of the reactor,

Y2 is the section at the half depth of the reactor.

The section Y2 will be compared with the results obtained with the two-dimensional reactor.

Due to the symmetry of the reactor, the results are symmetrical and the curves obtained show the current distributions on one extremity of each electrode. Only the 8 first millimeters are plotted to show the "extremity effect".

From this distance, the current density is constant.

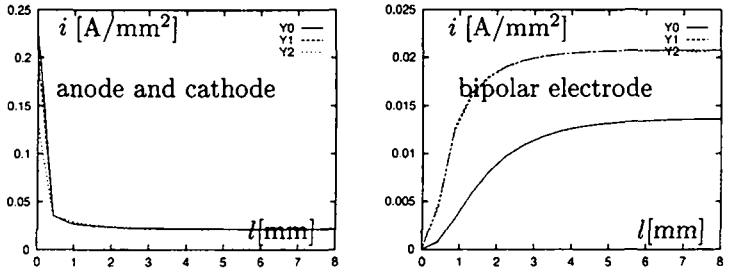

Figure 5.19: Current density in function of the depth

5.2.4 comparison 2D - 3D results

Taking the same physical conditions, we compare the current distribution obtained in 3D for (Y2) with a 2D section (left figure in 5.17).

In terms of current, the total current crossing (entering or outgoing) the reactor I and the current I_b crossing the bipolar electrode are (in the 2D case) :

$$I = 8.4\,[\mathrm{A}] \qquad I_b = 8.27\,[\mathrm{A}]$$

As the bypass is defined as the proportion of the total current which does not cross the bipolar electrode:

$$\Psi = \frac{I - I_b}{I} \tag{5.1}$$

we obtain in this case: $\psi = 0.015$
Taking the 3D case, the situation is different because the surface of the bipolar electrode and the ending electrode are not the same. Then, the total current crossing the reactor I and the current I_b crossing the bipolar electrode are:

$$I = 67.5\,[\mathrm{A}] \qquad I_b = 49.8\,[\mathrm{A}]$$

Then the bypass in this case is : $\Psi = 0.2605$.
The area of the ending electrode are $A = 200 \times 16 = 3200\,[\mathrm{mm}^2]$ and the area of the bipolar electrode are $A_b = 200 \times 12 = 2400\,[\mathrm{mm}^2]$. Then the average current densities are :

2D (ending electrodes)	$j_1 = \frac{I}{l} = 0.0210\,[\mathrm{A/mm}^2]$
2D (bipolar electrode)	$j_2 = \frac{I_b}{l} = 0.0207\,[\mathrm{A/mm}^2]$
3D (ending electrodes)	$j_3 = \frac{I}{A} = 0.0211\,[\mathrm{A/mm}^2]$
3D (bipolar electrode)	$j_4 = \frac{I_b}{A_b} = 0.0207\,[\mathrm{A/mm}^2]$

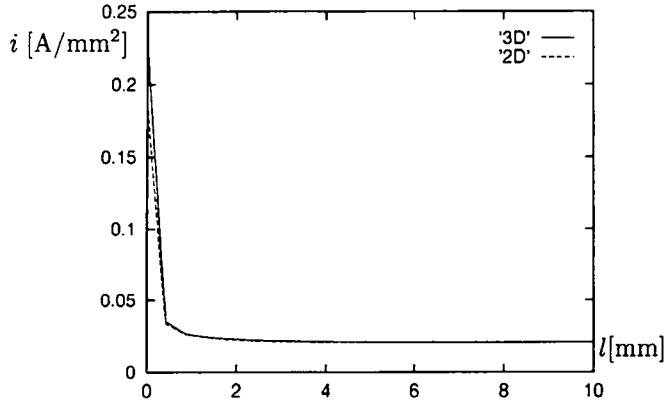

Figure 5.20: Current density along the ending electrodes

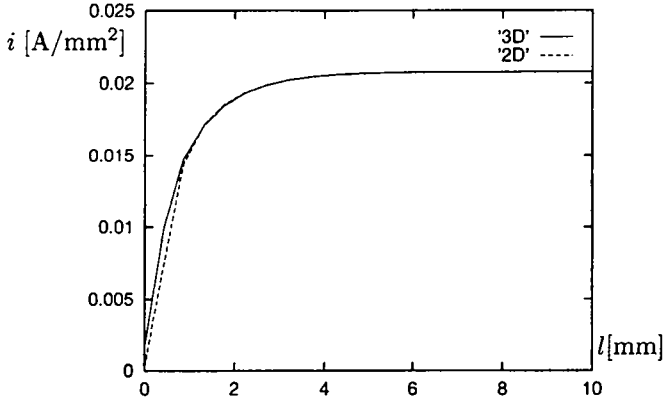

Figure 5.21: Current density along the sides of the bipolar electrode

5.2.5 Effects of the bubbles formation

We use here the same reactor 2D (Figure 5.17) as simulated previously, keeping the same input data :

Physical Input data

Cell potential : $V = 10$ [V]
Extended *Butler-Volmer* function : Figure 5.18

But the main difference here is how we introduce a model for varying the conductivity of the electrolyte in function of the formation of hydrogen and oxygen in the reactor.

Modelling the bubbles formation

Having the oxygen formation at the anode :

$$2H_2O \rightarrow O_2 + 4H^+ + 4e^-$$

$4F(4Faraday = 4 \times 96500\,[\text{As}])$ produce 1 mole of oxygen.
At the cathode:

$$4H^+ + 4e^- \rightarrow 2H_2$$

Then, $4F(= 4 \times 96500\,[\text{As}])$ produce 2 moles of hydrogen.
So, 386000 [A] produce 2 moles of hydrogen and 1 mole of oxygen per second.
From there, we are able to calculate the formed quantities of gas in the reactor in function of the current densities obtained from the last computations, making the hypothesis of an uniform current distribution along the cell.
That means we neglect the extremities effects of the electrodes.

To evaluate the variation of the conductivity, we use the following relations:
the volumetric gas fraction (which measures the proportion of bubbles in the electrolyte) is :

$$\epsilon_z = \frac{\dot{V}_{gz}}{\dot{V}_l + \dot{V}_{gz}} \qquad (\dot{V}_l >> \dot{V}_g) \tag{5.2}$$

then, $0 < \epsilon_z < 1$
$\dot{V}_{gz}$ represents the volume flow rate of the gas in function of the height z of the electrode and $\dot{V}_l$ the volume flow rate of the electrolyte.
The conductivity depends on ϵ_z (Bruggemann's law):

$$\sigma = \frac{\sigma_0}{(1-\epsilon_z)^{-1.5}} \tag{5.3}$$

σ_0 is the conductivity of the electrolyte without bubbles.
From these formulas, we can evaluate the volumetric gas fraction and therefore the conductivities for the reactor (Figure 5.17) as following:
The electrolyte flow comes from the bottom, and reactions take place at electrodes. The conductivity of the electrolyte in the lower manifold is constant and equal to σ_0.
Taking a section of thickness 1 [mm] at the level z of the reactor ($0 \leq z \leq 400$), with the electrolyte circulating at 1 [m/s] in a section of $2 \times 3 = 6$ [mm^2], we obtain:

$$\dot{V}_l = 6000\,[\text{mm}^3/\text{s}]$$

Taking account of the bypass current (5.1) $\Psi = 0.015$ estimated in § 5.2.4, this electrolyzer needs $4F$ to produce :

$$(3 + 3(1-\Psi))22.4 \cdot 10^6\,[\text{mm}^3/\text{s}] \text{ of gas}$$

Having an average current density of $i_1 = 0.00210\,[\text{A/mm}^2]$, each mm^2 of the reactor produce

$$\dot{V}_{gz} = \frac{(3 + 3(1-\Psi))22.4 \cdot 10^6 \cdot 0.00210}{386000} z = 7.257z$$

Finally,

$$\epsilon_z = \frac{7.257z}{7.257z + 6000} \quad (0 < z < 400)$$

Then, the conductivity of the electrolyte in function of the height of the reactor is :

$$\sigma_1^e(z) = \begin{cases} 0.02917 & \text{for } -250 \leq z < 0 \\ \dfrac{0.02917}{(1 - \dfrac{7.257z}{7.257z + 6000})^{-1.5}} & \text{for } 0 \leq z \leq 400 \\ 0.0199 & \text{for } 400 < z \leq 650 \end{cases}$$

the evolution of σ_1^e is given in Figure 5.22

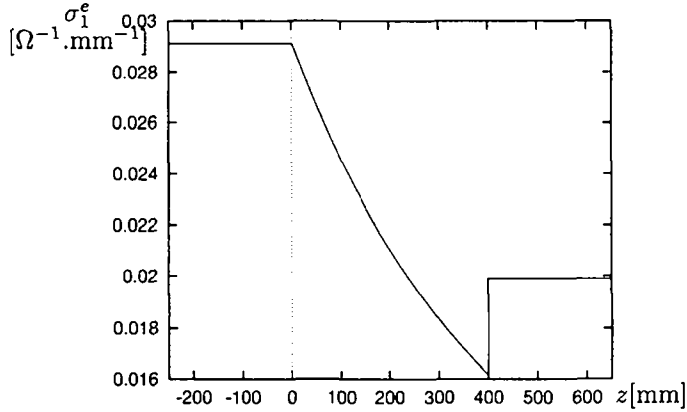

Figure 5.22: Conductivity in function of the height of the reactor

To obtain the conductivity in the upper manifold, we take the highest value of the bubble density and consider constant an homogeneous mix of the electrolyte and bubbles.
Then computations give a total current $I = 6.37\,[\mathrm{A}]$ instead of the initial current of $I = 8.4\,[\mathrm{A}]$. This difference is due to the estimation of the value of the conductivity which has been calculated with $I = 8.4\,[\mathrm{A}]$ and is over-estimated. It gives a too small value for the conductivity. To get a more realistic model, we adjust the function σ_1^e by taking the last current obtained ($I = 6.37\,[\mathrm{A}]$) and that gives

the following function (Figure 5.23) for the conductivity:

$$\dot{V}_{gz} = \frac{(3+3(1-\Psi))22.4 \cdot 10^6 \cdot 0.00159}{386000} z = 5.499z$$

$$\sigma_2^e(z) = \begin{cases} 0.02917 & \text{for } -250 \leq z < 0 \\ \dfrac{0.02917}{(1 - \dfrac{5.499z}{5.499z + 6000})^{-1.5}} & \text{for } 0 \leq z \leq 400 \\ 0.02164 & \text{for } 400 < z \leq 650 \end{cases}$$

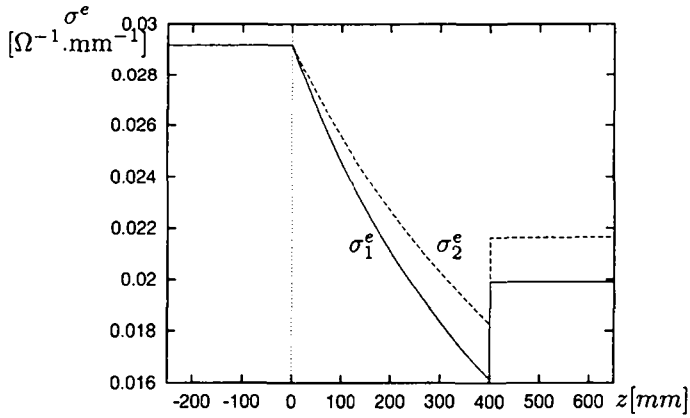

Figure 5.23: Conductivity in function of the height of the reactor

the following results for the current distribution along each side of the electrodes are given in the following figures (5.24 and 5.25).

Figure 5.26 shows the evolution of the number of iterations n_{it} in function of the parameter λ of the method of *Kellogg* (§ 3.3).

The optimal value of λ has the same order of magnitude as the conductivity of the electrolyte.

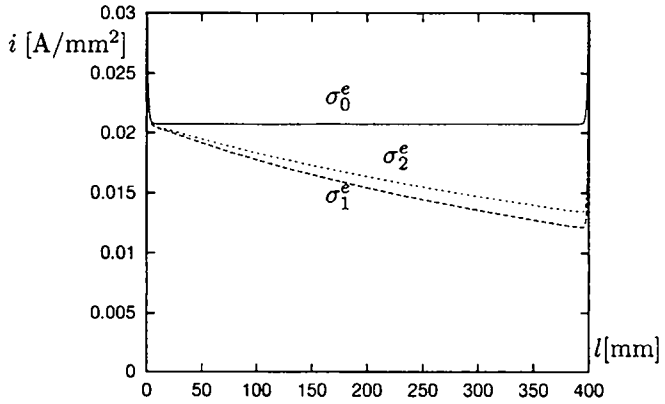

Figure 5.24: Current density along the ending electrode of length l=400 [mm]

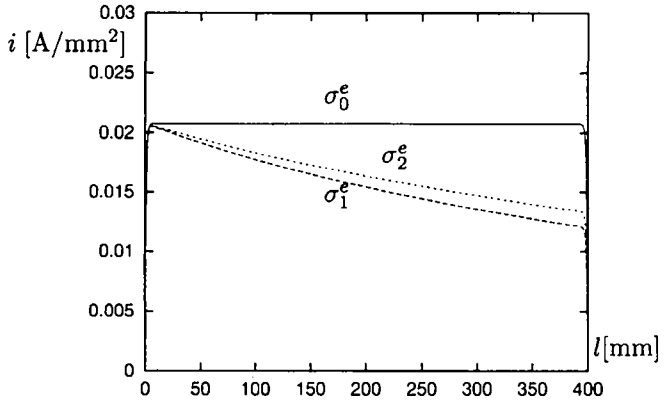

Figure 5.25: Current density along the sides of the bipolar electrode of length l=400 [mm]

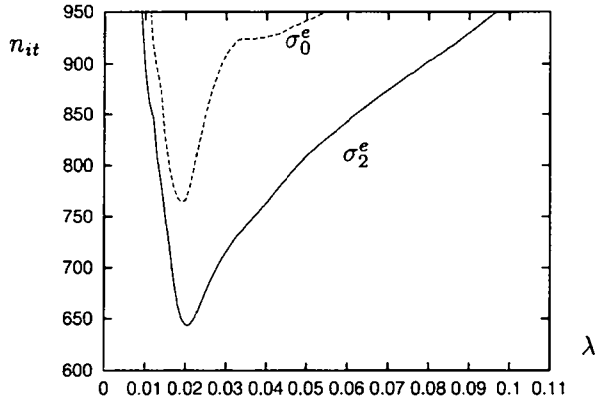

Figure 5.26: Optimal value of λ (§ 3.3) for σ_0^e and σ_2^e

5.2.6 Effects of translating the bipolar electrode

We use here the same reactor (Figure 5.17) as simulated previously, keeping the same input data but the bipolar electrode is translated of 1 mm to the cathode as shown in Figure 5.27.

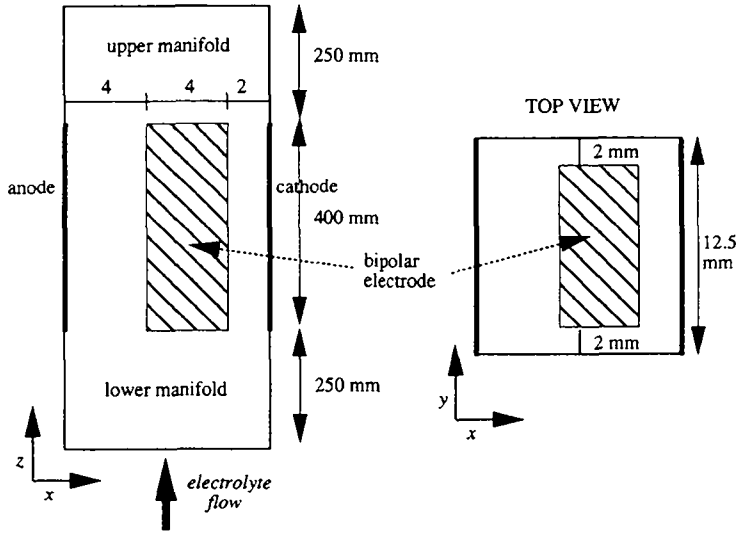

Figure 5.27: Geometry of the reactor (bipolar electrode translated)

The conductivity function σ_3^e is now recalculated taking account of the bubbles formation in the reactor.

$$\sigma_3^e(z) = \begin{cases} 0.02917 & -250 \leq z < 0 \\ \dfrac{0.02917}{(1 - \dfrac{2.75z}{2.75z + 4000})^{-1.5}} & 0 \leq z \leq 400,\ 0 \leq x \leq 4 \\ \dfrac{0.02917}{(1 - \dfrac{2.75z}{2.75z + 2000})^{-1.5}} & 0 \leq z \leq 400, 8 \leq x \leq 10 \\ 0.02 & 400 < z \leq 650 \end{cases}$$

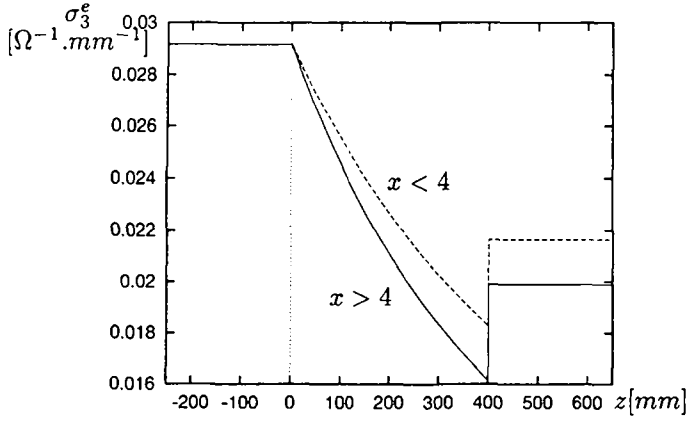

Figure 5.28: Conductivity in function of the height of the reactor

The evolution of σ_3^e is given in Figure 5.28.
Results for the current distribution along each side of the electrodes are given in Figures 5.29 and 5.30.

Potential of the bipolar electrode

When the bipolar electrode is centered, due to the symmetrical geometry and the identical function of conductivity on both sides of the bipolar, the potential of the bipolar is 5 [V] $(V/2)$ in every case.
When the bipolar electrode is translated, its potential and the current crossing the electrodes become:

$U_b = 4.29$ [V] if $\sigma = \sigma_0$ $I = 8.4$ [A], $I_b = 8.27$ [A]
$U_b = 4.13$ [V] if $\sigma = \sigma_3$ $I = 6.4$ [A], $I_b = 6.3$ [A]

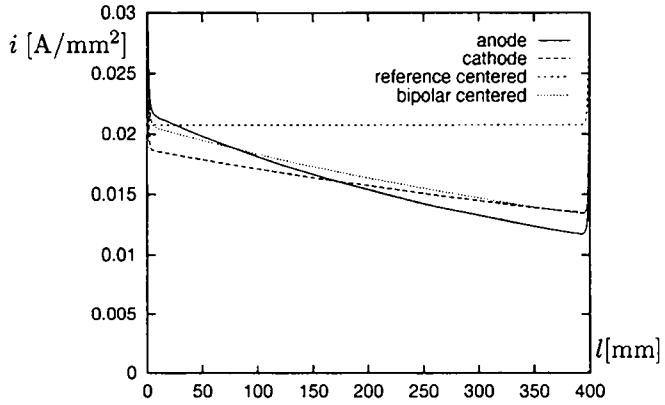

Figure 5.29: Current density along the ending electrodes with σ_3^e

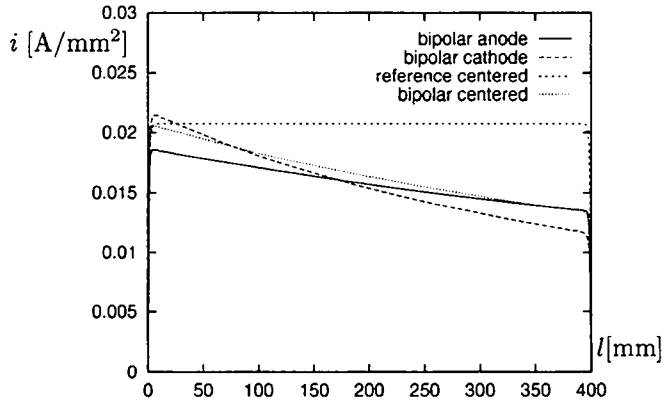

Figure 5.30: Current density along the sides of the bipolar electrode with σ_3^e

5.3 A spherical bipolar electrode in an electrolytic cell

5.3.1 Parameters study

This three-dimensional reactor is made of two current feeders and one centered sphere which acts as a bipolar electrode. A view of this reactor is given in Figure 5.31 and the dimensions of the reactor are given below.
We are interested here in investigating the behavior of the bipolar electrode in terms of current distributions and current bypass.
The current bypass (Ψ) calculated in these simulations is defined as the proportion of the total current crossing the cell which does not cross the bipolar electrode (Eq. (5.1)).
If I represents the total current and I_b the current entering (or outgoing) the surface of the spherical bipolar electrode, therefore,

$$\Psi = \frac{I - I_b}{I} = 1 - \frac{I_b}{I}$$

We perform then the following numerical simulations to compute the bypass function of the following parameters:

1. Three different values of cell potential have been applied :
   $V = 10$ [V], $V' = 7.5$ [V], $V'' = 5$ [V]

2. The conductivity of the electrolyte (constant in the whole cell) has been scanned from very small values ($\sigma^e = 10^{-4}[\Omega^{-1}\text{mm}^{-1}]$) to larger one ($\sigma^e = 10^{-1}\,[\Omega^{-1}\text{mm}^{-1}]$)

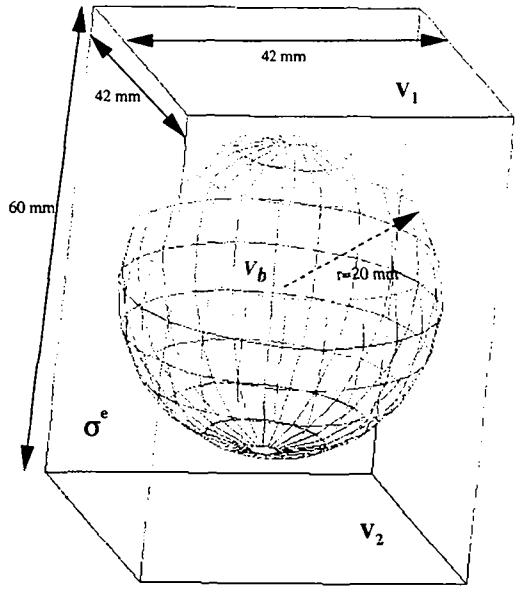

Figure 5.31: Geometry of the reactor

Anode and cathode dimensions :	42×42 mm
height of the reactor :	60 mm
diameter of the sphere :	40 mm

The extended *Butler-Volmer* function used here is the one given in Figure 5.2.

The finite element mesh built for this computation has 13838 nodes and 62808 tetraedral elements.

5.3.2 Results and discussion

In all cases the potential of the sphere is $V_b = \dfrac{V_1 - V_2}{2}$.

Figures 5.32, 5.34 and 5.36 represent the bypass in function of the conductivity for the three different cell potentials applied.

Figures 5.33, 5.35 and 5.37 represent the currents I and I_b in function of the conductivity for the three different cell potentials applied.

The current density distributions on the surface of the sphere are shown on Figure 5.40 for the three cell potential applied : 10, 7.5 and 5 [V].

The current distributions on one of the ending electrode (anode and cathode have the same behavior) for the three cell potential applied : 10, 7.5 and 5 [V] are shown in Figure 5.38 for $\sigma^e = 10^{-3}[\Omega^{-1}\text{mm}^{-1}]$.

When $\sigma^e = 10^{-2}[\Omega^{-1}\text{mm}^{-1}]$, the current density distributions on the surface of the sphere is shown in Figure 5.41 for the three different cell potential applied : 10, 7.5 and 5 [V].

The current distributions on one of the ending electrode (anode and cathode have the same behavior) are shown in Figure 5.39. When the applied potential is 10 [V] in this case, the current density distribution on the ending electrode is constant and equal to $i = 10^{-2}$ [Amm^{-2}].

For those three applied potentials in this reactor, the bypass increases with the conductivity (Figure 5.32, 5.34 and 5.36). The minimal bypass is obtained for the smallest conductivity, but in this case, I and I_b are very small (Figure 5.33, 5.35 and 5.37).

In function of σ^e, I has a fast growing slope until it reaches a constant value of $I_{lim} = 17.64$ [A], reached independently of the applied cell potential. More the cell potential is high, more the slope of $I(\sigma^e)$ is high. This limiting value is due to the extended *Butler-Volmer* function (Figure 5.2). We have introduced in this function a limitation of the current density of $i = 10^{-2}$ [Amm^{-2}] (see Figure 5.2).

Then the total current crossing the cell is in this case $I = i.S$ where S represents the area of the ending electrode :

$S = 42 \times 42 = 1764$ mm^2 and $I = I_{lim} = 17.64$ [A].

The current entering (or outgoing) the sphere has a maximum which corresponds to a conductivity from where the total current I becomes constant, but it is not the minimal bypass as it has been defined in Eq.(5.1).

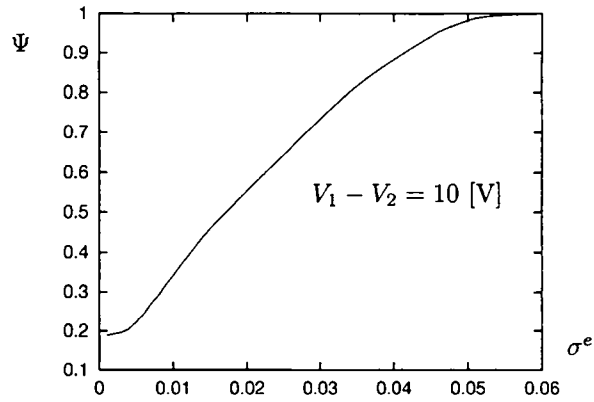

Figure 5.32: Bypass in function of σ^e $[\Omega^{-1}\text{mm}^{-1}]$

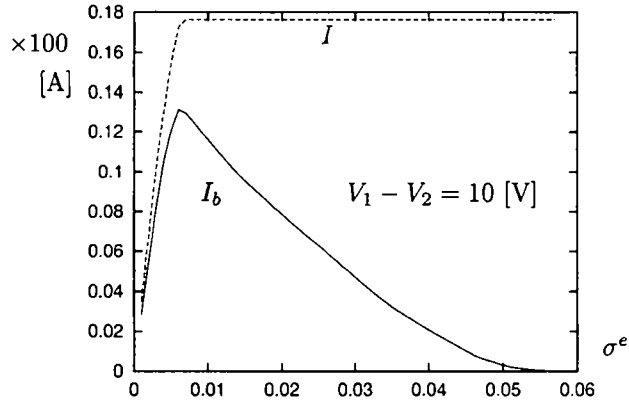

Figure 5.33: I and I_b [A] in function of σ^e $[\Omega^{-1}\text{mm}^{-1}]$

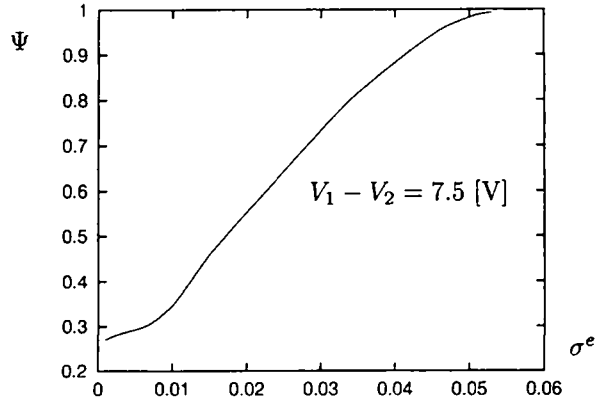

Figure 5.34: Bypass in function of σ^e [Ω^{-1}mm^{-1}]

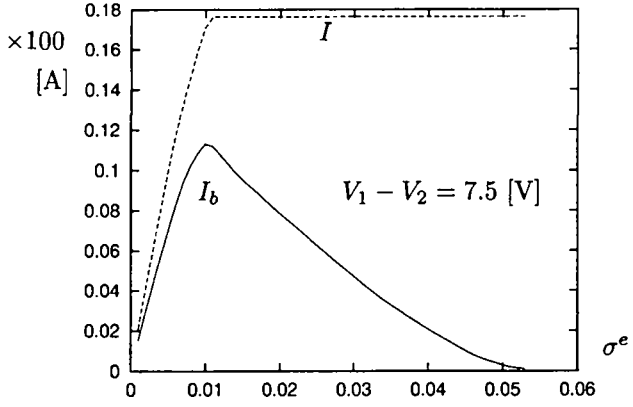

Figure 5.35: Currents I and I_b [A] in function of σ^e [Ω^{-1}mm^{-1}]

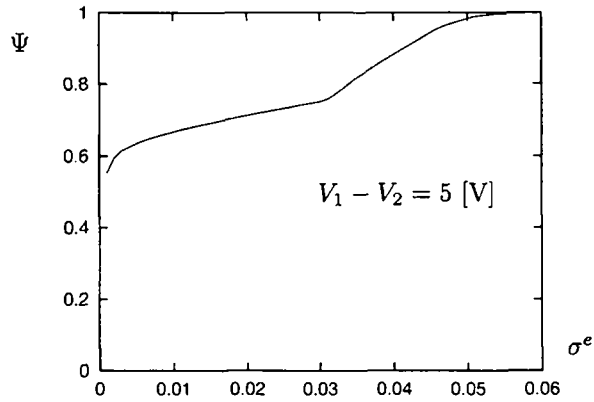

Figure 5.36: Bypass in function of σ^e $[\Omega^{-1}\text{mm}^{-1}]$

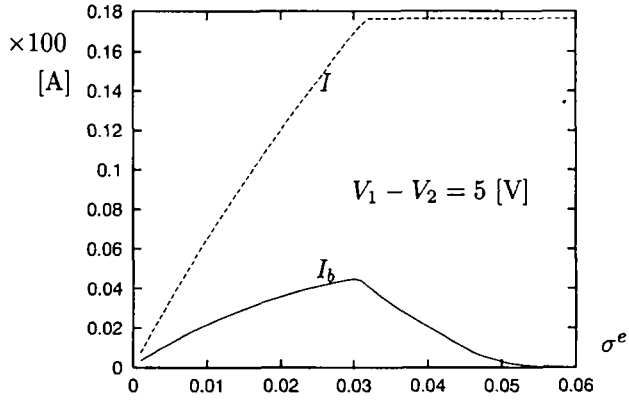

Figure 5.37: Currents I and I_b [A] in function of σ^e $[\Omega^{-1}\text{mm}^{-1}]$

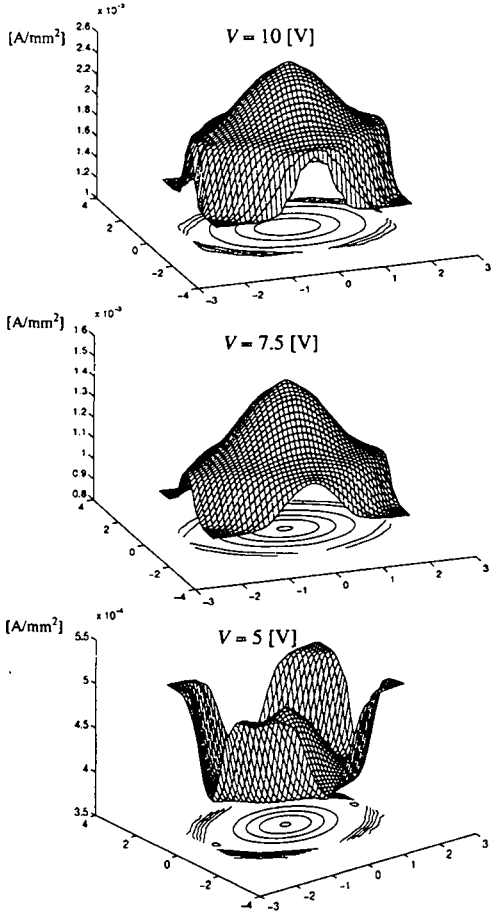

Figure 5.38: Current density distribution at the anode for V=10, 7.5 and 5 [V] and $\sigma^e = 10^{-3}\,[\Omega^{-1}\mathrm{mm}^{-1}]$

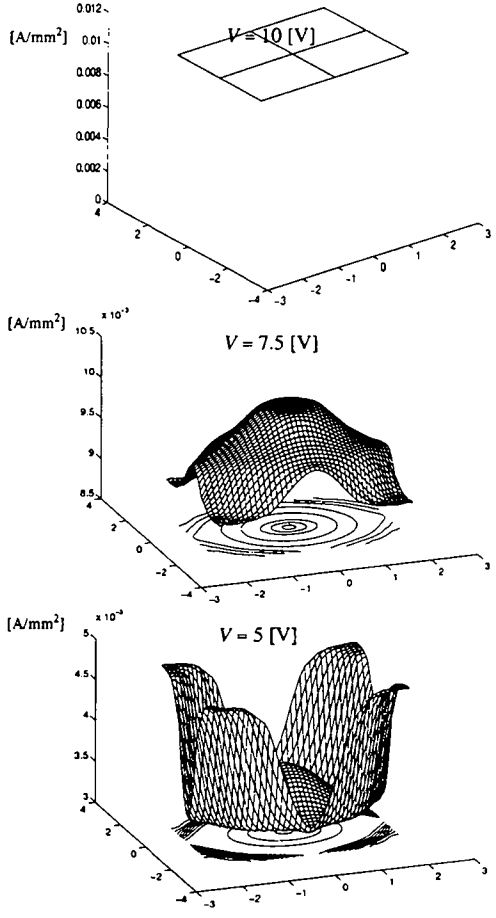

Figure 5.39: Current density distribution at the anode for V=10, 7.5 and 5 [V] and $\sigma^e = 10^{-2}\,[\Omega^{-1}\mathrm{mm}^{-1}]$

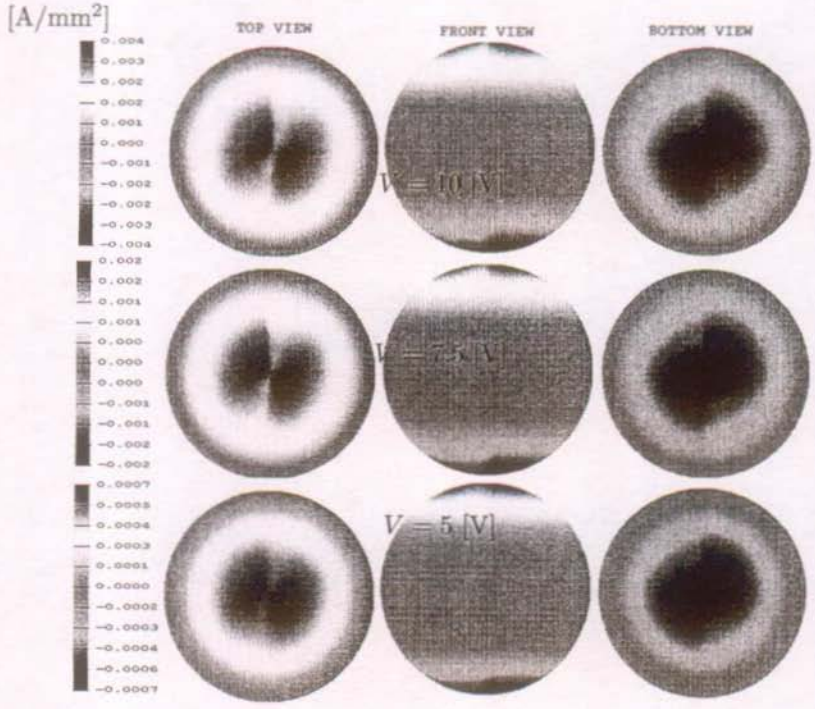

Figure 5.40: Current density distribution [A/mm^2] on the sphere with $\sigma^e = 10^{-3}\,[\Omega^{-1}\mathrm{mm}^{-1}]$

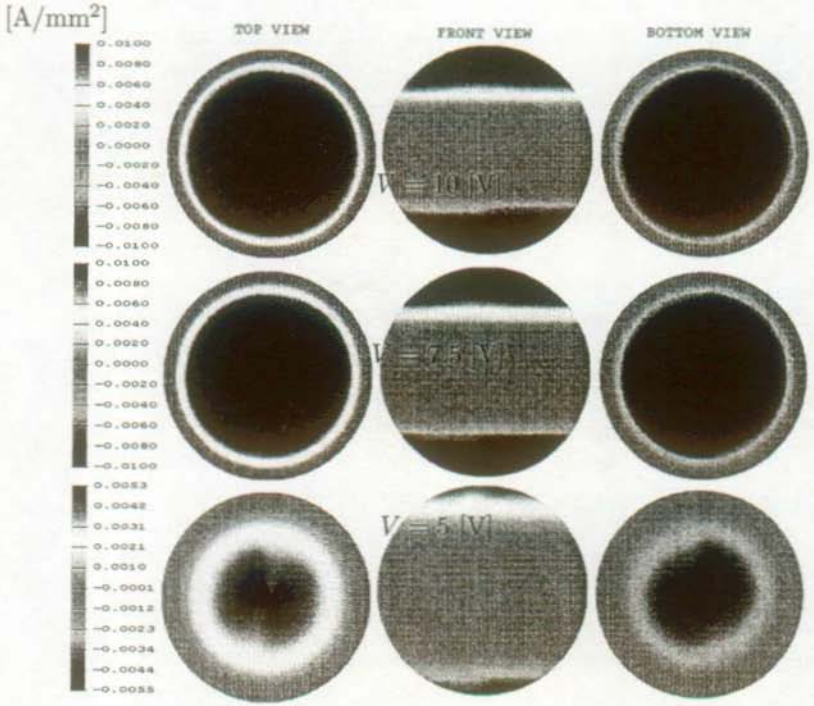

Figure 5.41: Current density distribution [A/mm^2] on the sphere with $\sigma^e = 10^{-2}\,[\Omega^{-1}\mathrm{mm}^{-1}]$

5.4 Contaminated soil

Processes like electroosmosis or electromigration have been used to promote the movement and the extraction of pollutant in soils. Their effectiveness depends on electric field strength, field orientation, soil electrochemistry and subsurface conditions. Studies of potential distribution in soil are rare. Only cases with homogeneous conditions are considered. [RP87] gives the results of two-dimensional numerical simulations showing the distribution of equipotential lines for two different cases of electrodes position. [RB96] presents the study of electrode placement for isotropic and homogeneous material surface and the resulting electric field.

This study is based on a field experiment presented by [LPS89]. The site of a galvanizing plant is considered, which corresponds to sandy clay contaminated with zinc. The original geometry of the soil has been complicated by the introduction of a rock, symbolizing a non conductive element and by the introduction of an electrical wire who may act as a bipolar electrode in the system.

The aim of this study is the modelling of the electric field through a 3D geometry characterized by a non homogeneous medium.

5.4.1 Experimental conditions

The general geometry (Figure 5.42) of the system is similar to the field experiment. The four zones defined by [LPS89] have been kept (Figure 5.43), for each of them we have defined the equivalent concentration of zinc chloride. Table 5.44 presents the evolution of zones concentration as a function of height. The conductivities corresponding to these concentrations have been calculated by V. Merminod [Mer97] for kaolinite-electrolyte mixture.

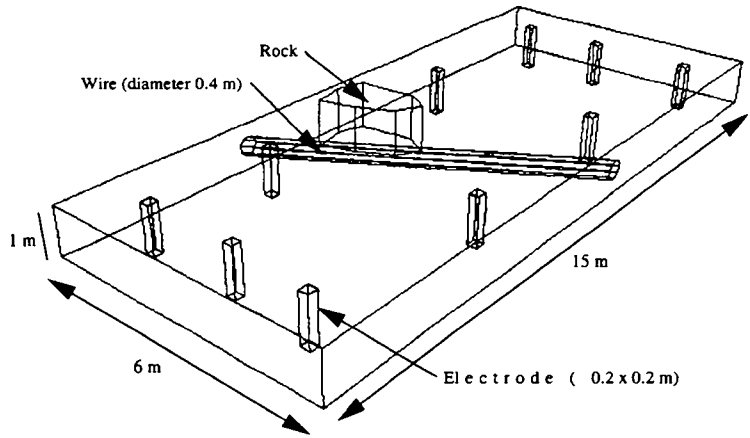

Figure 5.42: General geometry with electrodes and wire placement

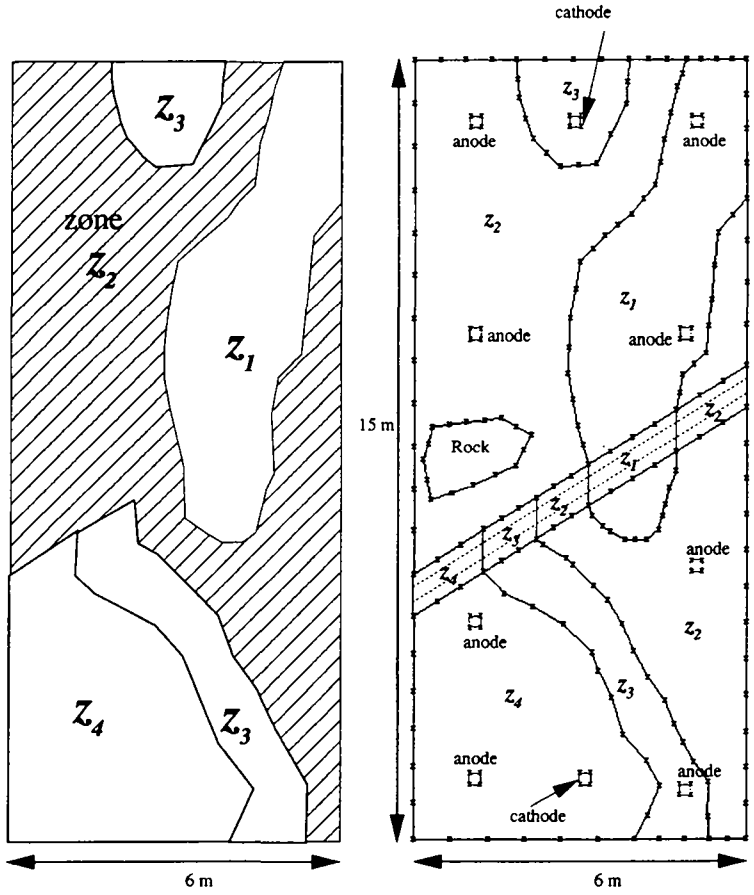

Figure 5.43: Section of the field at half-depth: different zones (left figure) , electrodes and wire placement (right figure)

The following assumptions have been made.

1. Sandy clay is similar to kaolinite clay: surface charge, porosity and conductivity of saturated mixture are equivalent.
2. The system is saturated by water.
3. $ZnCl_2$ is the main specie present in the system.

	0-30 cm	30-50 cm	50-100 cm
zone 1	2.935E-05	1.468E-05	3.669E-06
zone 2	2.202E-05	1.101E-05	2.935E-06
zone 3	7.338E-06	5.137E-06	1.101E-06
zone 4	1.101E-06	7.338E-07	2.935E-07

Figure 5.44: Distribution of concentration [mol.cm^{-3}] for each zone as a function of the height [LPS89]

	0-30 cm	30-50 cm	50-100 cm
zone 1	6.77E+00	3.59E+00	1.20E+00
zone 2	5.18E+00	2.79E+00	1.04E+00
zone 3	1.99E+00	1.52E+00	6.39E-01
zone 4	6.39E-01	5.59E-01	4.64E-01

Figure 5.45: Distribution of conductivity [Ω^{-1}.m^{-1}] for each zone as a function of the height [Mer97]

5.4.2 Simulations conditions

The finite element mesh built for this case contains 8 anodes and 2 cathodes. Referring to [LPS89], the order of magnitude of the applied electrical field is 40 [V/m]. Then, the potential applied here is 60 [V].

The diameter of the electrodes is 0.2 [m], and the diameter of the wire is 0.4 [m].

The finite element mesh we have built has 4128 nodes and 18780 tetrahedral elements. Two cases have been studied depending on the extended *Butler-Volmer* function. Figure 5.46 shows the two different functions chosen. The main difference between the two curves "BV 1" and "BV 2" is the thermodynamic barrier of 1.23 [V] that has been suppressed in "BV 2" and which is furthermore symmetrical. We have taken this function to get more risks of polarizing the wire (bipolar electrode). That is what we would like to illustrate. "BV 2" corresponds physically to a corrosion and dissolution of a metal. The thermodynamic barrier is small (0.5 [V]) and oxidation and reduction curves as symmetrical.

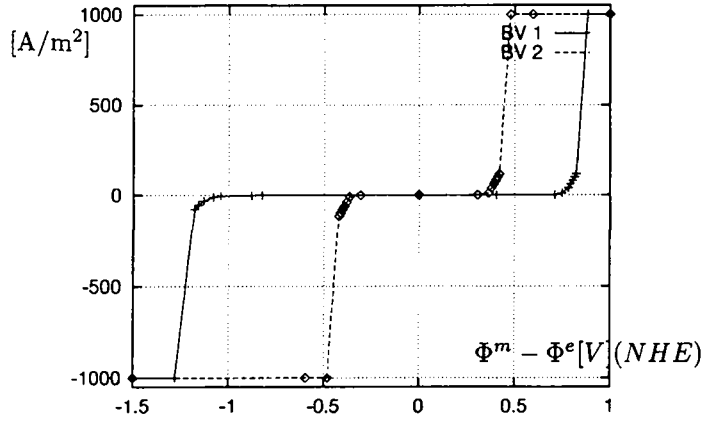

Figure 5.46: Extended *Butler-Volmer* functions used for simulations BV1 : Extended *Butler-Volmer* function of Ni electrode in 1N NaOH BV2: BV1 without thermodynamic barrier and symmetrical (anodic branches)

5.4.3 Results

Using the curve "BV 1", we determine the potential of the wire which is 57.5 [V]. In this case, there is no current crossing the wire. It is not polarized and did not act as a bipolar electrode but as a insulator. Figure 5.47 shows equipotential surfaces in the soil and Figure 5.50 shows the current distribution in a (plane) section at the half-depth of the soil.

In the other case (with the interfacial function "BV 2"), we determine the potential of the wire which is now 58.2 [V], and it is polarized. The wire acts as a bipolar electrode. Figure 5.48 and Figure 5.49 show the potential distribution around the wire. Figure 5.51 shows the current distribution in a (plane) section at the half-depth of the soil.

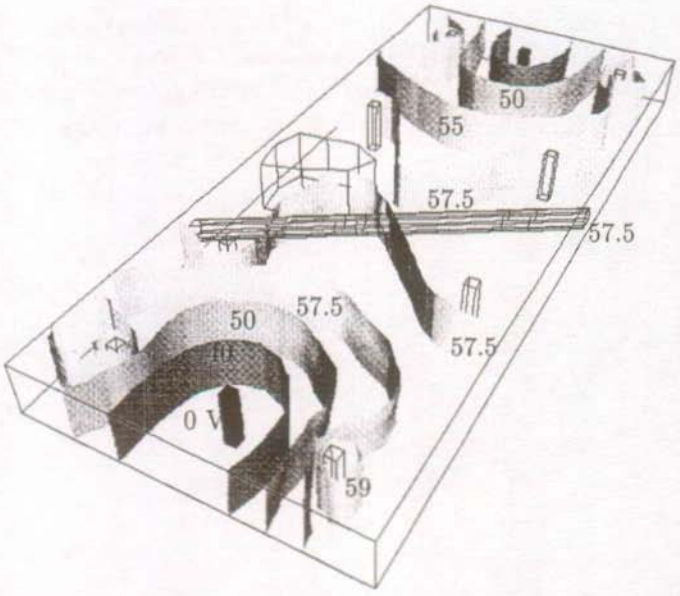

Figure 5.47: Potential distribution [V], (case BV 1)

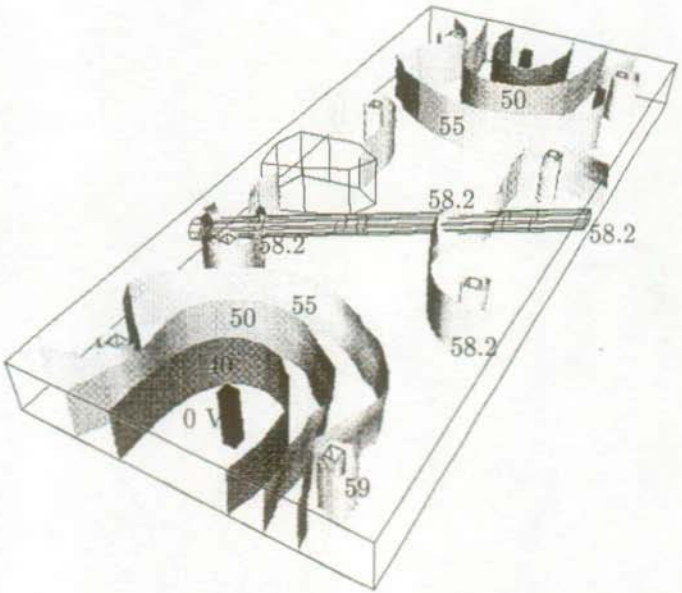

Figure 5.48: Potential distribution [V], (case BV 2)

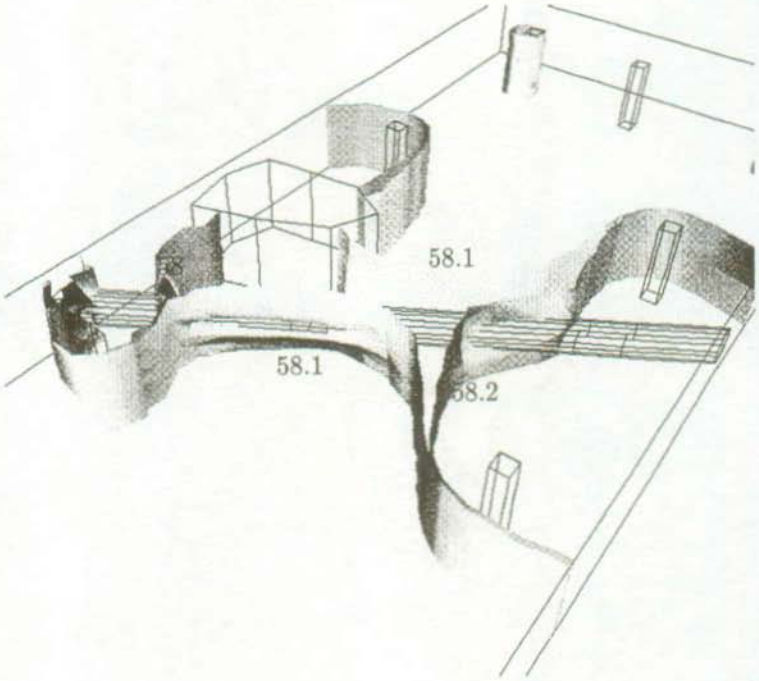

Figure 5.49: Equipotential surfaces [V] around the wire, (case BV 2)

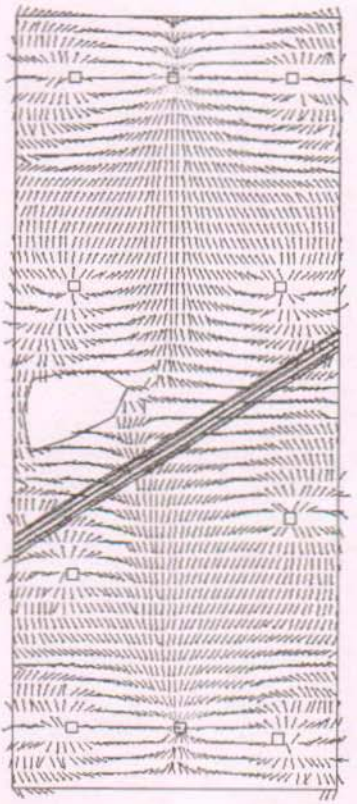

Figure 5.50: Current distribution at half-depth, (case BV 1)

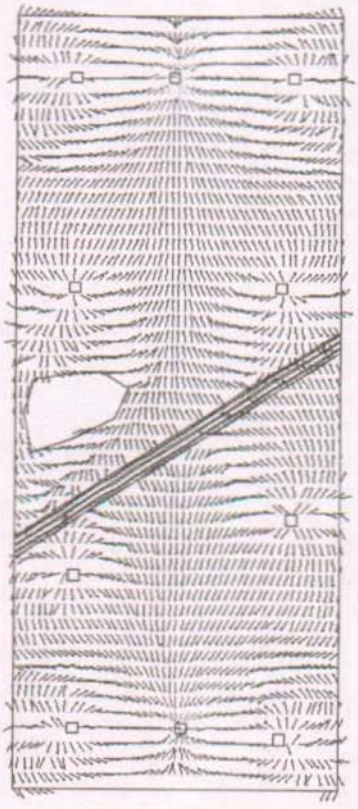

Figure 5.51: Current distribution at half-depth, (case BV 2)

5.5 Electrolyzer for hydrogen production [FM95a]

From the geometric and physical data provided by [ALY], we have built a three-dimensional mesh using the method exposed in § 3.5. This has been achieved by generating a two-dimensional mesh as shown in Figure 5.52, and elevating this mesh to build the whole reactor. Then, some parts of the cell has a different conductivity depending on the environment as shown in Figure 5.53.

The different slices having their own height are represented in Figure 5.54.

The applied cell potential is: $V = 3.4$[V] and due to the symmetry of the problem, the bipolar electrode has a potential which is the half of the cell potential: $V_b = 1.7$[V].

The conductivities of the different environments are:

$$\begin{array}{ll} \text{electrolyte:} & \sigma_e = 0.14\ \Omega^{-1}.mm^{-1} \\ \text{membrane:} & \sigma_p = 0.04\ \Omega^{-1}.mm^{-1} \\ \text{insulator:} & \sigma_i = 10^{-9}\ \Omega^{-1}.mm^{-1} \end{array}$$

The electrodes potential are considered as equipotential and therefore are not meshed. All electrodes have then a null height.

We represent in Figures 5.56 and 5.57, two sections on which we will calculate the potential distributions. These sections 1 and 2 are taken respectively along the z axis of the reactor and in the canals of the reactors.

In Figures 5.56 and 5.57, the potential distributions are displayed, only values between the two electrodes (1.7 V et 0 V) are represented.

The calculated potentials are situated between 1 and 1.2 volts in a portion of cell fed with 1.7 V.

The extended *Butler-Volmer* function is the one given in Figure 5.18.

Values of potential jumps at interfaces:

1.7 - 1.2 = 0.5 V (metal-electrolyte) et
0 - 1 = -1 V (electrolyte-metal)

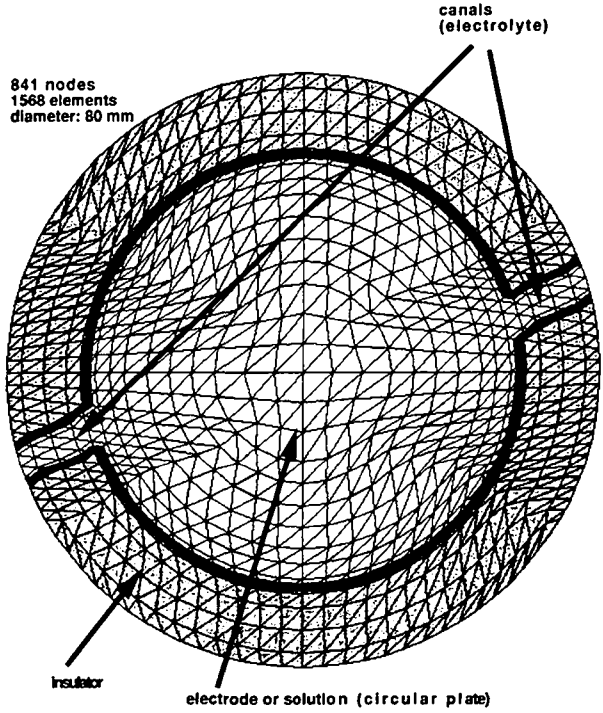

Figure 5.52: Two-dimensional mesh (base of the cell)

Value of the total current crossing the cell:

The sum of the elementary contributions on the surface of each electrode gives: $I = 2.2358[\mathrm{A}]$.

The average current density is: $3635[\mathrm{A/m^2}]$
The average current density given by [ALY] is around $3000[\mathrm{A/m^2}]$.

The model presented here give the same results independently of the number of stacks, the difference of potential between two electrodes is always 1.7 V.

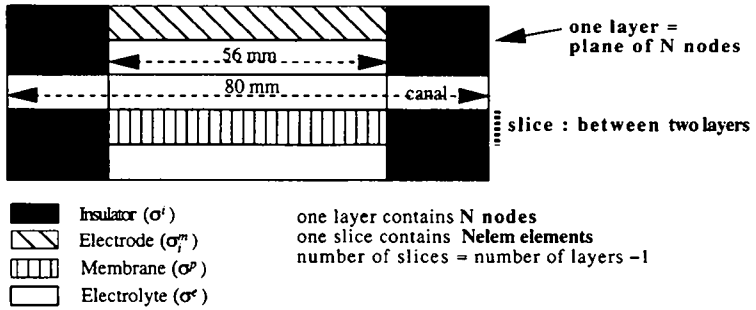

Figure 5.53: Schematic representation of the height of the cell)

For a such computation, we have built meshes made of 30 layers of 1000 nodes per layer. We have to store then, for the over-all stiffness matrix **A**, 11 vectors of 30000 components and 10 other vectors for computations.

That means 600000*4 bytes = 2,4 MByte of dynamic memory to allocate.
With a Silicon Graphics (processor R4000), the computation time (including reading and writing all the files) is around 30 minutes.

In 30 minutes, the program solve nearly 100 iterations of *Kellogg*, and at each iteration, it solves a linear system of 30000 equations within 30 iterations.

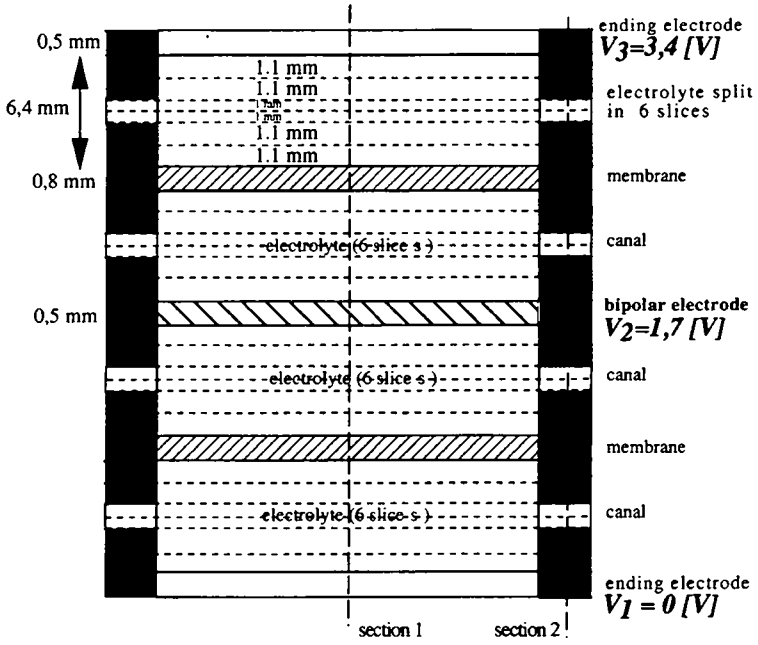

Figure 5.54: Different slices of the cell

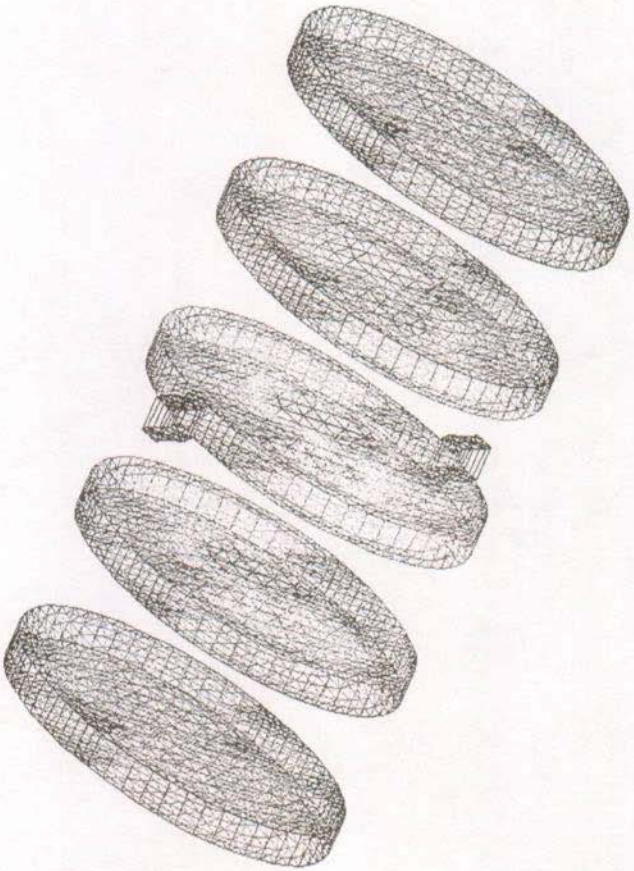

Figure 5.55: Finite element mesh of the cell without insulators

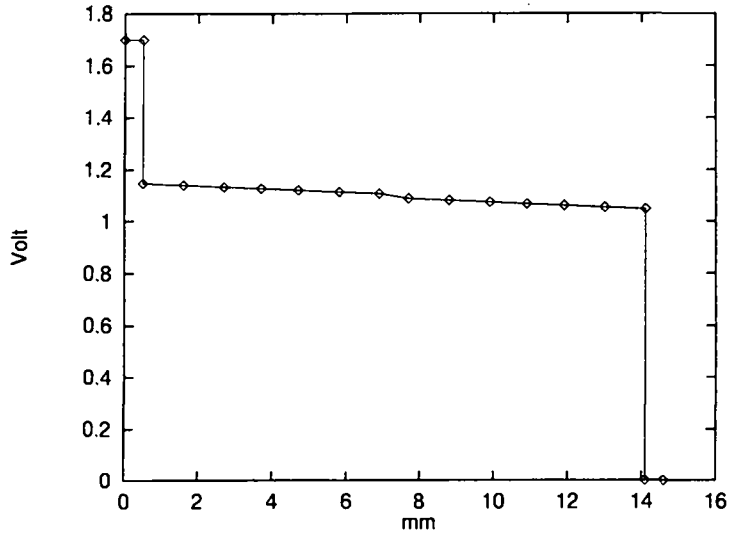

Figure 5.56: Potential distributions (section 1) along the central axis

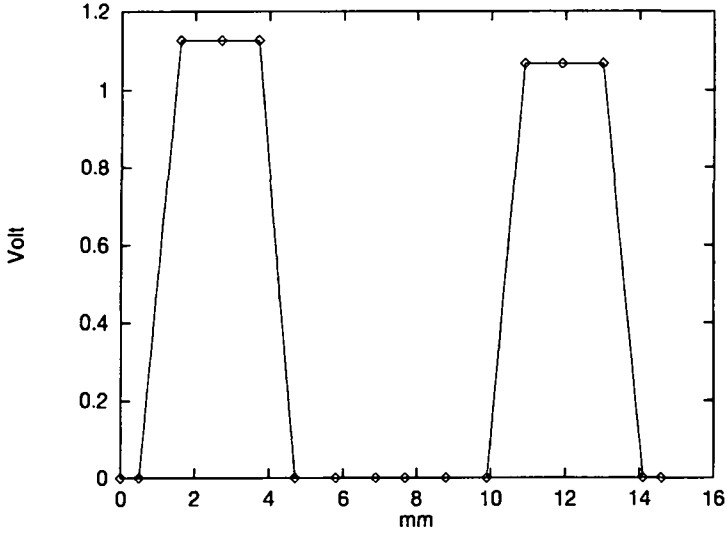

Figure 5.57: Potential distributions (section 2) in the canal

Conclusion

In this thesis we presented a method which enabled us to simulate numerically current and potential distributions in electrochemical bipolar cells of any geometry, in two and three dimensions. The mathematical model and the subsequent numerical approximations which lead to the final system for the determination of bipolar electrodes potential were presented in detail. In particular, we used a finite element method and we have built a software tool for computing potential and current distributions for any geometry and any physical parameters.

Several major difficulties have been encountered during the work. The first one was the problem of the determination of the unknown floating potential of the bipolar electrodes. This has successfully been achieved using a method of minimization, which gives fast and good results.

The second difficulty concerned the numerical solving of the nonlinear systems of equations, particularly the optimization of the time computation. For the iterative methods we employed, the convergence depended on values of very delicate parameters. A very small deviation of such parameters strongly effected the system. An empirical study of the parameter λ in the method of *Kellogg* has been undertaken, and some "recipes" have been applied to find its optimal value.

The third major difficulty was the building of three-dimensional geometries. We used a commercial package but it is still a heavy tool and the handling of three-dimensional finite element meshes is not

always flexible.

Our main objectives have finally been achieved, our model and software were partially validated through comparison with one-dimensional calculations for simple cases and through physical measurements of water electrolyzers in two dimensions. We have obtained very good agreement between the two, however, much remains to be done.

For future work we mention 4 points as concluding remarks:

1. In two dimensions, results have been only partially validated: total current and potentials of bipolar electrodes have been compared and have given good results. But, concerning current distributions on electrodes, no comparison have been undertaken. It should be interesting for instance to compare those distributions with measurements of thickness of metallic deposition to validate our predictive curves.

2. A validation of the model including the formation of bubbles has to be made in two and three dimensions. For the moment, only simulations taking into account the effects of the variation of the conductivity have been made and experimental measurements should be compared with numerical simulations for any kind of electrolyzer with bipolar electrodes.

3. The method we used for solving the nonlinear system of equations has many advantages such as short time computations, few intermediary vectors to store, applicable to any non decreasing current-potential function. But its main disadvantage is the delicate *Kellogg parameter* λ, on which the algorithm strongly depends. Enhancements on this side should be made by a theoretical analysis of this parameter in function of the finite element mesh and of the conductivities.

   In order to get a flexible software tool, this parameter should be automatically chosen by the software in function of the input data.

4. To solve a complete problem in three dimensions, a large time is needed for data pre-processing: building a three-dimensional finite element mesh takes a lot of time and this is an important limiting point of the method we used. Furthermore, 3D meshes occupies a lot of memory.

   Due to that limitation, 3D problems are not easily accessible by a non-specialist person, because it implies the separate knowledge of the mesh generator, some programming knowledge, and the use of graphical packages. In two dimensions, portability between our code developed on Silicon Graphics workstation and PCs is ensured and there is no problem of memory limitation. A good perspective is to get a independent package running on PC, including the mesh generator, the code and the post-processing.

Appendix A

Proofs concerning the PROBLEMS 1A, 2A, and 3A

A.1 Transformation of the PROBLEM 2A to the PROBLEM 1A

The PROBLEM 1A (2.6) is:

PROBLEM 1A : search Φ^e and V_b such that:

$$
\left\{
\begin{array}{lcll}
div(\sigma^e \underline{grad}\,\Phi^e) & = & 0 & \text{in } \Omega^e \\
< \sigma^e \underline{grad}\,\Phi^e \,|\, \underline{\nu} > & = & 0 & \text{on } \Gamma_N \\
< \sigma^e \underline{grad}\,\Phi^e \,|\, \underline{\nu} > + \varphi\,(V - \Phi^e) & = & 0 & \text{on } \Gamma^1(V) \\
< \sigma^e \underline{grad}\,\Phi^e \,|\, \underline{\nu} > + \varphi\,(-\Phi^e) & = & 0 & \text{on } \Gamma^2(0) \\
< \sigma^e \underline{grad}\,\Phi^e \,|\, \underline{\nu} > + \varphi\,(V_b - \Phi^e) & = & 0 & \text{on } \Gamma^m \\
\displaystyle\int_{\Gamma^m} \varphi\,(V_b - \Phi^e) ds & = & 0 &
\end{array}
\right.
$$

The PROBLEM 2A (2.8) is:

PROBLEM 2A : find $\Phi^e \in H$ and $V_b \in \mathbb{R}$ such that:

$$\left\{\begin{array}{l} \displaystyle\int_{\Omega^e} \sigma^e \, < \, \underline{grad}\, \Phi^e \,|\, \underline{grad}\, u^e \, > d\tau \\ \\ \displaystyle + \int_{\Gamma^1(V)} \varphi\,(V \, - \, \Phi^e)\, u^e ds + \int_{\Gamma^2(0)} \varphi\,(-\,\Phi^e)\, u^e ds \\ \\ \displaystyle - \int_{\Gamma^m} \varphi\,(V_b \, - \, \Phi^e)\,(c^m - u^e) ds = 0 \\ \\ \text{for all } u^e \in H \text{ and } c^m \in \mathbb{R} \end{array}\right.$$

Proposition

If Φ^e and V_b are regular (of class C^2) solutions of the PROBLEM 2A (2.8), they are also solutions of the PROBLEM 1A (2.6).

Proof

Let $\mathcal{D}(\Omega^e)$ the set of functions indefinitely differentiable with support in Ω^e.

Let us choose $u^e \in \mathcal{D}(\Omega^e) \subset H$ and $c^m = 0$, then (2.8) becomes:

$$\int_{\Omega^e} \sigma^e \, < \, \underline{grad}\, \Phi^e \,|\, \underline{grad}\, u^e \, > d\tau = 0 \qquad \text{for all } u^e \in \mathcal{D}(\Omega^e).$$

Then using the *Green*'s formula (which is verified for regular functions):

$$\begin{aligned} \int_{\Omega^e} < \underline{grad}\, f \,|\, \underline{grad}\, g \, > d\tau \; &= \int_{\partial\Omega^e} f \, < \underline{grad}\, g \,|\, d\underline{s} \, > \\ &\quad - \int_{\Omega^e} f div(\underline{grad}\, g) d\tau \end{aligned}$$

The integrals of the frontiers are null and we obtain:

$$0 = -\int_{\Omega^e} u^e \, div(\sigma^e \underline{grad}\, \Phi^e) d\tau \qquad \text{for all } u^e \in \mathcal{D}(\Omega^e).$$

Thus, by hypothesis $div(\sigma^e \underline{grad}\, \Phi^e)$ is continuous on Ω^e:

$$\boxed{div(\sigma^e \underline{grad}\, \Phi^e) = 0 \qquad \text{in } \Omega^e} \tag{A.1}$$

We have to prove now that the boundary conditions are verified.
Let us choose functions of $\mathcal{D}(\Omega^e \cup \Omega^m)$ (Ω^m is the domain occupied by the bipolar electrode, $\partial\Omega^m = \Gamma^m$).
These functions are null on $\Gamma^1(V), \Gamma^2(0)$ and Γ_N.
Let E this set of functions on which we consider the restriction to $\overline{\Omega^e}$. $E \subset H$.
With $u^e \in E$, and c^m =0, (2.8) becomes:

$$\int_{\Omega^e} \sigma^e < \underline{grad}\, \Phi^e \mid \underline{grad}\, u^e > d\tau + \int_{\Gamma^m} \varphi\,(V_b - \Phi^e) u^e ds = 0$$
for all $u^e \in E$.

Then using *Green*'s formula:

$$\begin{aligned} &\int_{\partial\Omega^e} u^e < \sigma^e \underline{grad}\, \Phi^e \mid \underline{ds} > - \int_{\Omega^e} u^e \, div(\sigma^e \underline{grad}\, \Phi^e) d\tau + \\ &\int_{\Gamma^m} \varphi\,(V_b - \Phi^e) u^e ds = 0 \qquad \text{for all } u^e \in E. \end{aligned} \tag{A.2}$$

with (A.1) and $u^e = 0$ on $\partial\Omega^e \backslash \Gamma^m$, (A.2) becomes:

$$\int_{\Gamma^m} u^e < \sigma^e \underline{grad}\, \Phi^e \mid \underline{ds} > + \int_{\Gamma^m} \varphi\,(V_b - \Phi^e) u^e ds = 0$$
for all $u^e \in E$.

and

$$\int_{\Gamma^m} [< \sigma^e \underline{grad}\, \Phi^e \mid d\underline{s} > + \varphi\,(V_b - \Phi^e)]\, u^e ds = 0 \qquad \text{(A.3)}$$

for all $u^e \in E$.

Finally, (with $d\underline{s} = \underline{\nu} ds$) :

$$\boxed{< \sigma^e \underline{grad}\, \Phi^e \mid \underline{\nu} > + \varphi\,(V_b - \Phi^e) = 0 \qquad \text{on } \Gamma^m} \qquad \text{(A.4)}$$

In the same manner we obtain:

$$\boxed{< \sigma^e \underline{grad}\, \Phi^e \mid \underline{\nu} > + \varphi\,(V - \Phi^e) = 0 \qquad \text{on } \Gamma^1(V)} \qquad \text{(A.5)}$$

and

$$\boxed{< \sigma^e \underline{grad}\, \Phi^e \mid \underline{\nu} > + \varphi\,(-\Phi^e) = 0 \qquad \text{on } \Gamma^2(0)}$$

Let us prove now that $\int_{\Gamma^m} \varphi\,(\Phi^m - \Phi^e) = 0$

Choosing $u^e \in \mathcal{D}(\Omega^e)$, $u^e = 0$ on $\Gamma^1(V) \cup \Gamma^2(0) \cup \Gamma_N \cup \Gamma^m$, (2.8) becomes:

$$\int_{\Omega^e} \sigma^e < \underline{grad}\, \Phi^e \mid \underline{grad}\, u^e > d\tau - \int_{\Gamma^m} \varphi\,(V_b - \Phi^e) c^m ds = 0$$

for all $u^e \in \mathcal{D}(\Omega^e)$ and for all $c^m \in \mathbb{R}$

Hence

$$\boxed{\int_{\Gamma^m} \varphi\,(V_b - \Phi^e) ds = 0} \qquad \text{(A.6)}$$

Equations (A.1), (A.4), (A.5), (A.1), and (A.6) are part of the differential formulation which is precisely the PROBLEM 1A (2.6).

A.2 Transformation of the PROBLEM 3A to the PROBLEM 2A

the PROBLEM 3A (2.12) is:

PROBLEM 3A : find $\Phi^e \in H$ and $V_b \in \mathbb{R}$ which realized the minimum of $J(\Phi^m, u^e)$.

More precisely:

$$\boxed{J(V_b, \Phi^e) \leq J(\Phi^m, u^e)}$$

with

$$\boxed{\begin{aligned} J(\Phi^m, u^e) = \frac{1}{2}\int_{\Omega^e} \sigma^e \|\underline{grad}\, u^e\|^2 d\tau \\ + \int_{\Gamma^1} \psi(V - \Phi^e) ds \; + \; \int_{\Gamma^2} \psi(-\Phi^e) ds \\ + \int_{\Gamma^m} \psi(\Phi^m - u^e) ds \end{aligned}}$$

For all $\Phi^m \in \mathbb{R}$ and all $u^e \in H$.

Theorem

If (V_b, Φ^e) satisfies the PROBLEM 3A (2.12), (V_b, Φ^e) is solution of the PROBLEM 2A (2.8).

Proof

We suppose that V_b and Φ^e realized the minimum of $J(\Phi^m, u^e)$
We calculate the difference:

$$J(V_b + \alpha\Phi^m, \Phi^e + \alpha u^e) - J(V_b, \Phi^e), \qquad \alpha \in \mathbb{R}$$

$$J(V_b + \alpha\Phi^m, \Phi^e + \alpha u^e) - J(V_b, \Phi^e) =$$

$$\begin{aligned}
&\frac{1}{2}\int_{\Omega^e} \sigma^e \|\underline{grad}\,\Phi^e + \alpha u^e\|^2 d\tau + \int_{\Gamma^1(V)} \psi(V - \Phi^e - \alpha u^e) ds \\
&+ \int_{\Gamma^2(0)} \psi(-\Phi^e - \alpha u^e) ds + \int_{\Gamma^m} \psi(V_b + \alpha\Phi^m - \Phi^e - \alpha u^e) ds \\
&-\frac{1}{2}\int_{\Omega^e} \sigma^e \|\underline{grad}\,\Phi^e\|^2 d\tau - \int_{\Gamma^1(V)} \psi(V - \Phi^e) ds \\
&- \int_{\Gamma^2(0)} \psi(-\Phi^e) ds - \int_{\Gamma^m} \psi(V_b - \Phi^e) ds
\end{aligned}$$

$$J(V_b + \alpha\Phi^m, \Phi^e + \alpha u^e) - J(V_b, \Phi^e) =$$

$$\begin{aligned}
&\alpha \int_{\Omega^e} \sigma^e < \underline{grad}\,\Phi^e | \underline{grad}\,u^e > d\tau \; + \; \frac{\alpha^2}{2}\int_{\Omega^e} \sigma^e \|\underline{grad}\,u^e\|^2 d\tau \\
&- \int_{\Gamma^1(V)} [\psi(V - \Phi^e - \alpha u^e) - \psi(V - \Phi^e)]\, ds \\
&- \int_{\Gamma^2(0)} [\psi(-\Phi^e - \alpha u^e) - \psi(-\Phi^e)]\, ds \\
&- \int_{\Gamma^m} [\psi(V_b + \alpha\Phi^m - \Phi^e - \alpha u^e) - \psi(V_b - \Phi^e)]\, ds
\end{aligned}$$

using the *intermediate value theorem*:
$f(a+h) - f(a) = hf'(a+h) + \frac{1}{2}f''(a+\theta h), \qquad 0 < \theta < 1$
f is continuous on $[a, a+h]$
f' is continuous on $]a, a+h[$
f'' is bounded on $]a, a+b[$

we have:

$$
\begin{aligned}
&J(V_b+\alpha\Phi^m,\Phi^e+\alpha u^e)-J(V_b,\Phi^e)= \\
&\alpha\int_{\Omega^e}\sigma^e<\underline{grad}\,\Phi^e|\underline{grad}\,u^e>d\tau\;+\;\frac{\alpha^2}{2}\int_{\Omega^e}\sigma^e\|\underline{grad}\,u^e\|^2d\tau \\
&+\alpha\int_{\Gamma^1(V)}\psi'(V-\Phi^e)u^eds+\frac{\alpha^2}{2}\int_{\Gamma^1(V)}\psi''(V-\Phi^e-\alpha\theta u^e)(u^e)^2ds \\
&+\alpha\int_{\Gamma^2(0)}\psi'(-\Phi^e)u^eds+\frac{\alpha^2}{2}\int_{\Gamma^2(0)}\psi''(-\Phi^e-\alpha\theta u^e)(u^e)^2ds \\
&+\alpha\int_{\Gamma^m}\psi'(V_b-\Phi^e)u^eds+\frac{\alpha^2}{2}\int_{\Gamma^m}\psi''(V_b-\Phi^e+\alpha\Phi^m-\alpha\theta u^e)(u^e)^2ds
\end{aligned}
$$

with

$$\psi(x)\;=\;\int_0^x\varphi(y)\,dy$$

φ is a nondecreasing, continuous, bounded function in $\mathbb{R}$,
and we suppose furthermore that φ' is bounded, we have then:

$$
\begin{aligned}
&J(V_b+\alpha\Phi^m,\Phi^e+\alpha u^e)-J(V_b,\Phi^e)= \\
&\alpha\,[\int_{\Omega^e}\sigma^e<\underline{grad}\,\Phi^e|\underline{grad}\,u^e>d\tau\;+\int_{\Gamma^1(V)}\varphi(V-\Phi^e)u^eds \\
&+\int_{\Gamma^2(0)}\varphi(-\Phi^e)u^eds+\int_{\Gamma^m}\varphi(V_b-\Phi^e)(\Phi^m-u^e)ds\,] \\
&+\frac{\alpha^2}{2}\,[\int_{\Omega^e}\sigma^e\|\underline{grad}\,u^e\|^2d\tau+\int_{\Gamma^1(V)}\varphi'(V-\Phi^e-\alpha\theta u^e)(u^e)^2ds \\
&+\int_{\Gamma^2(0)}\varphi'(-\Phi^e-\alpha\theta u^e)(u^e)^2ds+\int_{\Gamma^m}\varphi'(V_b-\Phi^e+\alpha\Phi^m-\alpha\theta u^e)(u^e)^2ds\,]
\end{aligned}
$$

We have obtained an expression for $J(V_b+\alpha\Phi^m,\Phi^e+\alpha u^e)-J(V_b,\Phi^e)$ of the type:

$$J(V_b+\alpha\Phi^m,\Phi^e+\alpha u^e)-J(V_b,\Phi^e)=\alpha A+\frac{\alpha^2}{2}B$$

with:

$$A = \int_{\Omega^e} \sigma^e < \underline{grad}\,\Phi^e | \underline{grad}\,u^e > d\tau + \int_{\Gamma^1(V)} \varphi(V - \Phi^e) u^e ds + \int_{\Gamma^2(0)} \varphi(-\Phi^e) u^e ds + \int_{\Gamma^m} \varphi(V_b - \Phi^e)(\Phi^m - u^e) ds$$

$$B = \int_{\Omega^e} \sigma^e \|\underline{grad}\,u^e\|^2 d\tau + \int_{\Gamma^1(V)} \varphi'(V - \Phi^e - \alpha\theta u^e)(u^e)^2 ds + \int_{\Gamma^2(0)} \varphi'(-\Phi^e - \alpha\theta u^e)(u^e)^2 ds + \int_{\Gamma^m} \varphi'(V_b - \Phi^e + \alpha\Phi^m - \alpha\theta u^e)(u^e)^2 ds$$

All integrals of B are positive because φ is nondecreasing, then $B \geq 0$. If V_b and Φ^e realized the minimum of $J(\Phi^m, u^e)$

$$J(V_b + \alpha\Phi^m, \Phi^e + \alpha u^e) - J(V_b, \Phi^e) \geq 0$$

$$\text{for all}\, \alpha \in \mathbb{R}, \text{ and for all}\, u^e \in H$$

Thus

$$\alpha A + \underbrace{\frac{\alpha^2}{2} B}_{\geq 0} \geq 0, \quad \text{for all}\, \alpha \in \mathbb{R}, \text{ and for all}\, u^e \in H$$

This condition is satisfied if and only if $A = 0$.

That gives finally:

$$\begin{cases} \displaystyle\int_{\Omega^e} \sigma^e < \underline{grad}\,\Phi^e \,|\, \underline{grad}\,u^e > d\tau \\ \displaystyle + \int_{\Gamma^1(V)} \varphi(V - \Phi^e)\, u^e ds + \int_{\Gamma^2(0)} \varphi(-\Phi^e)\, u^e ds \\ \displaystyle - \int_{\Gamma^m} \varphi(V_b - \Phi^e)\,(\Phi^m - u^e) ds = 0 \end{cases}$$

which is precisely to the formulation of the PROBLEM 2A (2.8) when $c^m := \Phi^m$.

Bibliography

[ALY] ALYZER SA, Industrial Electrochemistry. CH-6950 Mendrisio.

[AS84] F. Coeuret A. Storck. *Eléments de génie électrochimique.* 401. Lavoisier, Paris, 1984.

[AVS] AVS, Advanced Visual Systems Inc, version 5.2, 1997.

[Bar93] J. Baranger. *Analyse numérique, Chapitre 5.3 (Méthode du gradient conjugué)*, volume 1 of *Collection enseignement des sciences.* Hermann, Paris, 1993.

[BC94] G. Bonvin and Ch. Comninellis. Scale-up of bipolar electrode stack dimensionless numbers for current bypass estimation. *Journal of Applied Electrochemistry*, 24:469–474, 1994.

[BF83] A.J Bard and L.R. Faulkner. *Electrochimie, principes, méthodes et applications.* Chapitre 3. Masson, Paris, 1983.

[Bol88] Pascal Bolomey. *Caractérisation d'un réacteur électrochimique non-divisé à électrodes bipolaires planes parallèles.* Thèse de doctorat ès sciences techniques No. 753, Ecole Polytechnique Fédérale de Lausanne, Lausanne, 1988.

[Bon92] Guy Bonvin. *Pertes et distributions de courant dans un réacteur électrochimique non-divisé à électrodes bipolaires planes parallèles.* Thèse de doctorat ès sciences techniques No. 1029, Ecole Polytechnique Fédérale de Lausanne, Lausanne, 1992.

[BR85] J.M Bockris and A.N Reddy. *Modern Electrochemistry, An introduction to an interdisplinary area*, volume 2. Plenum press, New York, 1985.

[CC95a] Eric Plattner P. Vaudano C. Comninellis. The industrial electrolytic regeneration of $mn_2(so_4)_3$ for the oxydation of substitued toluene to the corresponding benzaldehyde. *CHIMIA*, 49:12–16, 1995.

[CC95b] S. Muller F. Holzer O. Haas C. Comninellis. Development of rechargeable monopolar and bipolar zinc/air batteries. *CHIMIA*, 49:27–32, 1995.

[Dav86] A.J. Davies. *The Finite Element Method: A First Approach.* Oxford applied mathematics and computing science series. Oxford University Press, 1986.

[Dec94] J. Deconinck. Mathematical modeling of electrode growth. *J. Electrochem. Soc.*, 212(24):785, 1994.

[EK83] R.F. Savinell E.A Kaminsky. A technique for calculation of shunt linkeage and cell currents in bipolar stacks having divided or undivided cells. *J. Electrochem. Soc.*, 130:1103, 1983.

[FC97] H. Froidevaux and Ch. Comninellis. Mathematical formulation of electrochemical systems with bipolar configuration. In *The 1997 Joint International Meeting*, page 608. ISE 48th Annual Meeting and the Electrochemical society 192nd meeting , Paris, 1997.

[FM95a] H. Froidevaux and E. Mitha. Modélisation tridimensionelle de cellules électrochimiques productrices d'hydrogène par la méthode des éléments finis. Rapport pour l'office fédéral de l'energie, Département de Mathématiques, Ecole Polytechnique Fédérale de Lausanne, Lausanne, 1995.

[FM95b] H. Froidevaux and E. Mitha. Numerical methods for the design of electrochemical cells. In *Poster*. ISE 46th Annual Meeting, Xiamen, China, 1995.

[FMC97] H. Froidevaux, E. Mitha, and Ch. Comninellis. Modelling of a bipolar electrochemical reactor using numerical simulations. In *Current and potential distributions in complex electrochemical systems*, page 18. European workshop on current and potential distributions in complex electrochemical systems, Nancy, 1997.

[FMCM96] H. Froidevaux, E. Mitha, Ch. Comninellis, and V. Merminod. Modelling of a bipolar electrochemical reactor using numerical simulations. In *Contemporary Trends in Electrochemical Engineer, Symposium proceedings*. 4th European Sysmposium on Electrochemical Engineering, Prague, Czech Republic, 1996.

[FMS95] H. Froidevaux, E. Mitha, and J.-Y. Salamin. Modelization of a bipolar electrochemical reactor. *CHIMIA*, 49:3–12, 1995.

[Fro] H. Froidevaux. Formulations et démonstrations des problèmes mathématiques en relation avec la modélisation de systèmes électrochimiques, DMA-EPFL, 1994.

[FS94] H. Froidevaux and J.-Y. Salamin. Modélisation de réacteurs électrochimiques bipolaires. Rapport pour l'office fédéral de l'energie, Département de Mathématiques,

Ecole Polytechnique Fédérale de Lausanne, Lausanne, 1994.

[Geo91] P.L George. *Génération automatique de maillages: application aux méthodes déllements finis.* Masson, Paris, 1991.

[IR86] V. Cezner I. Rousar. Experimental determination and calculation of parasitic current in bipolar electrolyzers with application to chlorate electrolyzer. *J. Electrochem. Soc.*, 121:648, 1986.

[JB79] D.E. Danly J.C. Burnett. Current bypass in electrochemical cells assemblies. *AICHE Symposium 75*, page 8, 1979.

[JD97] D. Froning W.Lehnert J. Meusinger U. Stimming J. Divisek. Current and potential distribution on ni-cermet electrodes during methane steam reforming sofc. In *Current and potential distributions in complex electrochemical systems*, page 8. European workshop on current and potential distributions in complex electrochemical systems, Nancy, 1997.

[JH84] R.E. White J.A. Holmes. *Electrochemical cell Design.* 311. Plenum Press R. White, New York, 1984.

[J.L71] J.L. Lions. Cours d'analyse numérique. Ecole Polytechnique. Paris, 1971.

[J.N73] J.Newmann. *Electrochemical systems.* 403. Prentice-Hall Inc. Englewood Cliffs, 1973.

[Kel69] R.B Kellogg. A nonlinear alternating direction method. *Math. Comp.*, 23, 1969.

[Lan94] D. Landolt. Electrochemical and material science aspects of alloy deposition. *Electrochemica Acta*, 39, 1994.

[LJ91] G. J. Visser L.J.J. Janssen. Behaviour of a tall vertical gas-evolving cell: Part ii: distribution of current. *J. of Applied Electrochemistry*, 21:753, 1991.

[LPS89] R. Lageman, W. Pool, and G. Seffinga. Contamined soil, electro-reclamation: theory and practice. *Chemistry and Industry*, page 589, September 1989.

[LT93] P. Lascaux and R. Théodor. *Analyse numérique matricielle appliquée à l'art de l'ingénieur, chapitre 5: méthodes directes pour les matrices creuses*, volume 1. Masson, Paris, 1993.

[Mar91] S.L. Marshall. Mathematical analysis of interfacial current distribution in cylindrical porous electrodes. *J. Electrochem. Soc.*, 138(6):1040, 1991.

[Mer96] V. Merminod. experimental measurements in a bipolar cell. Institute of Chemical Engineering, EPFL, 1996.

[Mer97] V. Merminod. Estimation des conductivités à partir des concentrations données par [LPS89]. Communication personnelle, 1997.

[PM97] E. Petit M. Rakib P. Viers P. Moçoteguy. Current and potential distribution on ni-cermet electrodes during methane steam reforming sofc. In *Current and potential distributions in complex electrochemical systems, Nancy*, page 8. European workshop on current and potential distributions in complex electrochemical systems, 1997.

[Pou63] M. Pourbaix. *Atlas d'équilibres chimiques.* Ed. Gauthier-Villard, Paris, 1963.

[RB96] W. O. Rasmussen and M. Budhu. Electrode placement for subsurface electric field generation. *Journal of Environmental Engineering*, 122(8):764–768, 1996.

[Rou74] I. Rousar. Current distribution at the electrodes in zinc electrowinning cells. *J. Electrochem. Soc.*, 121:648, 1974.

[RP87] P. C. Renaud and R. F. Probstein. Electroosmotic control of hazardous wastes. *Physico Chemical Hydrodynamics*, 9:345–360, 1987.

[RW90] F. Jangush R.E White. Three dimensional current distributions in a bipolar, chlor-alkali membrane cell. *J. Electrochem. Soc.*, 137(6):1846, 1990.

[Sal95] Jean-Yves Salamin. *Modélisation de réacteurs électrochimiques bipolaires à électrodes parallèles planes.* Thèse de doctorat ès sciences techniques No. 1332, Ecole Polytechnique Fédérale de Lausanne, Lausanne, 1995.

[SIM] SIMAIL, logiciel de maillage, version 6.1, SIMULOG, Paris.

[SS90] J.J.Smith S. Szpak, C. Gabriel. Intercell currents in assembly of modules. *J. Electrochem. Soc.*, 137(3):849, 1990.

[SY91] C.Y. Yao S.C. Yen. The bipolar analysis of a single sphere in an electrolytic cell. *J. Electrochem. Soc.*, 138(9):2697, 1991.

[YSC96] T. Kang Y. S. Choi. Three-dimensional calculation of current distribution in electrodeposition on patterned cathode with auxiliary electrode. *J. Electrochem. Soc.*, 143(2):480, 1996.

Curriculum Vitæ

I was born on 8th September 1967 in Tananarive, Madagascar. After my primary school in Grenoble (France), I did my secondary school in Mauritius (Indian Ocean) where I graduated with a French Baccalauréat C in 1985.
Afterwards, I started the Special Mathematics Course (CMS) in Lausanne and entered at the Swiss Federal Institute of Technology (EPFL) where I obtained my diplôme d'ingénieur électricien in 1992.
I started my PhD, with Prof. H. Froidevaux as my thesis supervisor at the Department of Mathematics in 1994. This work was completed in December 1997. During these four years, I also participated in teaching and has been assistant of Prof. P. Buser for the last two years.